UNIVERSITE DE BLIDA 1

Faculté de Technologie

Département de Mécanique

THÈSE DE DOCTORAT

Spécialité: Énergétique

L'ANALYSE DE L'INTERACTION FLUIDE STRUCTURE LORS DU MOUVEMENT VIBRATOIRE D'UNE AILE BATTANTE

Par

YOUNSI ABDELHAKIM

Composition du Jury:

BENKHEDA Y.	Professeur	U. de Blida 1	Président
BOUMEDDANE B.	Professeur	U. de Blida 1	Examinateur
GUERRI O.	Directrice de recherche	CDER	Examinateur
KEZRANE M.	MCA	U. de Médéa	Examinateur
ABDELLAH EL-HADJ A.	Professeur	U. de Médéa	Rapporteur
REZOUG T.	Professeur	U. de Blida 1	Co-Rapporteur

Blida, Janvier 2021

UNIVERSITY OF BLIDA1

Faculty of Technology

Department of Mechanical Engineering

DOCTORAL THESIS

Specialty: Energetics

FLUID STRUCTURE INTERACTION ANALYSIS OF A WING UNDER VIBRATORY MOVEMENT

By

ABDELHAKIM YOUNSI

Doctoral committee:

Y. BENKHEDA	Professor	U. Blida1	President
B. BOUMEDDANE	Professor	U. Blida1	Examiner
O. GUERRI	Research Director	CDER	Examiner
M. KEZRANE	Associate professor (MCA)	U. Médéa	Examiner
A. ABDELLAH EL-HADJ	Professor	U. Médéa	Supervisor
T. REZOUG	Professor	U. Blida1	Co-supervisor

Blida, January 2021

ACKNOWLEDGEMENT

The dissertation could not have been completed without the exceptional guidance of my advisor, Professor Abdellah Abdellah el hadj. Prof. Abdellah el hadj provided the guidance and intent to successfully execute research and add to the body of engineering knowledge.

In addition, I would like to give my personal and greatest gratitude to Professor Tahar Rezoug the Co supervisor of this dissertation for his willingness to help in this project.

I would also like to thank my committee members for volunteering to take time out of their busy schedules to review my work. Their time and effort is greatly appreciated.

Finally, I would like to thank my family, especially my parents, for their love and support. Their words of encouragement kept me going, especially this past year, and I do not think I would have made it without their help. They never stopped believing in me, even when I did not believe in myself.

ملخص

لطالما كان علماء البيولوجيا والهندسة مفتونين بطريقة طيران الحشرات والطيور. أثرت التطورات الحديثة في تقنيات الطيران والقدرات الحسابية في تطوير طائرات من صنع الإنسان تحاكي طريقة طيران الحشرات و الطيور والتي تُسمى المركبات الجوية المجهرية (MAVs) والمركبات الجوية النانو(NAVs) . ولكن، إلا نماذج اولية قليلة حلقت بنجاح. جزء من السبب هو أن الديناميكا الهوائية لطيران الطيور الصغيرة والحشرات لا تزال غير مفهومة تمامًا. نتائج النظاريات القديمة وجدت ان قوة الرفع التي تنتجها الحشرات والطيور لابقائها محلقة في الهواء غير كافية، هذا الأمر أثار اهتمامًا كبيرًا لتحديد الآليات المستخدمة من قبل هذه الحشرات لتحسين قوة الرفع.

الهدف من هذه الدراسة هو الحصول على فهم أفضل لتأثيرات العديد من العوامل التي لم يتم أخذها في الاعتبار من قبل على الديناميكا الهوائية للجناح الفردي والترادفي.

في الجزء الأول ، تم التحقيق في تأثيرات الأرض على جناح واحد تحت وضعين مختلفين من الطيران التحويمي وهما الوضع "normal" المستوحى من الطيور الطنانة وكذا وضع "water treading".

ابهر اليعسوب العلماء لاكثر من قرن بسبب مهاراتها العالية في الطيران. و هذا لانها تعتمد على جناحين بدلا من جناح واحد. لهذا السبب ، في الجزء الموالي تمت دراسة تأثيرات مدة الخفقان ، تباعد الأجنحة و تأخر الطور على الديناميكا الهوائية لجنائحين مترافقين. وأخيرا, تمت دراسة تأثيرات الوضع الأولي للجناح الأمامي وعدم التناسق في تردد الخفقان على أداء الديناميكية الهوائية للجناحين مترادفين.

تركز هذه الدراسة على هيكل التدفق ، وتوزيع الضغط ، وإنتاج الرفع وكفائته في حالة الجناح المفرد.اما فيما يخص الجناحين المترادفين, تمت اضافة إنتاج قوة الدفع وكفائته في التحليل. تم استخدام ، طريقة الحجم المحدود لمحاكاة مجال التدفق باستخدام برنامج تجاري يسمى Ansys Fluent.

بالنسبة لجزء الأول ، وجدنا أنه على الرغم من ان الوضع التحويمي « normal » يتسخدم من طرف العديد من الحشرات الا ان الوضع « water treading" يولد قوة رفع أكبر ويمتلك كفاءة أعلى.

أما بالنسبة للجزء الثاني من هذه الدراسة ، فقد أشارت النتائج إلى أن فترة الخفقان كان لها تاثير أعلى بكثير من تأثير تباعد الجناحين و كذا فرق الطور.

وأخيرًا ، فيما يخص تأثيرات الموضع الأولي وعدم التناسق في تردد الخفقان. أظهر متوسط معاملات الرفع والدفع أن الجناح الفردي تفوق في الأداء على الجناحين المترافقين الذان يخفقان بضربات متعاكسة . الا أن ، كفاءات الرفع والدفع كانت اعلى عند الجناحين المترافقين. وأظهرت النتائج أيضًا أن التردد العالي للجناح المتقدم ينتج عنه كفائة اعلى في قوة الرفع.

الكلمات المفتاحية: MAVs, NAVs, water treading, normal hovering, الأجنحة الترادفية, وضع التحويم, قوة الرفع, قوة الدفع, Ansys Fluent, ، طريقة الحجم المحدود.

RESUME

Les scientifiques en biologie et en ingénierie ont toujours été captivés par le vol des insectes et des oiseaux. Les récents progrès réalisés dans les technologies aéronautiques et les capacités de calcul ont incité les scientifiques à développer des oiseaux et insectes artificiels imitant le vol naturel de ceux-ci, appelés micro-véhicules aériens (MAV) et nano-véhicules aériens (NAV). Cependant, seuls quelques prototypes ont volé avec succès .Une partie de la raison est que l'aérodynamique du vol des petits oiseaux et des insectes n'est pas encore pleinement comprise.

Les premières théories sur l'état quasi-permanent ont révélé que la force de portance produite par les insectes et les oiseaux était insuffisante pour soutenir leur poids, ce qui suscitait un vif intérêt pour l'identification des mécanismes utilisés par ces derniers pour améliorer la génération de portance.

Le but de cette thèse est d'avoir un meilleur aperçu des effets de plusieurs paramètres qui n'avaient jamais été pris en compte auparavant sur l'aérodynamique des ailes battantes.

Dans la première partie, nous étudions les effets du sol sur une seule aile elliptique sous deux modes de vol stationnaire à savoir «normal» qui a été inspiré par le vol des colibris et le mode «water treading». Les libellules possèdent des compétences de vol exceptionnelles. Une partie de la raison est qu'ils ont deux ensembles d'ailes. Pour cette raison, dans la deuxième partie, nous étudions les effets de la durée de battement, l'espacement des ailes, la différence de phase sur l'aérodynamique des ailes en tandem. Enfin, les effets de la position initiale de l'aile antérieure et de l'asymétrie de la fréquence de battement sur les performances aérodynamiques des ailes en tandem sont étudiés. L'analyse porte sur la structure de l'écoulement, la distribution de pression, la production et l'efficacité de portance pour le cas de l'aile seule. En ce qui concerne la configuration en tandem, la production et l'efficacité de poussée sont ajoutés à l'analyse. La méthode de volumes finis a été utilisée pour simuler le champ d'écoulement dans les deux cas à l'aide du logiciel commercial Ansys Fluent.

Dans la première partie, il a été constaté que, bien que le mode de vol stationnaire «normal» est utilisé par de nombreux insectes, le mode «water treading» générait plus de force de portance et possédait une efficacité de portance plus élevée. Quant à la deuxième partie de cette étude, les résultats indiquent que les

effets de l'asymétrie dans la durée des battements sont significativement plus élevés que les effets de l'espacement des ailes et la différence de phase. Enfin, les effets de la position initiale et de l'asymétrie de la fréquence de battement sont examinés. Les coefficients de portance et de poussée moyens ont révélé que l'aile seule surpassait la configuration en tandem qui bat en contre-course. Cependant, les rendements de portance et de poussée étaient plus élevés en configuration tandem. Les résultats ont en outre montré dans la deuxième partie que lorsque l’aile antérieure volets avec une fréquence plus élevée, la production et l'efficacité de l'ascenseur étaient considérablement améliorées.

Mots clé: MAVs, NAVs, water treading, normal vol stationnaire, ailes en tandem, vol stationnaire, vol en avant, aile, Ansys Fluent, méthode de volumes finis, force de portance and force de poussée.

ABSTRACT

For many years, biological and engineering scientists have been intrigued by the flight of birds and insects. The recent advances in aeronautic technologies and computational capabilities have influenced scientists to develop man-made flyers that mimic natural flyers' flight, which are called Micro Air Vehicles (MAVs) and Nano air vehicles (NAVs). However, only few prototypes flew successfully. Part of the reason is that the aerodynamics of small birds and insects' flight are still not fully understood. Early steady state theories found that the lift force generated by insects and birds is insufficient to sustain their body weight, which aroused a great interest to identify and study the unsteady mechanisms used by these flyers to enhance the lift and thrust generation such as the clap and fling, delayed stall, .rapid rotation and wake capturing.

The aim of this study is to get a better insight into the effects of multiple parameters that have never been considered before on the aerodynamics of single and tandem flapping wing configurations.

In the first part, we investigate the effects of the ground on a single elliptic wing under two hovering flight modes namely "normal" mode that was inspired by hummingbirds and "water treading" mode. Dragonflies have fascinated scientists for most of this century due to their outstanding flight skills. Part of the reason is that they have two sets of wings. For this reason, in the second part, we investigate the effects of the flapping duration, wing spacing and phase difference on the aerodynamics of flapping tandem configuration. Finally, the effects of the initial position of the forewing and the asymmetry in flapping frequency on the aerodynamic performance of flapping tandem configuration are studied. The analysis focuses on the flow structure, pressure distributions, lift production and efficiency for the case of the single wing. As for the tandem configuration, the thrust production and efficiency are added to the analysis. A finite volume method is used to simulate the flow field using a commercial software Ansys Fluent. The flow is considered laminar, incompressible and two-dimensional.

For the first case, it was found that although many insects use the "normal" hovering mode, the "water treading" generated more lift force and possessed higher lift efficiency. As for the second part of this study, the results indicated that the effects of the downstroke ration were significantly higher than the effects of the wing spacing

and phase difference. Finally, the average lift and thrust coefficients revealed that a single wing outperformed the tandem configuration that flaps in counterstroke. However, the lift and thrust efficiencies was higher in tandem configuration. The results in the second part further showed that when the forewing flaps with higher frequency the lift production and efficiency were significantly improved.

Keywords: MAVs, NAVs, water reading, normal hovering, tandem wings, hovering, forward flight, Ansys Fluent, finite volume method, thrust force, and lift force.

TABLE OF CONTENTS

ACKNOWLEDGEMENT III
ملخص IV
RESUME V
ABSTRACT VII
TABLE OF CONTENTS IX
LIST OF FIGURES XII
LIST OF TABLES XVII
INTRODUCTION 1
OVERVIEW AND MOTIVATION 1
THESIS OBJECTIVES 1
THESIS OUTLINE 2
CHAPTER 1: INTRODUCTION TO FLAPPING FLIGHT 4
1.1 Introduction 4
1.2 Definition of unmanned aerial vehicles (drones) 4
1.3 Classifications of drones 5
1.4 Introduction to Micro Air Vehicles 6
1.5 Classification of MAVs 7
1.5.1 Fixed wing MAVs 7
1.5.2 Rotary wing MAVs 8
1.5.3 Flapping wing MAVs 9
1.5.4 Flapping / Fixed wing MAVs 10
1.6 Classification of NAVs 10
1.6.1 Flapping wing NAVs 11
1.6.2 Rotary wing NAVs 12
1.6.3 Monocopter NAVs 12
1.7 Naturel flyers' flight 13
1.7.1 Unpowered Flight 13
1.7.2 Powered flight 14
1.8 The quasi steady theory 18
1.9 Unsteady mechanisms identified to enhance lift in insects 19
1.9.1 Leading edge vortices and delayed stall 19
1.9.2 Rapid pitching 20
1.9.3 Wake capturing 21
1.9.4 Clap and fling 22
CHAPTER 2: LITERATURE REVIEW 24
2.1 Introduction 24
2.2 Numerical and experimental studies on the ground effects in hovering flight 24
2.3 Numerical studies on flapping tandem wing configuration in forward flight 25
2.4 Experimental studies on flapping tandem wing in forward flight 26
2.5 Numerical studies on the effects of the asymmetry of downstroke ratio 27
2.6 Summary 27

CHAPTER 3: MATHEMATICAL MODEL 29

3.1 COMPUTATION TECHNIQUES 29
3.2 CHARACTERISTICS OF MAVS FLOW AT LOW REYNOLDS NUMBER 29
3.2.1 Incompressible Flow 29
3.2.2 Unsteady Flow 29
3.2.3 Viscous/Inviscid 30
3.3 ANSYS FLUENT 30
3.4 FINITE VOLUME METHOD 30
3.5 GOVERNING EQUATIONS OF FLUID FLOW 31
3.6 DISCRETIZATION PROCESS 31
3.6.1 Spatial Discretization 33
3.6.2 Temporal Discretization 35
3.6.3 Discretization of the Momentum Equation 36
3.6.4 Discretization of the Continuity Equation 37
3.7 PRESSURE-VELOCITY COUPLING 38
3.7.1 Coupled Algorithm 38
3.8 UNDER RELAXATION FACTORS 39
3.9 NAVIER STOKES EQUATIONS 40
3.10 DIMENSIONLESS NUMBERS 41
3.11 PARAMETER DEFINITION 41

CHAPTER 4: EFFECTS OF THE GROUND ON AN AIRFOIL UNDER TWO HOVERING MODES AT RE=100 44

4.1 INTRODUCTION 44
4.2 KINEMATIC DESCRIPTION AND BOUNDARY CONDITIONS 44
4.3 MESH GENERATION 47
4.4 GRID INDEPENDENCY ANALYSIS 48
4.5 COMPARISON WITH SIMILAR WORK 51
4.6 RESULTS AND DISCUSSION 52
4.6.1 Water treading hovering mode in ground effect 52
4.6.2 Normal hovering mode in ground effect 58
4.7 SUMMARISED RESULTS 63
4.8 CONCLUSION 66

CHAPTER 5: EFFECTS OF THE WING SPACING, PHASE DIFFERENCE AND DOWNSTROKE RATIO ON FLAPPING TANDEM WING AT RE=157 68

5.1 INTRODUCTION 68
5.2 KINEMATIC DESCRIPTION OF THE FLAPPING TANDEM WING 68
5.3 BOUNDARY CONDITIONS AND MESH GENERATION 74
5.4 GRID INDEPENDENCY 75
5.5 VALIDATION STUDY 78
5.6 RESULTS AND DISCUSSION 78
5.6.1 Effects of the downstroke ratio on a single wing: 79
5.6.2 Effects of wing spacing on flapping tandem wing configuration 80
5.6.3 Effects of wing spacing, phase difference and downstroke ratio on the lift generation 81
5.6.4 Effects of wing spacing, phase difference and downstroke ratio on the thrust generation 87
5.6.5 Effects of wing spacing, phase difference and downstroke ratio on the thrust and lift efficiencies 95
5.7 CONCLUSION 96

CHAPTER 6: EFFECTS OF INITIAL POSITION AND ASYMMETRY IN FLAPPING FREQUENCY ON TANDEM WING AT RE=5000 98

6.1 INTRODUCTION 98
6.2 KINEMATIC DESCRIPTION AND BOUNDARY CONDITIONS 98
6.2.1 Kinematic description 98

6.2.2 Boundary conditions and mesh generation *99*
6.3 VALIDATION OF NUMERICAL METHOD 101
6.4 RESULTS AND DISCUSSION 101
6.4.1 Effect of initial position *101*
6.4.2 Effect of frequency *119*
6.5 CONCLUSION 127
CONCLUDING REMARKS AND FUTURE WORK 128
NOMENCLATURE 131
REFERENCES 133

LIST OF FIGURES

Figure 1.1 Minimum cost of transport (COT) for various objects [1]. 4
Figure 1.2 Tactical drone at launch by a solder [4] 5
Figure 1.3 Experiment copy of a smart dust, distribution and data collection from it [8] 5
Figure 1.4 Spectrum of drones from UAV to SD [9]. 6
Figure 1.5 Different types of air vehicles [9]. 6
Figure 1.6 Examples of Fixed wing MAV [14]. 8
Figure 1.7 Rotary wings MAVs. 9
Figure 1.8 A view of "Thunder I" flapping wing MAV [21]. 10
Figure 1.9 Jones' flapping wing– propelled MAV [22]. 10
Figure 1.10 AeroVironment NAV [24]. 11
Figure 1.11 RoboBee [25]. 11
Figure 1.12 Black Hornet PRS [26]. 12
Figure 1.13 Robotic samara [27]. 12
Figure 1.14 Hovering flight pattern of large birds [32]. 14
Figure 1.15 Hovering flight pattern of insects and small birds [32]. 15
Figure 1.16 The Great Flight Diagram gives a relation among wing loading, weight [34]. 16
Figure 1.17 Montage of the flight path of a peregrine falcon in stoop with the corresponding live images (diving bird) [35]. 17
Figure 1.18 Galapagos Hawk taking off [37]. 17
Figure 1.19 Bald Eagle landing [38]. 18
Figure 1.20 Flow around a thin airfoil [49]. 19
Figure 1.21 Vorticity plot around a flapping airfoil [52]. 20
Figure 1.22 Experimental and numerical lift coefficients for a fruit fly-modelled wing [51]. 21
Figure 1.23 Momentum transfer due to wing-wake interaction. Sketched from Sane [49]. 22
Figure 1.24 Clap and fling mechanism. Left [30]. 22
Figure 1.25 Schematic of clap and fling mechanism. Based on Weis-Fough [30]. 23
Figure 3.1 The discretization process [82]. 32
Figure 3.2 Control Volume of two-dimensional triangular cells. 33
Figure 3.3 One-Dimensional Control Volume [84]. 34

Figure 4.1 Scheme of the “water treading” hovering mode. 45
Figure 4.2 Scheme of “normal” hovering mode. 45
Figure 4.3 Time histories of translation displacement and angle of rotation for the two hovering modes. 47
Figure 4.4 Time histories of translation velocity and angular velocity for the two hovering mode. 47
Figure 4.5 close-up view of the mesh near the wing surface, (a) at t/T=0, (b) at t/T=0.25. 48
Figure 4.6 Computational mesh, (A): coarse grid, (B): intermediate grid, (C) Fine grid. 49
Figure 4.7 Lift coefficient for three different grid size for the case of the “water treading mode at L=1c. 50
Figure 4.8 Comparison of the time histories of the lift and drag coefficients of the present study with the results obtained from the literature. 51
Figure 4.9 Lift coefficient of “water treading” hovering mode. 53
Figure 4.10 Vorticity contours at different instances of the "water treading" hovering mode for D=1c and D=2c. 54
Figure 4.11 Vorticity contours at different instances of the "water treading" hovering mode for D=3c and D=5c. 55
Figure 4.12 Pressure distribution on the airfoil surface for the “water treading” hovering mode. 56
Figure 4.13 Energy coefficient of “water treading” hovering mode. 57
Figure 4.14 Variations of $\boldsymbol{Cl}$, $\boldsymbol{Cp}$ and $\boldsymbol{\eta}$ for the “water treading” hovering mode. 57
Figure 4.15 Lift coefficient of “normal” hovering mode. 58
Figure 4.16 Vorticity contours of the “normal” hovering mode at D=1c and D=2c. 60
Figure 4.17 Vorticity contours of the “normal” hovering mode at D=3c and D=5c. 61
Figure 4.18 Pressure distribution on the airfoil surface for the “normal” hovering mode. 62
Figure 4.19 Energy coefficient of "normal" hovering mode. 63
Figure 4.20 Variations of $\boldsymbol{Cl}$, $\boldsymbol{Cp}$ **and** $\boldsymbol{\eta}$ for the “normal” hovering mode. 63
Figure 4.21 Time histories of $\boldsymbol{Cd}$ and $\boldsymbol{Cm}$ for both hovering modes, (a): Drag coefficient, (b): pitching moment coefficient. 64
Figure 4.22 Variation of $\boldsymbol{Cd}$ and **L/D** for both hovering modes. 65
Figure 4.23 Variation of $\boldsymbol{Cp}$ and $\boldsymbol{\eta L}$ for both hovering modes. 66
Figure 5.1 Schematic of the tandem wing motion. 72

Figure 5.2 Time histories of the flapping motion used in this study at ξ=0.35. *a)* Translation displacement A(t), *b)* angular rotation, α(t) 73
Figure 5.3 Computational domain and boundary conditions 74
Figure 5.4 Coarse mesh 75
Figure 5.5 Intermediate mesh 76
Figure 5.6 Fine mesh 76
Figure 5.7 Lift coefficient for three different grid sizes for the hindwing with L=2c and ξ=0.5. 77
Figure 5.8 Comparison of the time histories of the lift coefficient and drag coefficient of the present study and the results obtained from the literature. 78
Figure 5.9 Time histories of $\boldsymbol{Cd}$, $\boldsymbol{Cl}$and $\boldsymbol{Cp}$: a) drag coefficient, b) lift coefficient, c) energy consumption coefficient for an isolated single wing at 3 downstroke ratios 79
Figure 5.10 Variation of the mean thrust coefficient at different wing spacings and downnstroke rations at φ=0° 80
Figure 5.11 Variation of the mean lift coefficient at different wing spacings and downnstroke rations at φ=0° 80
Figure 5.12 vorticity contours around a single and tandem wing configurations with 0° of phase difference at L=1.25, L=1.5 and L=2c at time 0.75T 81
Figure 5.13 Time histories of the lift coefficient of the hindwing at different wing spacing L, phase difference φ and downstroke ratio ξ. 82
Figure 5.14 Vorticity contours for different wing spacing L. For ξ=0.5 at time=0.**3**5T 82
Figure 5.15 Vorticity contours for different phase difference angles and flapping ratios at the middle of the downstroke with L=1.5c. 85
Figure 5.16 Pressure distribution on the hindwing surface for L=1.5c at the middle of the downstroke for different phases and downstroke ratios 86
Figure 5.17 Variation of the mean lift coefficient $\boldsymbol{CL}$ 87
Figure 5.18 Time histories of the thrust coefficient of the hindwing at different wing spacing L, phase difference φ and downstroke ratios ξ. 88
Figure 5.19 Vorticity contours for different phase difference angles and flapping ratio at the middle of the upstroke for L=1.5c. 91
Figure 5.20 Pressure distribution on the hindwing surface for L=1.5c at the middle of the upstroke for different phases and downstroke ratios 92
Figure 5.21 Variation of the mean thrust coefficient $\boldsymbol{CT}$ 93

Figure 5.22 Time histories of the energy coefficient of the hindwing at different wing spacing L, phase difference φ and downstroke ratio ξ. 94
Figure 5.23 Variation of the mean energy coefficient $\boldsymbol{Cp}$ 95
Figure 5.24 variation of the thrust efficiency $\boldsymbol{\eta T}$. 95
Figure 5.25 variation of the lift efficiency $\boldsymbol{\eta L}$. 96
Figure 6.1 Schematic of the tandem wing motion. 99
Figure 6.2 Computational domain and boundary conditions 100
Figure 6.3 Computational grid used in this study. 100
Figure 6.4 Comparison of the time histories of the lift coefficient and drag coefficient of the present study and the results obtained from the literature. 101
Figure 6.5 Time histories of the flapping motion used in this study. a) Translation velocity Vt, b) rotation velocity ωt 102
Figure 6.6 Time histories of the lift coefficient of the Forewing at different phase angles. 104
Figure 6.7 Time histories of the lift coefficient of the Hindwing at different phase angles 104
Figure 6.8 Vorticity and pressure contours around the hindwing for φ=0° and φ=90°at t/T=0.25. 105
Figure 6.9 Vorticity and pressure contours around the hindwing for φ=0° and φ=90°at t/T=0.25 106
Figure 6.10 Time averaged CL of combined Fore/hind wing 107
Figure 6.11 Time histories of the thrust coefficient of the Forewing at different phase angles. 109
Figure 6.12 Time histories of the thrust coefficient of the Hindwing at different phase angles. 110
Figure 6.13 Vorticity and pressure contours around the hindwing for φ=0° and φ=90°at t/T=0.75. 111
Figure 6.14 Vorticity and pressure contours around the hindwing for φ=180° and φ=270°at t/T=0.75. 112
Figure 6.15 Time averaged CT of combined Fore/hind wing 113
Figure 6.16 Time averaged CR of combined Fore/hind wing. 114
Figure 6.17 Time histories of the power coefficient of the Forewing. 115
Figure 6.18 Time histories of the power coefficient of the hindwing. 115
Figure 6.19 Averaged CP of combined Fore/hind wing 116
Figure 6.20 Variation of $\eta T, \eta L \; and \; \eta R$, (a) thrust efficiency, (b): Lift efficiency, (c) resultant efficiency 118

Figure 6.21 Time histories of the translation velocity for the three cases. 120
Figure 6.22 Time histories of the thrust coefficient CT of the three cases. 121
Figure 6.23 Time histories of the lift coefficient CL of the three cases. 121
Figure 6.25 Vorticity contours of the Case 1 and Case 4 at t/T= 0.12, t/T=0.25 and t/T=0.88. 123
Figure 6.26 Vorticity contours of the Case 2 and Case 5 at t/T= 0.3, t/T=0.85 and t/T=1.85. 124
Figure 6.27 Vorticity contours of the Case 3 and Case 6 at t/T= 0.75, t/T=1.7 and t/T=2.85. 125
Figure 6.24 Time histories of the energy coefficient CP of the three cases. 125
Figure 6.28 Time average of CT, CL and CR for all cases studied compared with the symmetrical case, (a): average thrust coefficient, (b): average lift coefficient and (c): average resultant coefficient 126
Figure 6.29 Variation of $\eta T, \eta L \; and \; \eta R$, (a) thrust efficiency, (b): Lift efficiency, (c) resultant efficiency 126

LIST OF TABLES

Table 3.1 Corresponding ∅ for transport equation. 40

Table 4.1 Grid independence study for the case of “water treading” hovering mode at Re=100, h_a=1.4c, α_0=0°, α_a=45°, D=1c. 50

Table 5.1 Grid independence study results for tandem wing configuration. Re=157, L=2c, $\xi = 0.5 \; and \; \varphi = 0°$ 77

Table 5.2 Lift coefficient at the middle of the downstroke for L=1.5c 84

Table 5.3 Thrust coefficient at the middle of the upstroke for L=1.5 90

Table 5.4 Lift coefficient at the middle of the upstroke for L=1.5c 90

Table 6.1 average lift coefficient of the best performing tandem wing configuration (CLb) compared with the single (CLs) case as well as the tandem wing at A_0=0c ($CL\ 0c$) 107

Table 6.2 average thrust coefficient of the best performing tandem wing configuration (CTb) compared with the single (CTs) case as well as tandem configuration at A_0=0c ($CT\ 0c$) 113

Table 6.3 Thrust efficiency of the best performing tandem wing configuration (ηTb) compared with the single (ηTs) case as well as tandem configuration at A_0=0c ($\eta T\ 0c$) 117

Table 6.4 Lift efficiency of the best performing tandem wing configuration (ηLb) compared with the single (ηLs) case as well as tandem configuration at A_0=0c ($\eta L\ 0c$) 117

Table 6.5 variation of the flapping frequency factor ε. 119

INTRODUCTION

Overview and motivation

The generation of lift and thrust forces through flapping wings is not a new idea. Insects and bird flight have fascinated human beings for hundreds of years. Early flying attempts were made through mimicking the flapping motion of birds and insects. However, human arms are too weak to flap large wings. This contributed in the invention of aircrafts that can sustain them in flight. Other propulsive aircrafts such as propellers and jet engines were invented just in the beginning of the last century. Micro Air Vehicle (MAVs) are miniature class of unmanned vehicles (drones). There are three generation of MAVs, Fixed wing (similar to conventional airplanes), rotary wing (similar to helicopters) and flapping wing (inspired by birds and insects flight), which this thesis focuses on. At low Reynolds numbers, small and light weighted aircrafts that use flapping wing to generate thrust and lift forces are considered highly more efficient than the conventional rotary and fixed wing designs. However, direct copying of certain proprieties of natural flyers (insects and birds) is unlikely to be successful. Therefore, understanding the essential physics behind flapping motion is highly necessary.

Thesis objectives

The purpose of this thesis is to get a better insight into the effects of the unsteady mechanisms and vortex dynamics of flapping motion of a single and tandem wing configuration for possible use in the designs of Micro and Nano air vehicles.

The essential physics of unsteady airfoil problems can be observed from simplified two-dimensional experiments. Therefore, two-dimensional airfoils were used in this work.

The main objective of this study is to find the optimal wings configuration and flapping kinematics (in terms of thrust and lift generations and efficiencies). In order to gain a full understanding to help optimizing the designs of flapping wings MAVs, the effects of multiple kinematic parameters on the aerodynamics of flapping wings are investigated. Two flapping flight modes were considered; hovering and forward

flight modes. First, the effects of the ground on two hovering flight modes are investigated. While for the forward flight, the effects of several kinematic parameters and wing configurations on the aerodynamics of tandem wing arrangement are carried out next.

Thesis outline

The thesis is organized as follows:

In Chapter1, a brief introduction of the different classifications of drones is presented. A detailed discussion on the flight capabilities and limitations of the Micro and Nano air vehicles is also considered. Since the flapping wing design of which this thesis focuses on mimics the flight of either small birds or insects, a detailed investigation on flight characteristics as well as the mechanisms used by natural flyers to enhance their aerodynamic performance is provided next.

In chapter 2, a literature survey on past and current numerical and experimental investigations on both hovering and forward flight modes is presented. This survey is divided into two sections. The first section summarizes the previous work on the effect of the ground on the aerodynamics of a single wing in hovering flight. The second section represents the previous work on the effects of the wing spacing and the phase on tandem wing configuration in both hovering and forward flight.

In chapter 3, the numerical framework for solving flapping wings problems with moving boundaries is presented. The fluid's governing equations are presented as well as the numerical implementation of those equations in a pressure-based fluid solver.

Chapter 4 investigates numerically the effects of the ground on the flow around a hovering airfoil at Re=100. Two types of hovering mode are studied "Water treading" and "Normal" modes. Several ground clearances were considered. The aim is to have a better insight into the effects of the ground on the lift force production as well as the energy consumption.

In chapter 5, a study of the flow over tandem wings in asymmetric stroke is carried out. The effects of the wing spacing L and the phase difference angle φ between the forewing and the hindwing are taken in consideration. The energy consumption and the flight efficiency have also been taken in consideration. The

Reynolds number was fixed at 157, which is related to a typical flight of dragonfly flight.

Chapter 6 studies the effects of initial position and asymmetry in flapping frequency on the aerodynamics of tandem wing at Re=5000. For the first part of this study, we vary the initial position of the forewing with an interval of 0.25c (c is the chord length) and the phase difference from 0° to 270° (with an interval of 90°). For the second part, we vary the frequency. The effects of these parameters on the flow structure as well as the aerodynamic forces and the energy consumption were deeply investigated.

Finally, a brief overview of the work that has done as well as summary and the directions for the future work are provided.

CHAPTER 1: INTRODUCTION TO FLAPPING FLIGHT

1.1 Introduction

The cost of transport (COT) is related to several of the familiar measures of economy used for man-made vehicles. For a particular vehicle, it is directly proportional to litters of fuel consumed per 100 km. While for animals, it is directly proportional to their body weight and type of locomotion [1].

The COT for insects, birds, mammals, and other animals and man-made vehicles with various weights and types of locomotion are shown in Figure 1.1. It can be seen that running or walking is the most expensive in terms of energy costs, while flying is the cheapest. This why designing efficient aircrafts has been always an interesting field of research especially with the recent raising demands for energy.

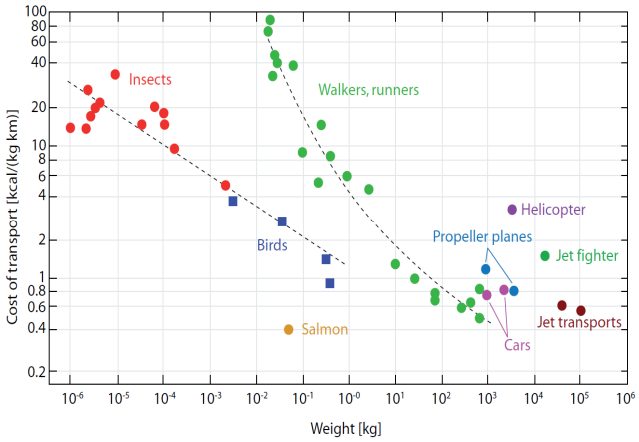

Figure 1.1 Minimum cost of transport (COT) for various objects [1].

There are two categories of aerial vehicles: manned and unmanned (drones). This thesis focuses only on the flow at the low Reynolds regime and since manned aircrafts operate at high Reynolds number due to their large size and highflying speed, this type is excluded.

1.2 Definition of unmanned aerial vehicles (drones)

Drones are flying vehicles that do not carry human operator on them (as the one shown in Figure 1.2). They can fly remotely or independently. Depending on their size, they can fly thousands of kilometres or fly in confined spaces. In recent

years, drones or unmanned aerial vehicles have become more and more attractive due to various application that can offer such as military surveillance, planetary exploration, search-and-rescue, farming and border patrol, mapping and scientific research and many more [2, 3].

Figure 1.2 Tactical drone at launch by a solder [4]

1.3 Classifications of drones

There are many different ways of classifications of drones. Brooke-Holland [5] and Arjomandi et al [6] proposed a classification based on their weight. Brooke-Holland labelled the smallest drones as Class I with weight less than 200 g, and the largest drones as Class III with weight superior than 600 Kg. Zakora and Molodchick [7] suggested a classification based on weight and flight ranges. Where the weight of Micro Unmanned Vehicles (μUAV) is less than 5kg, their flight ranges between 25km and 40 km. Wide varieties of drones were used for military and civilian purposes. Drones range in size from large fixed-wing unmanned air vehicle (UAV) to smart dust (SD) which consists of many tiny micro-electro-mechanical systems including sensors or robots (as shown in Figure 1.3).

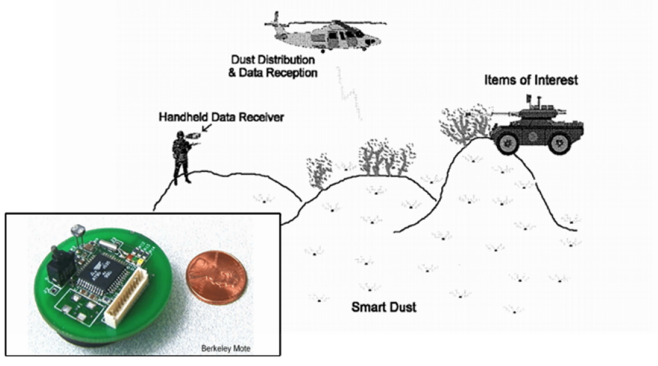

Figure 1.3 Experiment copy of a smart dust, distribution and data collection from it [8]

There are several types of drones between UAVs and SDs, such as Micro Air Vehicles (MAVs), Nano Air Vehicle (NAVs) and Pico Air Vehicles (PAVs). In Figure 1.4, the spectrum of different types of drones is presented [9].

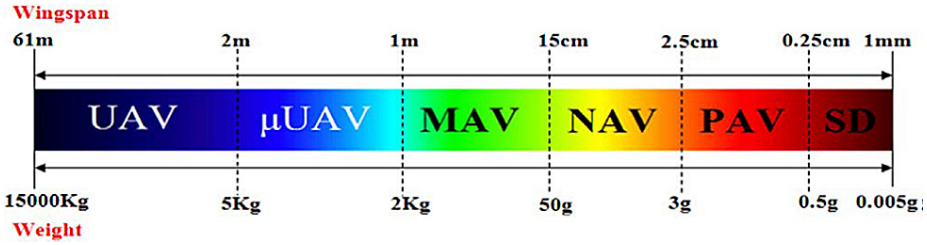

Figure 1.4 Spectrum of drones from UAV to SD [9].

Figure 1.5 gathers all types of drones and classifies them based on their propulsion system, where the HTOL and VTOL are the abbreviation terms of horizontal and vertical take-off and landing, respectively.

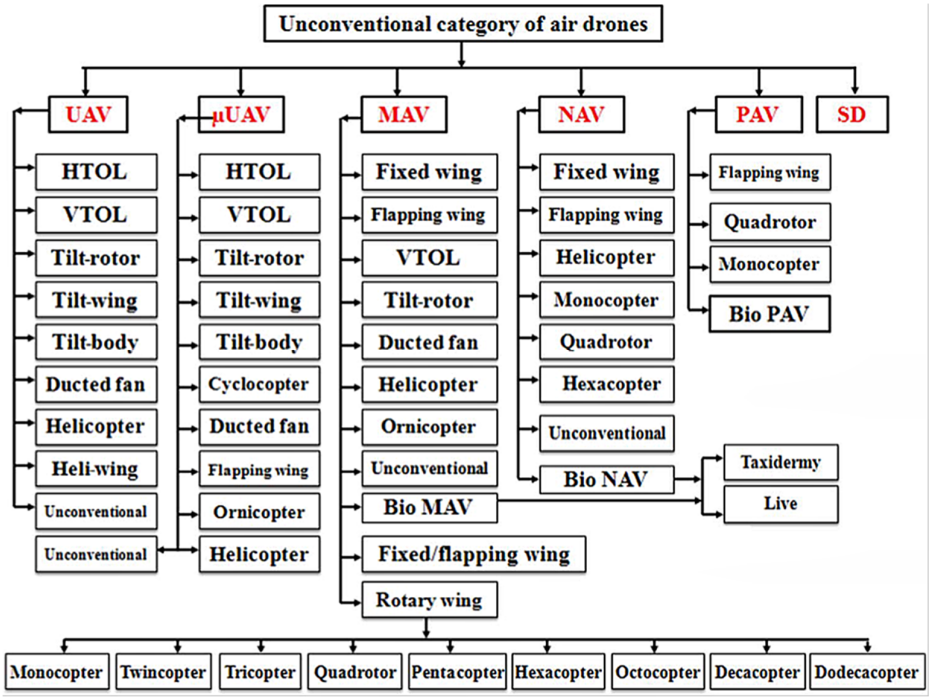

Figure 1.5 Different types of air vehicles [9].

In this present thesis, we only focus on the MAVs and NAVs designs.

1.4 Introduction to Micro Air Vehicles

Miniaturization of UAVs provides new possibilities that larger aircraft cannot offer. Several applications that were dominated by large UAVs were made possible

by smaller, lighter and cheaper ones. The Defense Advanced Research Projects Agency (DARPA) program used to limit these air drones to a size less than 150 mm in length, width, or height and weighing between 50 and 100 g [10, 11] , but after the advent of the NAVs and PAVs, the definition for MAV was changed. MAVs are now defined as micro planes with length smaller than 100 cm and weight lower than 2 Kg [12].

These vehicles are characterized by the smaller size and low flight speed. These characteristics imply low stall velocity and low inertia, which make these vehicles, fly at low speed and consume less energy. Regarding the size and the normal flight speed of these vehicles, the maximum Reynolds number is always lower than 10^4 [13]. The ability of these miniature-flying vehicles to hover makes them of high importance since the ability to hover allows the vehicle to fly indoors.

Indoor flight provides emergency teams' valuable information especially that most MAVs can be equipped with microphones, sensors, and cameras.

MAVs fly at low speeds and low altitudes, which makes them ideal for exploring areas in which helicopters are unable to reach, examine or poses some threats on them to operate. They can also be a replacement of soldiers when the missions requires entering a potential dangerous building. The Low cost and rapid deployment of the MAVs make it easy to a team to deploy multiple Mavs and collect data rapidly.

1.5 Classification of MAVs

There are three different configurations of MAVs. Fixed wings, rotary wings, and flapping wings, which are among the most important designs nowadays dues to their promising potentials.

1.5.1 Fixed wing MAVs

The most technically advanced MAV design is that with fixed wing configuration.Identical to conventional aircraft with propulsive system to maintain flight. All fixed wing MAVs use low aspect ratio wings to maximize area for a constrained wingspan.

The low aspect ratio wings offer area to store fuel or payload compared to other MAV configurations. Moreover, they are relatively more efficient in producing lift at high flight speeds. Fixed wing designs use separate systems to generate thrust

such as engine or propeller. For the production of lift force and control, they use airfoils. Fixed wing MAVs are perfectly suited for missions requiring long endurance and high cruise speeds.

They are highly desirable both from mechanical and control point of view. This is due their low complexity. However, they must maintain a high forward velocity for their wings to generate lift. Moreover, they tend to have large turn radii, making them unsuitable for prolonged applications in confined environments. Figure 1.6 represents a model of Fixed wing MAVs designed by Hussain et al [14]. This MAV uses Airfoil S5010 with aspect ratio of 1.45 while its endurance is around 20 minutes.

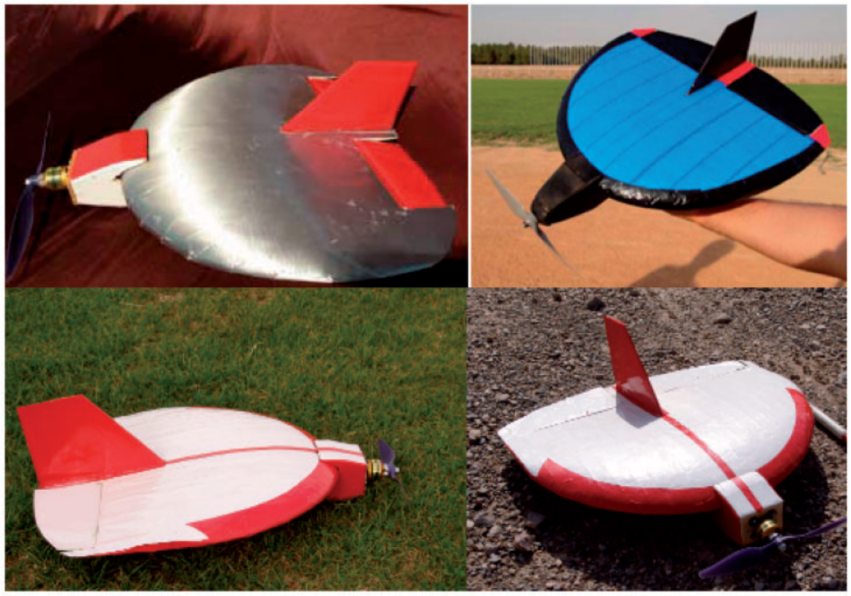

Figure 1.6 Examples of Fixed wing MAV [14].

1.5.2 Rotary wing MAVs

Rotary wings designs are inspired of large-scale helicopters. They achieve flight through the rotation of the airfoils about a vertical axis. For missions that require hovering capability and high maneuverability, they are considered as the best choice. Rotary wing MAVs can have two, three, four, five, six, eight, ten, or twelve motors. Among the rotary wing MAVs designs, the quad-copters and hexa-copters are the best-known drones [15]. Coaxial and quad copters are presented in Figure 1.7.

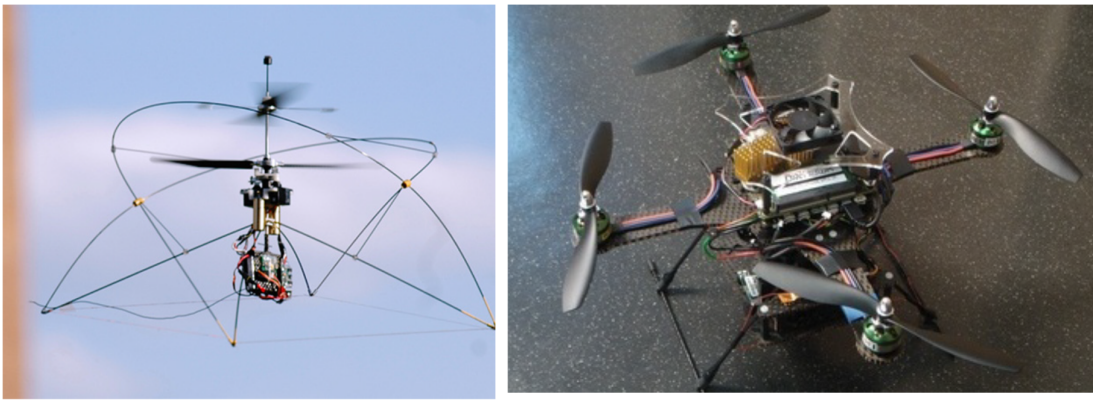

a) Co-Axial Copters (MICO [16]) Quad-copters MAV [17]

Figure 1.7 Rotary wings MAVs.

Unlike the fixed wing design, these drones can fly in all direction. This characteristic makes them the perfect drones for surveying hard-to-reach areas, such as pipelines, bridges, etc. [18, 19]. However, rotary wings produce significant level of noise, have relatively high-energy consumption and operate at low forward speed. To overcome these problems, the flapping wings design is introduced.

1.5.3 Flapping wing MAVs

Flapping wing MAVs are inspired from biological flyers' flight. They generate lift and thrust forces through oscillatory flapping motion of the wings. Flapping wing MAVs mimics birds' flight, which is characterized by wing motion in a primarily vertical plane. Flapping wing vehicles possess superior agility and efficiency compared to both rotary and fixed wing flyers. They considered among the best designs that resist efficiently the wind gusts [20]. Moreover, flapping wing configurations can be designed to move and look inconspicuous like a biological flyer. However, since the flapping flight is very complex and not fully understood yet, flapping wing MAVs are not highly recommended as the other two designs mentioned above. Only few fully operational flapping MAVs have been created. Rotary flyers have been used for decades and have established computational models. Flapping vehicles have the potential for superior maneuverability and efficiency once the aerodynamics are fully understood.

Figure 1.8 represents two views of flapping wing MAV (Thunder I) fabricated by Hassanalian Abdelkefi [21]. The tail membrane is made of Textile while the tail perimeter structure and radius ribs are made of Carbon rod.

Figure 1.8 A view of "Thunder I" flapping wing MAV [21].

1.5.4 Flapping / Fixed wing MAVs

Fixed/flapping-wing MAVs are hybrid designs that use fixed wings for lift and flapping wings for propulsion, as shown in Figure 1.9. This design consists of a low aspect ratio fixed-wing with a trailing pair of higher aspect ratio flapping wings that flap in counter phase [22].

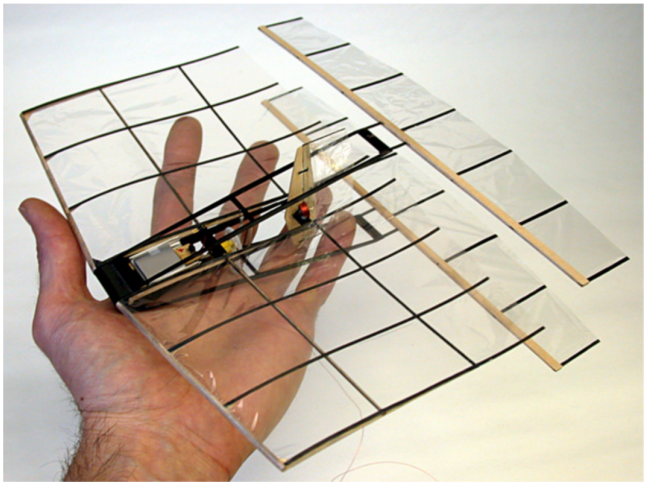

Figure 1.9 Jones' flapping wing– propelled MAV [22].

1.6 Classification of NAVs

Nano air vehicles (NAVs) are a miniature class of micro air vehicles (MAVs). NAVs are extremely small and lightweight drones with a maximum wing span length of 15 cm and a weight less than 50 g. There are different configurations for NAVs, such as fixed wings, rotary wings, and flapping wings. Only few designs flew successfully [23].

1.6.1 Flapping wing NAVs

The Nano Hummingbird shown in Figure 1.10 is an NAV funded by DARPA, presented in 2011 by AeroVironment. This vehicle mimics the flight and concept of a hummingbird [24]. It is the only flapping wing NAV capable of true hovering as well as of fight in any direction while carrying an on-board camera with live video feed.

Figure 1.10 AeroVironment NAV [24].

Inspired by the biology of a bee, researchers at the Wyss Institute are developing RoboBees (Figure 1.11), manmade systems that could perform countless roles in agriculture or disaster relief. The RoboBee's wingspan measures about 3 cm, weighs less than 80 mg, and flies using "artificial muscles" compromised of materials that contract when a voltage is applied with wingbeat frequency of 120 Hz. This RoboBees can achieve vertical take-off, hovering, and steering [25].

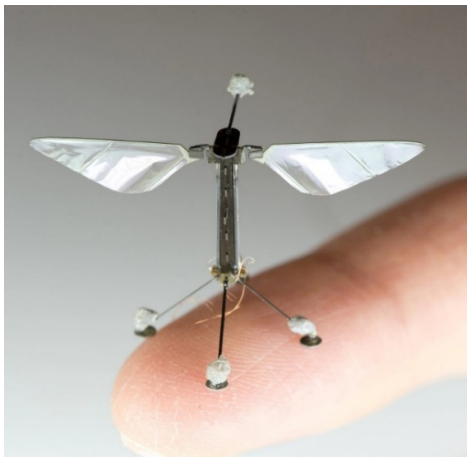

Figure 1.11 RoboBee [25].

1.6.2 Rotary wing NAVs

In addition to the flapping wing designs, the rotary wing NAVs has also been considered as successful designs. With a flight time up to 25 minutes, range of 2 Km and flight speed up to 21 Km/h, the FLIR Black Hornet PRS (shown in Figure 1.12) equips the non-specialist dismounted soldier with immediate covert situational awareness [26].

Figure 1.12 Black Hornet PRS [26].

1.6.3 Monocopter NAVs

Monocopters are single winged, all-rotating powered flight vehicles modelled after falling maple seeds. The researchers of University of Maryland have developed a robotic flying device based on samaras single-winged seeds that are released by trees (see Figure 1.13). The researchers built three robotic samaras ranging in size from 7.5 centimeters to half a meter. The robots are made out of carbon fiber and can be remotely steered by altering the wing pitch, enabling the samaras to hover, climb, and translate.

Figure 1.13 Robotic samara [27].

Nowadays, there is an increasing demand in improving the designs of flapping wing MAVs and NAVs, which is due to their impressive flight characteristics and higher flight efficiency. These designs are inspired of biological flyers flight. Therefore, the next section of this chapter investigates in details the characteristics of the flight of birds and insects.

1.7 Naturel flyers' flight

Birds and insects use the aerodynamic forces differently. Flying at high Reynolds numbers, birds only use the lift force, while reducing drag. Insects use both lift and drag, which are strongly coupled by unsteady effects generated by [28]:

- Low Reynolds number.
- High flapping frequency.
- Low aspect ratio of the wings.

Naturel flyers' flight can be divided into two categories: powered and unpowered flight

1.7.1 Unpowered Flight

1.7.1.1 Gliding

Flying animals usually flap their wings in order to generate both lift and thrust forces. However if they stop flapping and keep their wing starched out, their wings actively produce lift. The flyer generates thrust force using gravity by tilting its direction motion slightly downward relative to the air direction. The lift to drag ratio increases with the Reynolds number, which is proportional to flyer size and flight speed. For example, a wandering albatross, with a wing span of over 3 m, has a lift-to-drag ratio of 19 whereas the fruit fly, which has a span of 6 mm, has a ratio of 1.8 [29].

Flyers with high lift to drag ratio are only the ones that can glide. Therefore only large flyers can glide.

1.7.1.2 Soaring

In gliding, the animal uses the gravity force as source of power. However, in soaring flight the flyer uses the rising the energy in the atmosphere such as rising

column of air near the seas or mountains. Due to this rising air, the flyer can maintain or even gain height without flapping its wings [29].

1.7.2 Powered flight

1.7.2.1 Hovering flight

Hovering flight is the flight mode where the flyer maintains its position in calm air. During hovering flight, flyers move their wings in a complex pattern.

Whether a flying animal can hover or not, it was found that, it depends on:

- Its size, moment of inertia of the wings.
- Degrees of freedom in the movement of the wings
- Its wing shape.

Because of these limitations, hovering is mainly performed by and insects smaller birds. Larger birds can hover but only briefly.

There are two kinds of hovering, symmetric hovering and asymmetric hovering, as described by Weis-Fogh [30] and Norberg [31].

Birds for example extend their wings during the downstroke to produce more lift. During the upstroke, birds flex backward their wings to minimize the negative lift production and reduce drag (asymmetric hovering) as it is shown in the Figure bellow [32].

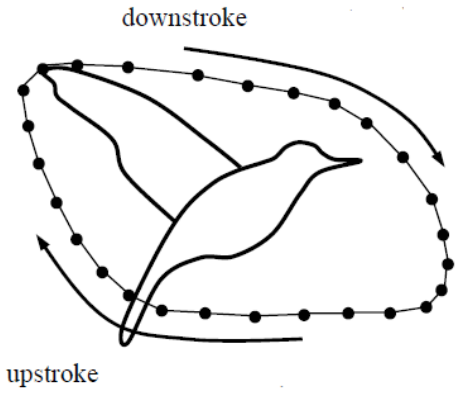

Figure 1.14 Hovering flight pattern of large birds [32].

Insects and small birds such as hummingbirds use symmetrical strokes with full-extended wings while hovering. They also tend to hover for longer period in

comparison with birds. They use the “Figure 8” pattern while flapping as it is shown in Figure 1.15 [32].

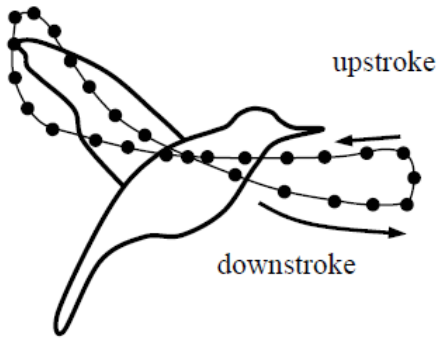

Figure 1.15 Hovering flight pattern of insects and small birds [32].

1.7.2.2 Forward flight

The important parameter in forward flight analyses is the reduced frequency, which is expressed as the ration between the forward velocity and the flapping velocity.

- Slow forward flight

The reduced frequency as well as the stroke amplitude in the slow forward flight are high. This results in high unsteady flow structures. According to Kelvin’s circulation theorem, the transverse vortices that are produced at the trailing edge connect the two tip vortices and results a shedding of a vortex ring [33].

- Fast forward flight

Unlike in the slow forward flight, the reduced frequency and the stroke amplitude in the fast forward flight are tend to be low. [33].

1.7.2.3 Cruising flight

Cruising flight is steady level forward flight in which the energy efficiency is likely to be of primary importance. The high lift peaks that come because of the development of the leading edge vortex with a cost of high drag is avoided.

Tennekes [34] considered the relations among cruising speed, weight, and wing loading, and established The Great Flight Diagram. The diagram is shown in Figure 1.16.

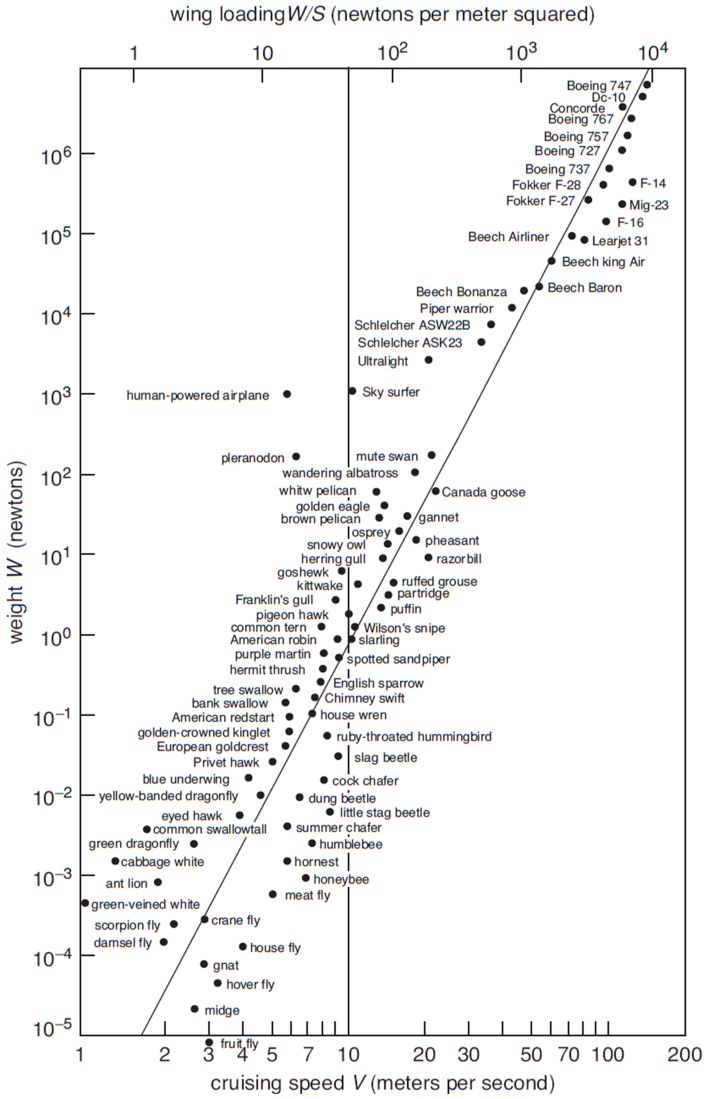

Figure 1.16 The Great Flight Diagram gives a relation among wing loading, weight [34].

1.7.2.4 Diving flight

Diving flight is a steep descent used for preying or landing. The wings are partially retracted to reduce drag. Birds control the speed and direction with the help of their tails. From the live recordings during the field experiment conducted at the Oleftal dam in Hellenthal, Germany, the dive path of a trained falcon was reconstructed and this is shown schematically in Figure 1.17. Phase 'I' shows the beginning of the stoop and 'II' is when the bird is diving at maximum speed in a T-shape configuration. Stage 'III' is when the wings are slightly deployed into the M-shape configuration and phase 'IV' where the bird starts to climb again, while flapping the wings [35].

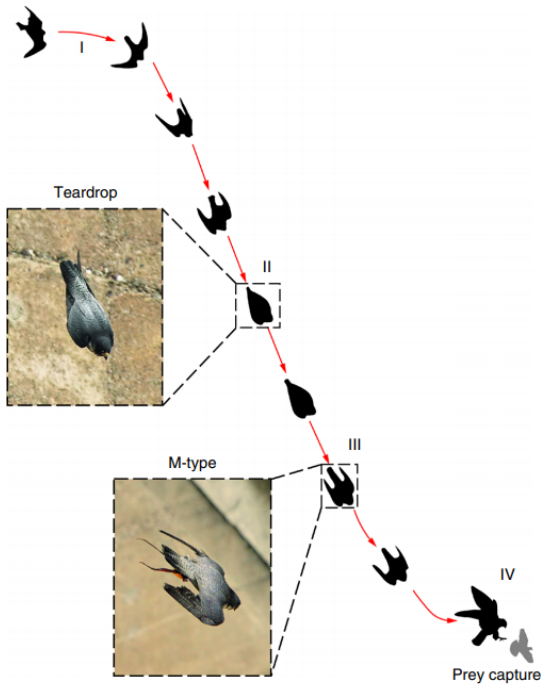

Figure 1.17 Montage of the flight path of a peregrine falcon in stoop with the corresponding live images (diving bird) [35].

1.7.2.5 Take off

During take-off, the primary requirement of lift to overcome gravity is essentially provided by a fast flapping rate, which is higher than in normal forward flight. The amplitude of flapping is also greater [36].

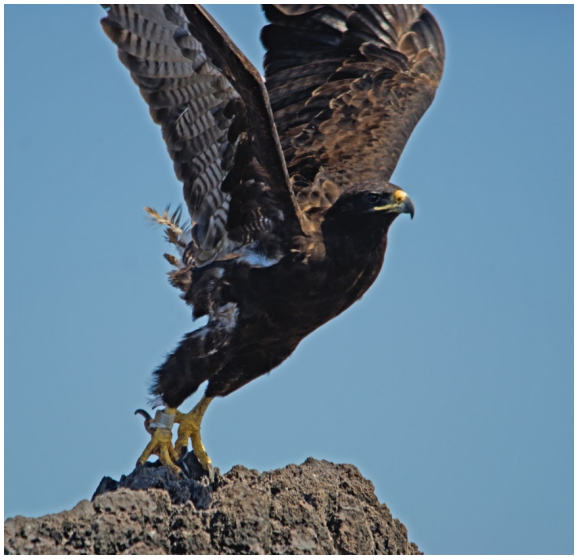

Figure 1.18 Galapagos Hawk taking off [37].

1.7.2.6 Landing

During landing, the bird's wings must generate the required lift to uphold the weight and brake the forward motion. The wings are spread wide and the flapping motion is adjusted as it is shown in Figure 1.19 [36].

Figure 1.19 Bald Eagle landing [38].

1.8 The quasi steady theory

Early models of small birds and insects' flight used the most notable analytical models, which is the "vortex models" of Ellington [39, 40] and Rayner [41]. These models are applicable for both hovering and forward flights. They could only predict the mean lift and induced power by considering the flapping wing as actuator that pushes air at a certain rate. The rate of change of momentum flux within the downward jet must be equal to the insect weight, and therefore the circulation in the wake required to maintain the force balance can be calculated, leading to an estimation of the mean lift force. These models ignored the variation in kinematics and lift generation.

The existing quasi-steady theory predicts lower lift coefficients than the required average lift coefficients for hovering as discussed by Ellington [42 ،43 ،44 ، 40] in a comprehensive review of the insect flight literature and based on a wide range of data available at that time.

In order to understand insect flight performance Dickinson et al [45] and Wang [46] applied the quasi-steady theory to compare with unsteady forces. The quasi-steady approach was then revised by Sane & Dickinson [47] to include rotational effects. However, even then the results required further improvement.

The failure of conventional quasi steady-state theories has encouraged researchers to search for the other unsteady mechanisms that might explain the high forces produced by flapping wings.

1.9 Unsteady mechanisms identified to enhance lift in insects

Based on experimental, computational and analytical models, some important unsteady mechanisms that play an important role in generating aerodynamic forces in insect flight are described below.

1.9.1 Leading edge vortices and delayed stall

For 2D airfoil traveling at high angle of attack, the pressure force created by high velocity of the fluid is much greater than the local viscous force near the leading edge of the airfoil. This results in flow separation. The low pressure on the upper side of the airfoil forces the flow to curl back and reattached on the airfoil. This forms what is called the leading edge vortex LEV. This LEV usually remains stably attached to a flapping wing after it is formed at the start of the stroke and hence it would enhance lift. [48].

The presence LEV generates a suction force on the upper side of the airfoil due to the lower pressure zone associated with the vortex core as seen in Figure 1.20.

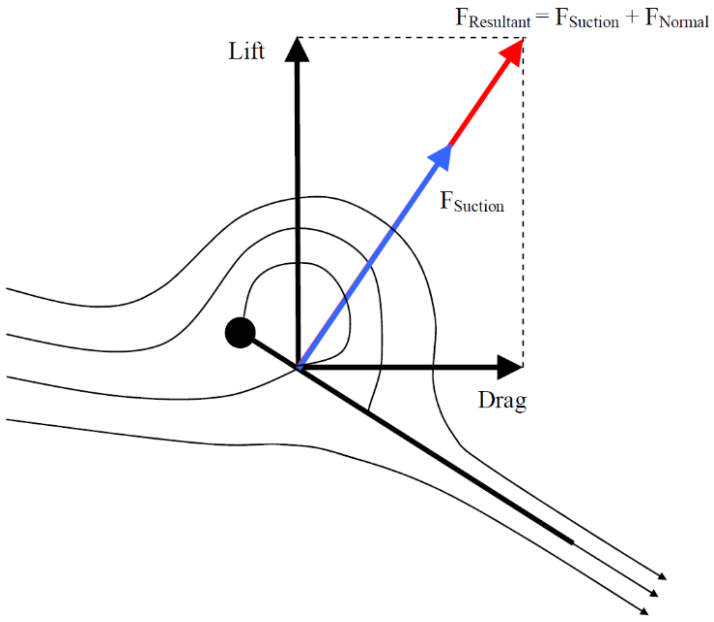

Figure 1.20 Flow around a thin airfoil [49].

Unlike in the 2D airfoil, the leading edge vortex in 3D airfoils are more stable. This is due to the axial flow that connects the LEV with the tip vortex, which forms even larger LEV.

1.9.2 Rapid pitching

At the reversal (during the end and the beginning of each stroke), the airfoil experiences a rapid rotation motion. This enhances the lift force in flying insects. Kramer [50] first demonstrated that a wing could experience lift coefficients above the steady stall value when the wing is rotating from low to high angle of attacks, which is now termed the Kramer effect. Sun and Tang [51] conducted a numerical simulation on the unsteady aerodynamic force generated by a model fruit fly wing in flapping motion. They suggested that the first peaks observed in the lift coefficient is due to rapid vorticity increase when the wing experiences fast pitch-up rotation. The pitch-up rotation and the associated vorticity increase are plotted in Figures 1.21 (f) and 1.21(g). The first peak, termed “rotational force” by Sane and Dickinson [47], appears near the end of each stroke. As shown in Figure 1.22.

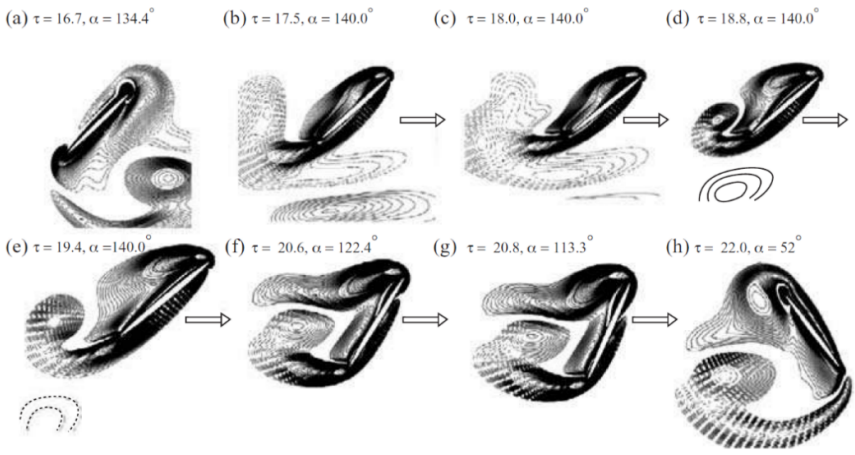

Figure 1.21 Vorticity plot around a flapping airfoil [52].

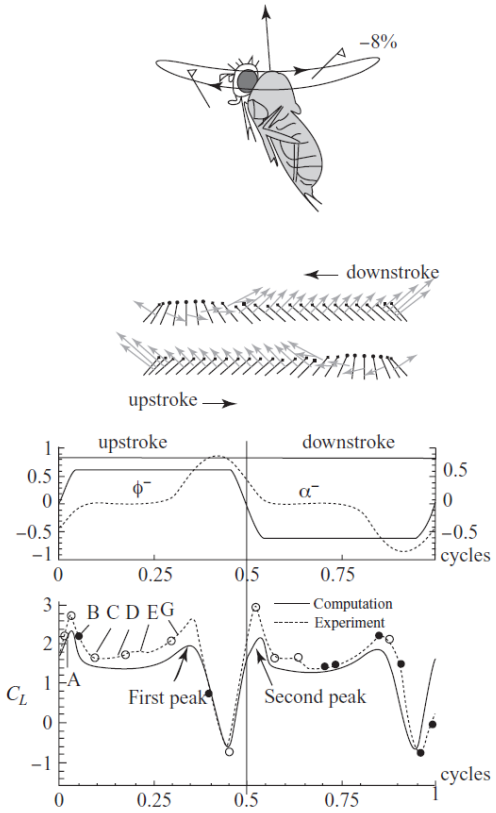

Figure 1.22 Experimental and numerical lift coefficients for a fruit fly-modelled wing [51].

1.9.3 Wake capturing

Contrary to aircrafts with fixed wings that move through still air, the wings of hovering insects interacts with the wake created by the wing in the previous stroke. The wing–wake interaction can significantly contribute to lift production in hovering insects. Wake capture is often beneficial, but can be detrimental dependent on the specific flapping kinematics. It can be beneficial only when it increases the flow velocity thus increasing lift.

The wing capture mechanism is illustrated in Figure 1.23. At the beginning, the wing is in steady translation (A). Then, as the wing moves forward, the training and leading edges vortices begin to form (B). At the end of the forward stroke the leading and training adage vortices are shed and the flow field is induced (C). After the wing reverse its direction (D), the wing encounters the induced field velocity. Fluid momentum is transferred to the wing that generates a peak in the aerodynamic (E). [49].

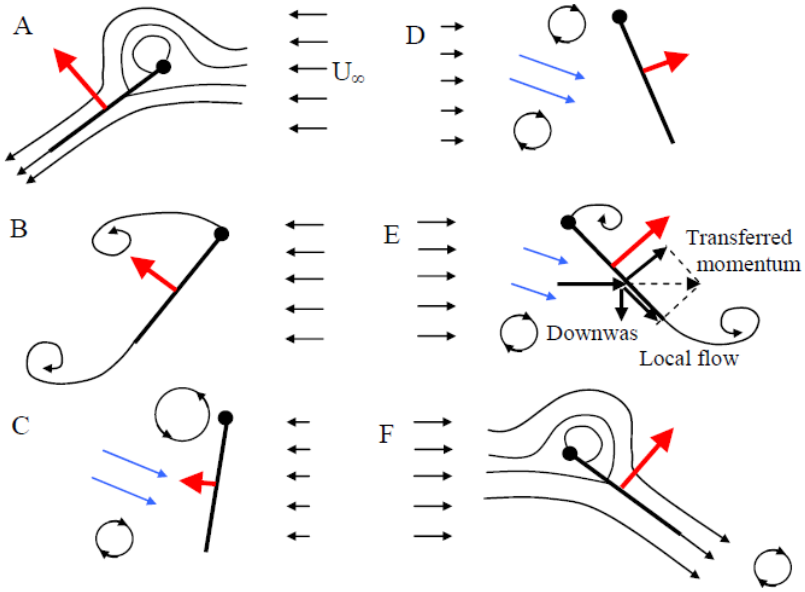

Figure 1.23 Momentum transfer due to wing-wake interaction. Sketched from Sane [49].

1.9.4 Clap and fling

The clap-and-fling mechanism is the physical interaction of the left and right wing during dorsal stroke reversal. This mechanism was proposed by Weis-Fough [30] to explain the lift generation in the chalcid wasp. Its schematic is presented in Figure. 1.24.

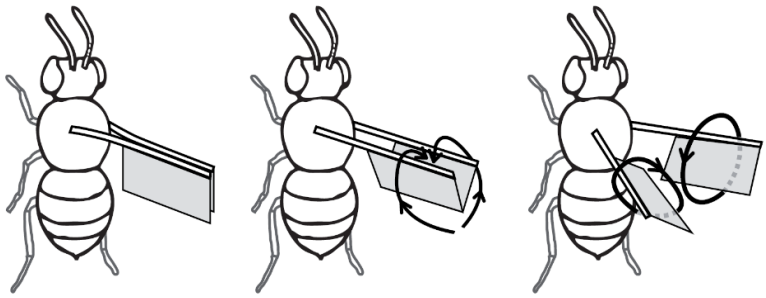

Figure 1.24 Clap and fling mechanism. Left [30].

The wings clap together at dorsal stroke reversal. Middle: The leading edges initiate the downstroke and air is sucked into the gap. Right: Positive circulation is generated instantly [30].

This mechanism was also found in fruit flies [53] and butterflies [54].

The fling phase preceding the downstroke is thought to enhance circulation that is due to fluid inhalation in the split formed by the moving wings (d), which causes a strong vortex generation at the leading edge. The schematic shown in Figure 1.25 demonstrates this mechanism in details.

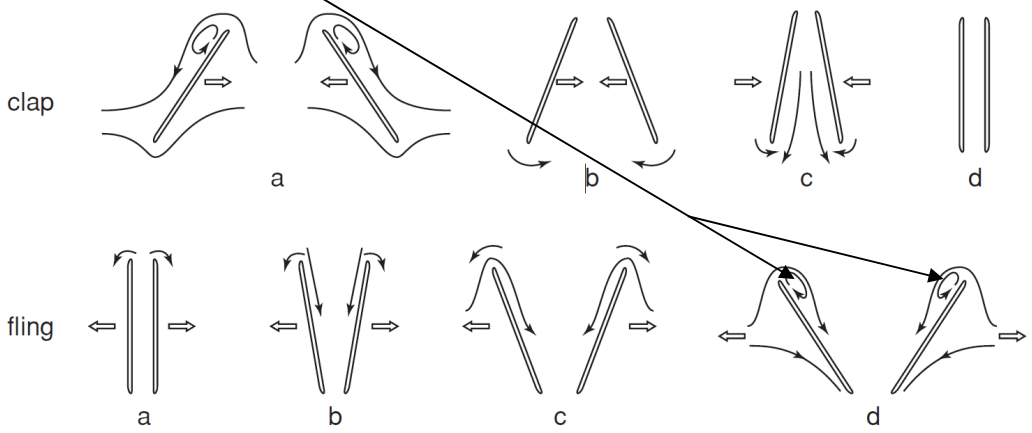

Figure 1.25 Schematic of clap and fling mechanism. Based on Weis-Fough [30].

CHAPTER 2: LITERATURE REVIEW

2.1 Introduction

To provide some perspective on the current state of the art in flapping wing MAVs, it is useful to examine the existing works that have already been accomplished by a variety of research groups. First, the numerical and experimental studies regarding the effects of the ground on 2D airfoil in hovering flight are briefly presented. Next, the numerical as well as the experimental works on the effect of the wing spacing and phase difference between the fore and hind wings are highlighted. Finally, the effects of the asymmetry of the downstroke ration on an isolated wing in inclined flapping motion are presented.

2.2 Numerical and experimental studies on the ground effects in hovering flight

The ground effect is one of the important parameters that influences drastically the aerodynamic performance. Among the first researchers who conducted a detailed study on the ground effects were **Moryossef and Levy** [55]. They investigated numerically the effects of the ground on the flow field an around oscillating airfoil. **Gao and Lu** [56] conducted a study on the insect normal hovering mode considering the ground. They concluded that the high lift force is produced in the case of advanced rotation and small amplitude of rotation. **Molina and Zhang** [57] examined numerically the effects of an inverted airfoil under vertical plunging motion in ground effect. They identified three different mechanisms occurring at different flow regimes (the ground effect, the incidence effect and the added mass effect). A numerical investigation of a flapping-flying model based on real birds flying characteristics under the effects of the ground was examined by **Su et al** [58]. They found that flying near the ground increases the lift force by 47% while the drag force

decreases by 20%. A hovering foil near the ground with a flexible tail at Reynolds number of 100 was numerically investigated by **Wu et al** [59]. They found that when the distance between the foil and the ground decreases, three force regimes are reproduced (force enhancement, force recovery and force reduction). In addition, the flexible tail found to be the main responsible for the lift enhancement as well as the reduction of the drag and the energy required to put the airfoil in motion. **Lu et al** [60] studied the ground effect on 3D wing with different hovering flight kinematics. They concluded that the effect of the ground on a 3D wing is insignificantly larger when it is compared with a case of 2D wing.

2.3 Numerical studies on flapping tandem wing configuration in forward flight

Dragonflies have always amazed the scientists due to their outstanding flight skills. They are able to switch their flight mode from hovering to forward to backward without changing their posture [61, 62]. Scientists observed that the dragonflies use a phase difference between their wings to achieve an optimal flight. Moreover, dragonflies stroke their wings in inclined direction, which led many scientists to investigate the role-played by the stroke angle, phase difference between the wings, and the distance between the two wings on the aerodynamic generation [63].

Many numerical studies have been done on the effects of the wing spacing and the phase difference on the aerodynamic performance and the flow structure. **Shilong and Mao** [64] studied the flow structure and the aerodynamic forces generated by single and tandem wing in forward flight, where only the effects of the phase difference between the forewing and hind wing were considered. They found that for the case of a single wing, the aerodynamic coefficients were significantly larger than what was predicted by the steady state analyses. Furthermore, for the case of tandem wing configuration, they found that when the two wings flap simultaneously, the aerodynamic forces were similar to that of single wing configuration. However, when the two wings flap in counter stroking, the lift force of the hindwing in downstroke and the thrust force on the forewing in upstroke are decreased .**Huang and Sun** [65] conducted a numerical simulation on a cross section of two dragonfly wings in forward flight. The simulation took in consideration the effects of the phase difference and the advance ratio. They found that at a positive angle difference, the lift and the thrust forces were slightly influenced by the wake interaction with the wings. However, at a negative phase difference, they

found that the mean lift force was significantly decreased. In order to understand the effects of the wing spacing and the phase difference on the aerodynamic forces at Re=5000. **Broering and Lian** [66] conducted a 2D numerical simulation on tandem wing configuration in forward flight. They found that the vortex interaction (vortex/wing and vortex/vortex) had a major influence on the lift and thrust generation and the formation of the leading edge vortex. They also found that for a phase difference of 90° had similar effects as of a wing spacing of 0.75. Moreover, **Broering and Lian** [67] conducted also a 3D simulation on the effects of the wing spacing and phase difference. They found that a 3D simulation resulted in a spanwise variation in the LEV structure and a weaker LEV formation at midspan compared with their previews 2D simulation results. This variation resulted in a weaker vortex interaction compared with the results predicted by 2D analysis. **Tay** [68] investigated numerically the effects flexibility and kinematic motions of wing-wing interaction in hovering flight. The author found that a rigid spanwise and flexible chordwise wing produce the highest lift with minimum energy consumption. **Shanmugan and Sohn** [69] performed a numerical investigation on the benefits of the wing-wing interaction of a dragonfly-like flapping wing on the aerodynamic performance in hovering flight. They identified two new flow features namely the “enhanced dipole” and “in-sync wake capture as well as the wing-wing interactions” that participate in a significant increase of the lift generation.

2.4 Experimental studies on flapping tandem wing in forward flight

In addition to the aforementioned numerical studies, many experimental investigations have been done on tandem wing configuration. **Zheng et al** [70] measured experimentally the force applied on flexible tandem wings in both hovering and forward flights. They used three flexible dragonfly-like tandem wing models differentiated by the degree of flexibility by varying their thicknesses. They found that the flexibility had an important role in generating high aerodynamic forces. Their results showed that the wing with the lowest flexibility had higher thrust generation in the forward flight. The PIV and deformation measurements results offered a better insight on how the flexibility affects the aerodynamic performance of the tandem wings. **Lua et al** [71] conducted an experimental and numerical investigation on tandem wing configuration in forward flight. They concluded that depending on how and when the hindwing interact with the wake produced by the

forewing, the thrust generation could be either higher or lower than that of the single wing configuration. **Li et al** [72] conducted an experimental and numerical investigation on a dragonfly during take-off. Two high-speed cameras were used to record the body motion of the dragonfly during take-off. They found that the maximal vertical acceleration can reach 20 m/s2, the phase difference between the fore and hind wings varies from 0° to 110° and the angle of attack during the first two beats was found to be greater than the following beats. However, due the experimental limitations, a numerical analysis was also added to their paper, where ellipse tandem wing configuration with thickness ration of 0.1 was used. The Reynolds number was fixed at 157. Their results showed that a large angle of attack generates higher lift force but smaller thrust, which explains why dragonflies beat with higher angle of attack during the take-off. **Li and Dong** [73] measured the wing kinematics and the aerodynamics of a dragonfly in turning flight. They found that dragonflies use phase difference and stroke asymmetry during turning maneuvers.

2.5 Numerical studies on the effects of the asymmetry of downstroke ratio

The asymmetry in the flapping duration is common in insect flight [44, 74]. Some numerical studies on the effects of asymmetrical stroke on a single wing is reported in the following. **Zhu et Zhou** [75] investigated the effects of the asymmetry of the downstroke duration on the aerodynamic performance of a single wing in both hovering and forward flights. They chose three different Reynolds numbers (Re=15.7, Re=157 and Re=1570). They found that for the case of hovering flight, only at low Reynolds (Re=15.7) the aerodynamic performance can benefit from the asymmetry. Moreover, for the forward flight, they found that the thrust and lift generation cannot benefit from the asymmetry simultaneously. In addition, **Wang et al** [76] added to the previous study, the effects of the asymmetry in the angle of attack. Their results showed that the larger the angle of attack during the downstroke, the higher the lift coefficient and the lift efficiency is produced. Moreover, the larger angle of attack during the upstroke the higher the thrust coefficient and thrust efficiency are generated.

2.6 Summary

From the aforementioned studies, it can be seen that the effects of the ground on the so called “water treading” hovering flight has not been studied before. In

addition, the effects of the asymmetry in flapping duration, initial position and the asymmetry in flapping frequency on tandem wing configuration have not been investigated before as well. For this reason, the influence of these parameters on the aerodynamic performance is considered in this study.

CHAPTER 3: MATHEMATICAL MODEL

3.1 Computation techniques

In order to understand the aerodynamics of flapping wing MAVs, accurate calculation methods are needed. However, it is far more difficult to simulate the aerodynamics around flapping wings than the conventional fixed wing. This is due to the small size of MAVs and their complex low Reynolds number flow aerodynamics

Viscous flow, unsteady flow, transition to turbulence, and vortical structures are some of the aerodynamics that must be accurately predicted to understand the flow. Small changes in these computation parameters can have a significant effect on the overall flow. The complex aerodynamics increase the computational cost requirements needed to evaluate the flow. Accurate, but cost effective computational techniques are required to evaluate the flow [77] .

3.2 Characteristics of MAVs flow at low Reynolds number

3.2.1 Incompressible Flow

All fluids are compressible at high enough pressures. Since low Reynolds number flow is so slow for MAV applications, the air compression is negligible [78].

3.2.2 Unsteady Flow

Unsteady flow is common in flapping flight aerodynamics. Often small disturbances in the aerodynamics can cause a significant change in overall aerodynamic performance. The aerodynamics of a flapping cycle can influence the aerodynamics of the next cycle. [79].

3.2.3 Viscous/Inviscid

Viscosity is the tendency of a fluid to resist deformation due to bonding within the fluid. In the conventional fixed wing flight, this parameter is usually negligible. However, at low Reynolds number flow, the viscous forces have a more noticeable effect on the aerodynamics. [80].

To solve the flow around a flapping wing, Ansys Fluent is often used due to the variety of options that provides especially the User Defined Function (UDF) that offers total freedom in controlling the wing's motion.

3.3 Ansys Fluent

ANSYS Fluent is a computational fluid dynamics (CFD) software solution used to predict flow, turbulence, heat transfer and reactions for industrial applications. Fluent has a record of outstanding parallel scalability, enabling high fidelity results in the shortest possible time.

Fluent uses finite-volume method that discretizes the spatial domain using a mesh. Variable values for quantities such as mass, energy, momentum are stored in these control volumes constructed with the help of the mesh.

3.4 Finite volume method

The Finite Volume Method (FVM) is a numerical technique that transforms the partial differential equations representing conservation laws over differential volumes into discrete algebraic equations over finite volumes (or elements or cells).

It is considered as one of the most adaptive discretization techniques used in CFD. The discretization method is consist of few steps:

1- The first step is the discretization of the geometric domain, which, in the FVM, is discretized into finite volumes.
2- The partial differential equations are then transformed into algebraic equations by integrating them over each discrete element.
3- The system of algebraic equations is then solved to compute the values of the dependent variable for each of the elements [81].

Some of the terms in the conservation equation are turned into face fluxes and evaluated at the finite volume faces. Because the flux entering a given volume *n* is identical to that leaving the adjacent volume, FVM is strictly conservative. This

conservation property of the FVM makes it the preferred method in CFD. FVM it is quite easy to implement a wide variety of boundary conditions. This is because the unknown variables are evaluated at the centroids of the volume elements, not at their boundary faces [81].

All of the characteristics mentioned above made the Finite Volume Method quite suitable for the numerical simulation of a variety of applications involving fluid flow and heat and mass transfer.

3.5 Governing Equations of Fluid Flow

Many flow related problems can be described using transport equations. Transport equations are modelled in different ways, depending on the considered phenomenon, their form can differ. However, with the same set of operators, the behavior of dependent variables in all such equations can be described. This allows the formulation of the generic scalar transport equation. The standard form of scalar transport equation is expressed as [82]:

$$\frac{\partial(\rho\phi)}{\partial t} + \nabla . (\rho\vec{v}\emptyset) = \nabla . (\Gamma\nabla\emptyset) + S_{\emptyset} \qquad (3.1)$$

where $\emptyset$ represents the transported scalar variable, ρ is the fluid density, $\vec{v}$ is the velocity vector ($= u\vec{\imath} + v\vec{\jmath}$), Γ is the diffusion coefficient and $S_{\emptyset}$ is the source term.

3.6 Discretization process

The numerical solution of a partial differential equation consists of finding the values of the dependent variable ϕ at specified points from which its distribution over the domain of interest can be constructed. In all methods, the focus is on replacing the continuous exact solution of the partial differential equation with discrete values. The distribution of ϕ is hence discretized, and it is appropriate to refer to this process of converting the governing equation into a set of algebraic equations for the discrete values of ϕ as the discretization process and the specific methods employed to bring about this conversion as the discretization methods.

The discrete values of ϕ are typically computed by solving a set of algebraic equations relating the values at neighboring grid elements to each other; these discretized or algebraic equations are derived from the conservation equation governing ϕ. Once the values of ϕ are computed, the data is processed to extract

any needed information. The various stages of the discretization process are illustrated in Figure 3.1 [81].

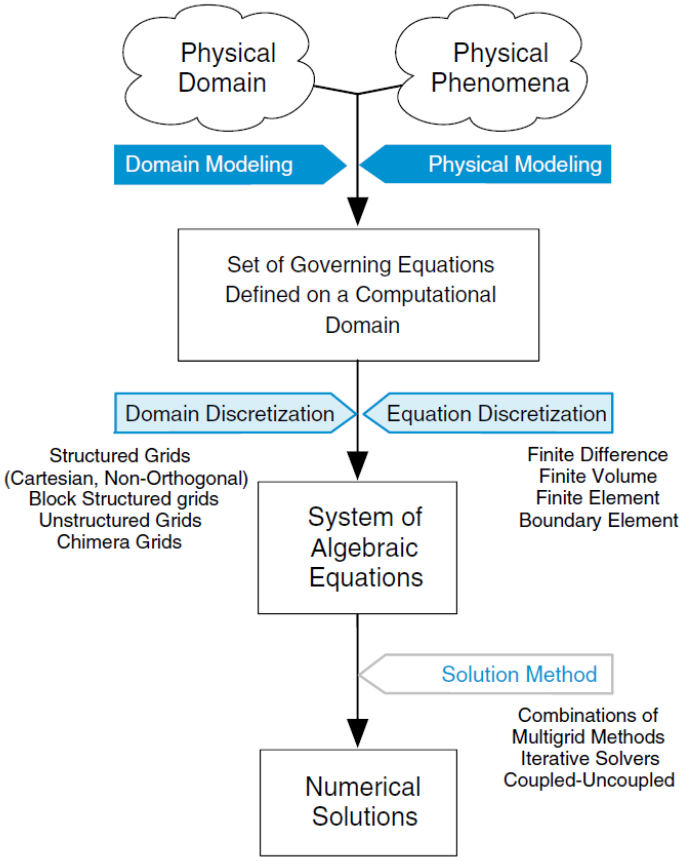

Figure 3.1 The discretization process [81].

The discretization of the conservation equation for transport of a scalar quantity ϕ is demonstrated by the following equation written in integral form for an arbitrary control volume V:

$$\int_V \frac{\partial(\rho\phi)}{\partial t} dV + \oint \rho\vec{v}\phi \,.\, d\vec{A} = \oint \Gamma\nabla\phi \,.\, d\vec{A} + \int_V S_\phi \, dV \qquad (3.2)$$

This equation is applied to each control volume, or cell, in the computational domain.

$$\frac{\partial(\rho\phi)}{\partial t} V + \sum_f^{N_{faces}} \rho_f \, \vec{v}_f \phi_f . \vec{A}_f = \sum_f^{N_{faces}} \rho_f \; \Gamma_f \nabla \phi_f . \vec{A}_f + S_\phi \, V \qquad (3.3)$$

Where N_{faces} is the number of faces enclosing cell, $\emptyset_f$ is the value of $\emptyset$ converted through face f, $\rho_f \vec{v}_f . \vec{A}_f$ is the mass flux through the face, $\vec{A}_f$ is the area of face f, $\nabla \emptyset_f$ is the gradient of $\emptyset$ at face f.

A schematic of two dimensional, triangular cells is shown in Figure 3.2.

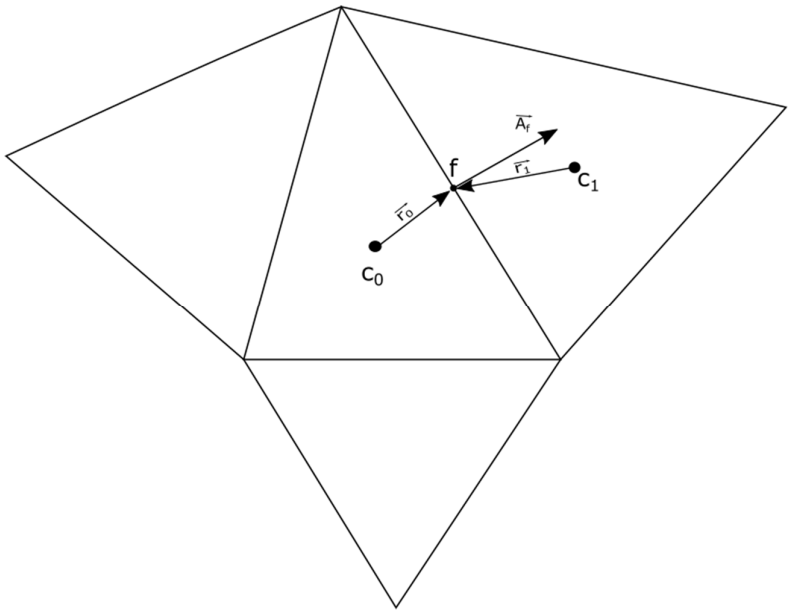

Figure 3.2 Control Volume of two-dimensional triangular cells.

3.6.1 Spatial Discretization

ANSYS Fluent stores discrete values of the scalar $\emptyset$ at the cell centers by default (c_0 and c_1 in Figure 3.2). However, face values are required for the convection terms in equation (3.3) and must be interpolated from the cell center values. This is accomplished using an upwind scheme [83].

ANSYS Fluent allows choosing several upwind schemes:

- First-order upwind.
- Second-order upwind.
- QUICK.

3.6.1.1 First-Order Upwind Scheme

When selecting the first order upwind scheme, the quantities at cell faces are determined by assuming that the cell center values of any field variable represent a cell-average value and hold throughout the entire cell. The face quantities are

identical to the cell quantities. Thus, when first-order upwind is selected, the face value $\emptyset_f$ is set equal to the cell-center value of $\emptyset$ in the upstream cell [83].

3.6.1.2 Second-Order Upwind Scheme

When selecting the second-order scheme, the quantities at cell faces are computed using a multidimensional linear reconstruction approach [84]. In this approach, higher-order accuracy is achieved at cell faces through a Taylor series expansion of the cell-centered solution about the cell centroid. Thus when second-order upwind is selected, the face value $\emptyset_f$ is computed using the following expression:

$$\emptyset_f = \emptyset + \nabla \emptyset . \vec{r} \qquad (3.4)$$

Where

$\emptyset$ and $\nabla \emptyset$ are the cell-centered value and its gradient in the upstream cell.

$\vec{r}$ is the displacement vector from the upstream cell centroid to the face centroid. This formulation requires the determination of the gradient $\nabla \emptyset$ in each cell. This scheme is the one selected in this study.

3.6.1.3 QUICK Scheme

ANSYS Fluent also provides the QUICK scheme for computing a higher-order value of the convected variable $\emptyset$ at a face. QUICK-type schemes are based on a weighted average of second-order-upwind and central interpolations of the variable. However, this scheme can be applied only on quadrilateral (2D) and hexahedral (3D) meshes [85].

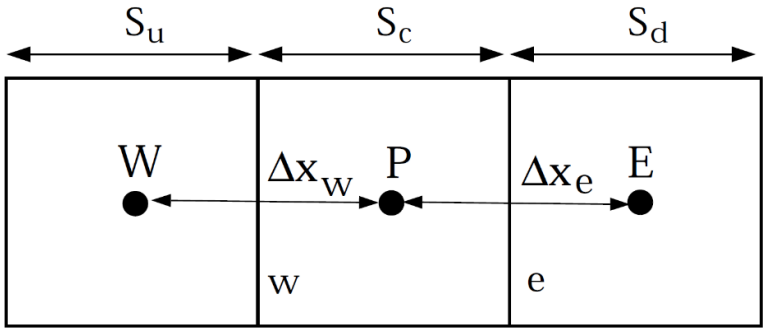

Figure 3.3 One-Dimensional Control Volume [83].

If the flow is one directional from left to right for a control volume shown in Figure 3.3, the face *e* can be written as:

$$\emptyset_e = \theta\left[\frac{S_d}{S_c+S_d}\emptyset_P + \frac{S_c}{S_c+S_d}\emptyset_E\right] + (1-\theta)\left[\frac{S_u+2S_c}{S_u+S_C}\emptyset_P - \frac{S_c}{S_u+S_C}\emptyset_W\right] \quad (3.5)$$

- θ =1 in the above equation results in a central second-order interpolation .
- θ =0 results in a second order upwind value.
- θ=1/8 results in the traditional QUICK scheme.

3.6.2 Temporal Discretization

When a transient simulation is chosen, the governing equations must be discretized in both space and time. The spatial discretization for the time-dependent equations is identical to the steady-state case. Temporal discretization involves the integration of every term in the differential equations over a time step Δt.

A generic expression for the time evolution of a variable ∅ is given by:

$$F(\emptyset) = \frac{\partial \phi}{\partial t} \quad (3.6)$$

where the function F incorporates any spatial discretization. If the time derivative is discretized using backward differences:

- The first-order accurate temporal discretization is given by:

$$F(\emptyset) = \frac{\emptyset^{n+1}-\emptyset^n}{\Delta t} \quad (3.7)$$

- The second-order discretization is given by:

$$F(\emptyset) = \frac{3\,\emptyset^{n+1}-4\emptyset^n+\,\emptyset^{n-1}}{2\,\Delta t} \quad (3.8)$$

where *n+1* is the value at the next time level ($t + \Delta t$), n is the value at current level (t), n-1 is the value at the previous time level ($t - \Delta t$) [83].

3.6.2.1 Implicit Time Integration

One method is to evaluate $F(\emptyset)$ at the future time level

$$F(\emptyset^{n+1}) = \frac{\emptyset^{n+1}-\emptyset^n}{\Delta t} \quad (3.9)$$

This is referred to as “implicit” integration since $\emptyset^{n+1}$ in a given cell is related to $\emptyset^{n+1}$in neighboring cells through $F(\emptyset^{n+1})$:

$$\emptyset^{n+1} = \emptyset^{n} + \Delta t\, F(\emptyset^{n+1}) \quad (3.10)$$

This implicit equation can be solved iteratively at each time level before moving to the next time step.

The advantage of the fully implicit scheme is that it is unconditionally stable with respect to time step size [83].

The explicit time integration is only available when the density-based solver is chosen, while the second order implicit scheme is not compatible with the overset meshing method

3.6.3 Discretization of the Momentum Equation

The x momentum equation can be obtained by setting $\emptyset$ as u:

$$a_P \emptyset = \sum_{nb} a_{nb} \emptyset_{nb} + b \quad (3.11)$$

$$a_P u = \sum_{nb} a_{nb} u_{nb} + \sum P_f A \,.\, \vec{\imath} + S \quad (3.12)$$

If the pressure field and face mass fluxes are known, the previous equation can be solved as outlined in the discretization process mentioned above. However, if the pressure field and face mass fluxes are not known, a priori and must be obtained as a part of the solution [83].

3.6.3.1 Pressure Interpolation Schemes.

For interpolating the pressure values at the faces, ANSYS Fluent offers several options. By default, the Second Order scheme is used:

- The Linear scheme computes the face pressure as the average of the pressure values in the adjacent cells.
- The Standard scheme interpolates the pressure values at the faces using momentum equation coefficients

$$P_f = \frac{\frac{P_{c0}}{a_{p.c0}} + \frac{P_{c1}}{a_{p.c1}}}{\frac{1}{a_{p.c0}} + \frac{1}{a_{p.c1}}} \quad (3.13)$$

- The Second Order scheme reconstructs the face pressure using a central differencing scheme. The pressure values at the faces are given by:

$$P_f = \frac{1}{2}(P_{c0} + P_{c1}) + \frac{1}{2}(\nabla P_{c0}.\vec{r}_{c0} + \nabla P_{c1}.\vec{r}_{c1}) \quad (3.14)$$

This scheme may provide improved accuracy over the Standard and Linear schemes. This is the reason why this scheme was selected in this study.

- The PRESTO! (PREssure STaggering Option) scheme uses the discrete continuity balance for a "staggered" control volume about the face to compute the "staggered" pressure. This procedure is similar in spirit to the staggered-grid schemes used with structured meshes.

The PRESTO! scheme is available for all meshes [86].

3.6.4 Discretization of the Continuity Equation

Considering the steady state continuity equation in integral form:

$$\oint \rho\vec{v}.d\vec{A} = 0 \quad (3.15)$$

Integrating this equation over the control volume shown in Figure 3.1 gives the following discrete equation:

$$\sum_f^{N_{faces}} J_f A_f = 0 \quad (3.16)$$

Where J_f is the mass flux through face f.

First, it is necessary to relate the face values of velocity $\vec{v}_n$, to the stored values of velocity at the cell centres. The linear interpolation of cell-cantered velocities to the face results in unphysical checker boarding of pressure. For this reason, ANSYS Fluent uses a procedure similar to that outlined by Rhie and Chow [87] to prevent checker boarding. The face value of velocity is not averaged linearly instead, momentum-weighted averaging, using weighting factors based on the coefficient from Equation (3.12), is performed. Using this procedure, the face flux, J_f is written as:

$$J_f = \rho_f \frac{a_{P.c0}\, v_{n.c0} + a_{P.c1}\, v_{n.c1}}{a_{P.c0} + a_{P.c1}} + d_f\left((P_{c0} + (\nabla p)_{c0}.\overrightarrow{r_0}) - (P_{c1} + (\nabla p)_{c1}.\overrightarrow{r_1})\right) \quad (3.17)$$

$$J_f = \hat{J}_f + d_f(P_{c0} - P_{c1}) \quad (3.18)$$

where P_{c0}, P_{c1} and $v_{n,c0}, v_{n,c1}$ are the pressures and normal velocities, respectively, within the two cells on either side of the face, and $\hat{J}_f$ contains the influence of velocities in these cells. The term d_f is a function of $\overline{a}_P$, the average of the momentum a_p coefficient for the cells on either side of face f [83].

3.7 Pressure-Velocity Coupling

To achieve the pressure-velocity coupling, the equation (3.17) is used to derive an additional condition for pressure by reformatting the continuity equation (3.18).

ANSYS Fluent provides the option to choose five pressure-velocity coupling algorithms: SIMPLE, SIMPLEC, PISO, Coupled and Fractional Step (FSM) [83]. The coupled Algorithm is the one chosen in this study for the reasons mentioned below.

3.7.1 Coupled Algorithm

Many advantages can be taken from the coupled algorithm that are been offered in the non-coupled methods.

By using the coupled scheme:

- A robust and efficient single-phase implementation for steady-state flows obtains.
- A superior performance compared to the segregated solution schemes.
- Offers an alternative to the SIMPLE algorithm in both pressure and density based solvers.
- When the quality of the mesh is poor, or if large time steps are used, using the coupled algorithm becomes necessary, especially for transient flow.
- The pressure-based segregated algorithm solves the momentum equation and pressure correction equations separately. This semi-implicit solution method results in slow convergence. However, the coupled algorithm solves the momentum and pressure-based continuity equations together. [83].

In the momentum equations (3.12), the pressure gradient for component k is of the form

$$\sum_f P_f A_k = -\sum_j a^{u_k P} P_j \qquad (3.19)$$

Where $a^{u_k P}$ is the coefficient derived from the Gauss divergence theorem and coefficients of the pressure interpolation schemes (Equation 3.13). Finally, for any *i* cell, the discretized form of the momentum equation for component u_k is defined as

$$b_i^{uk} = \sum_j a_{ij}^{u_k u_k} u_{kj} + \sum_j a_{ij}^{u_k p} P_j \qquad (3.20)$$

In the continuity equation (3.16), the balance of fluxes is replaced using the flux expression in equation 3.17.

Resulting in the following discretized form

$$b_i^P = \sum_K \sum_j a_{ij}^{puk} u_{kj} + \sum_j a_{ij}^{pp} P_j \qquad (3.21)$$

As a result, the overall system of equations (3.20 and 3.21) after being transformed to the δ form, is presented as

$$\vec{B}_i = \sum_J [A]_{ij} \vec{X}_j \qquad (3.22)$$

where the influence of a cell i on a cell j has the form

$$A_{ij} = \begin{bmatrix} a_{ij}^{pp} & a_{ij}^{pu} & a_{ij}^{pv} & a_{ij}^{pw} \\ a_{ij}^{up} & a_{ij}^{uu} & a_{ij}^{uv} & a_{ij}^{uw} \\ a_{ij}^{vp} & a_{ij}^{vu} & a_{ij}^{vv} & a_{ij}^{vw} \\ a_{ij}^{wp} & a_{ij}^{wu} & a_{ij}^{wv} & a_{ij}^{ww} \end{bmatrix} \qquad (3.23)$$

and the unknown and residual vectors have the form

$$\vec{X}_j = \begin{bmatrix} p_i' \\ u_i' \\ v_i' \\ w_i' \end{bmatrix} \quad , \vec{B}_i = \begin{bmatrix} -r_i^p \\ -r_i^p \\ -r_i^v \\ -r_i^w \end{bmatrix} \qquad (3.24)$$

3.8 Under relaxation factors

Since the solution was stable and converged without any difficulties, the relaxation factors were kept as default values.

3.9 Navier Stokes Equations

The governing equations for fluid flow, heat and mass transfer, as well as other transport equations can be represented by the conservative form equation 3.2. Where $\emptyset, \Gamma \text{ and } S_\phi$ are replaced as shown in table 3.1

Table 3.1 Corresponding $\emptyset$ for transport equation.

Equation	$\emptyset$	Γ	S_ϕ
Continuity	1	0	0
Momentum	$\vec{v}$	μ	$-\nabla p + \nabla\vec{\tau} - \nabla.(\mu\nabla\vec{v}) + \rho\vec{g}$

As heat transfer was not considered in this thesis, the energy conservation equation is excluded.

For incompressible laminar flow, the Navier stokes equations become

- Continuity equation:

$$\nabla . U = 0 \qquad (3.25)$$

- Momentum equation:

$$\frac{\partial U}{\partial t} + \nabla . (UU) = -\frac{\nabla P}{\rho} + \upsilon \nabla^2 U \qquad (3.26)$$

For a 2D case under Cartesian coordinating system, the N-S equations can be written as follows

Continuity equation:

$$\frac{\partial u}{\partial x} + \frac{\partial v}{\partial y} = 0 \qquad (3.27)$$

Momentum equation:

$$\frac{\partial u}{\partial t} + \frac{\partial uu}{\partial x} + \frac{\partial uv}{\partial y} = -\frac{1}{\rho}\frac{\partial P}{\partial x} + \frac{\partial}{\partial x}\left(\upsilon\frac{\partial u}{\partial x}\right) + \frac{\partial}{\partial y}\left(\upsilon\frac{\partial u}{\partial y}\right) \qquad (3.28)$$

$$\frac{\partial v}{\partial t} + \frac{\partial vu}{\partial x} + \frac{\partial vv}{\partial y} = -\frac{1}{\rho}\frac{\partial P}{\partial y} + \frac{\partial}{\partial x}\left(\upsilon\frac{\partial v}{\partial x}\right) + \frac{\partial}{\partial y}\left(\upsilon\frac{\partial v}{\partial y}\right) \qquad (3.29)$$

where *u* , *v* , *w are* the velocity components of U in Cartesian coordinate system, υ is the kinematic viscosity.

3.10 Dimensionless numbers

In general, the relative relevance of the different terms in equations (3.25) and (3.26) is revealed by making those equations dimensionless. Therefore, the main variables, *U, t, X, P* and ρ are scaled with their reference values as follows:

$$U^* = \frac{U}{U_{ref}} \tag{3.30}$$

$$t^* = t \,.\, f_{ref} \tag{3.31}$$

$$x^* = \frac{x}{L} \tag{3.32}$$

$$P^* = \frac{P}{P_{ref} \cdot U_{ref}^2} \tag{3.33}$$

The star (*) is used to indicate the dimensionless variables. When substituting the last four equations into equations (3.25) and (3.26), the following non-dimensional form of the incompressible continuity and momentum equations is obtained:

$$\nabla \,.\, U^* = 0 \tag{3.34}$$

$$St\frac{\partial U^*}{\partial t} + \nabla \,.\, (U^* U^*) = -\nabla P^* + \frac{1}{Re}\nabla^2 U \tag{3.35}$$

In these equations, two main dimensionless numbers are identified as relevant parameters, the Strouhal (St) and Reynolds number (Re).

3.11 Parameter definition

The two important parameters for the analysis of the flow around a rigid airfoil in both hovering and forward flight modes are the Reynolds number and the reduced frequency. The Reynolds number is defined as:

$$Re = \frac{\rho U_{ref} c}{\mu} \tag{3.36}$$

where ρ is the fluid density (Kg/m^3), μ is the dynamic viscosity of the fluid (Kg/m.s) , c is the chord length of the wing (m)(reference length) and $U_{ref}$is the reference velocity (m/s). U_{ref} is defined as the maximum translational velocity of the wing :

$$U_{ref} = \frac{2\,\pi\,A_m}{T} \tag{3.37}$$

The reduced frequency represents the ration between the forward velocity and the flapping velocity,

$$K = \frac{\pi f c}{U_{ref}} \tag{3.38}$$

The advance ratio *j* characterizes the forward flight and it is defined as:

$$j = \frac{U_0}{U_{ref}} \tag{3.39}$$

where U_0 represents the inlet velocity, which is chosen to be the quarter of the reference velocity.

The Strouhal number corresponds to ratio of the vertical distance travelled by the tip of the wing during the flapping stroke ($f\ A_m$) over the speed of the animal *(U_0).*

$$St = \frac{2\,f\,A_m}{U_0} \tag{3.40}$$

Biologists and engineers, have observed that most flying and swimming animals oscillate their wings or tails in a narrow range of Stroughal number between 0.2 and 0.4, where propulsive efficiency is high [88].

The thrust, lift and resultant coefficients were calculated numerically using:

$$C_t = -\frac{F_x}{0.5\,\rho {U_0}^2 c} = -\frac{F_T}{0.5\,\rho {U_0}^2 c} \tag{3.41}$$

$$C_l = \frac{F_y}{0.5\,\rho\,{U_{ref}}^2 c} = \frac{F_L}{0.5\,\rho\,{U_{ref}}^2 c} \tag{3.42}$$

$$C_r = \frac{\sqrt{{F_T}^2+{F_L}^2}}{0.5\,\rho\,{U_{ref}}^2 c} \tag{3.43}$$

where F_T, F_L, F_R represent the thrust, lift and resultant forces respectively.

The pressure coefficient was calculated numerically using:

$$C_{pr} = \frac{P-P_\infty}{0.5\,\rho {U_0}^2} \tag{3.44}$$

The instantaneous energy consumption was calculated by this formula:

$$P(t) = -[\underbrace{F_{flap}\, v(t)}_{\substack{power\ required \\ for\ displacement}} + \underbrace{M_a\, \omega(t)}_{\substack{power\ required \\ for\ rotation}}] \quad (3.45)$$

where $F_{flap}$is the resultant of the flapping force in the stroke direction, $v(t)$ is the translation velocity, $\omega(t)$ is the rotation velocity of the airfoil and M_a is the rotation moment with respect to the center of the wing. M_a is calculated by:

$$\overrightarrow{M_a} = \overrightarrow{M_o} + \overrightarrow{R_{ao}} \wedge \vec{F} \quad (3.46)$$

where $M_o$is the moment with respect to the origin given by the software, and R_{ao} is the vector from the origin to the center of the airfoil.

The energy coefficient was calculated numerically by:

$$C_p = \frac{P(t)}{0.5\ \rho\ {U_{ref}}^3 c} \quad (3.47)$$

The thrust, lift and resultant coefficients for the combined wings were calculated using

$$C_T = -\frac{F_{Df}+F_{Dh}}{0.5\ \rho {U_0}^2 (c_f+c_h)} \quad (3.48)$$

$$C_L = \frac{F_{Lf}+F_{Lh}}{0.5\ \rho {U_0}^2 (c_f+c_h)} \quad (3.49)$$

$$C_R = \frac{\sqrt{(F_{Df}+F_{Dh})^2+(F_{Lf}+F_{Lh})^2}}{0.5\ \rho {U_0}^2 (c_f+c_h)} \quad (3.50)$$

where the indices *h* and *f* represent the fore and hind wings.

The thrust, lift and resultant efficiencies were calculated by

$$\eta_T = \frac{\overline{C_T}}{\overline{C_p}} \quad (3.55)$$

$$\eta_L = \frac{\overline{C_L}}{\overline{C_p}} \quad (3.51)$$

$$\eta_R = \frac{\overline{C_R}}{\overline{C_p}} \quad (3.52)$$

CHAPTER 4: Effects of the ground on an airfoil under two hovering modes at Re=100

4.1 Introduction

In this chapter, we study the effects of the ground on the flow around an airfoil undergoing two hovering modes, “water treading” and “normal” modes. In order to have a better insight into the effects of the ground on the lift production as well as the energy consumption, the ground clearance (D) is varied from D=1c to D=5c with an interval of 0.5c. Moreover, the effects of the ground on the vorticity contours and the pressure distribution on the airfoil are also studied. The case with no ground effects is also considered which will be used as a reference for comparison. A finite volume method is used to simulate the flow field using a commercial software Fluent.

4.2 Kinematic description and boundary conditions

The “water treading” mode was first identified by Freymuth in his experiments. This mode resembles to action of the ventral fins of fishes for stable positioning in still water [89].

The same motion is also used by swimmers to keep themselves float when their body is upright. The airfoil motion consists of a translation and a rotation where the airfoil is placed horizontally at the reversal of each stroke. The translation and rotation components are presented in the following equations

$$h(t) = h_a.sin(2\pi ft + \varphi) \quad (4.1)$$

$$\alpha(t) = \alpha_0 - \alpha_a.sin(2\pi ft) \quad (4.2)$$

where, *h(t)* is the instantaneous translation amplitude, $h_a$is the translation amplitude, $\alpha(t)$is the instantaneous angle of rotation, α_0 is initial angle of rotation, $\alpha_a$is the angle of rotation amplitude, and φ is the phase difference between the translation and rotation motion. In this case $\alpha_0 = 0°$ and $\varphi = 90°$.

The schematic of the motion is shown in Figure 4.1.

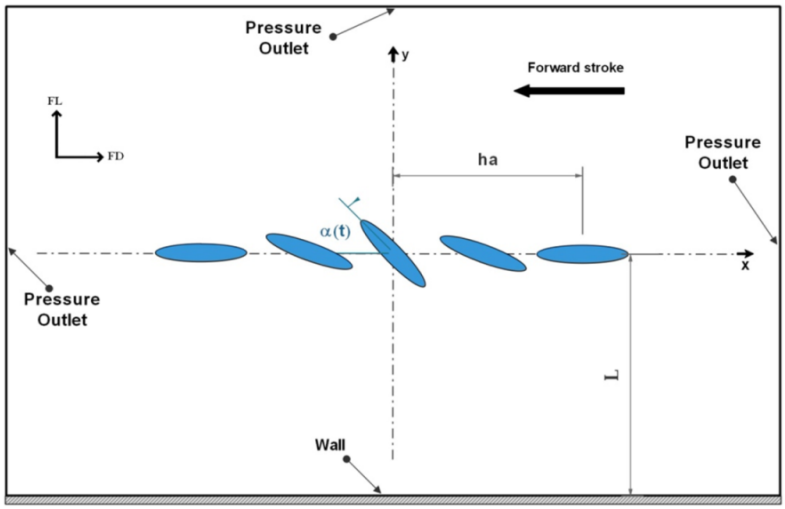

Figure 4.1 Scheme of the “water treading” hovering mode.

For the second part of this study, “normal” hovering mode is considered. Similar as in the first mode, the airfoil motion is also consists of translation and rotation. However, in this mode the airfoil is placed vertically at the end of each stroke. The Equations (4.3) and (4.4) describing the airfoil motion as:

$$h(t) = h_a.sin(2\pi\, f\, t + \varphi) \tag{4.3}$$

$$\alpha(t) = \alpha_0 + \alpha_a.sin(2\pi f t) \tag{4.4}$$

The schematic of the “normal” hovering motion is shown in Figure 4.2.

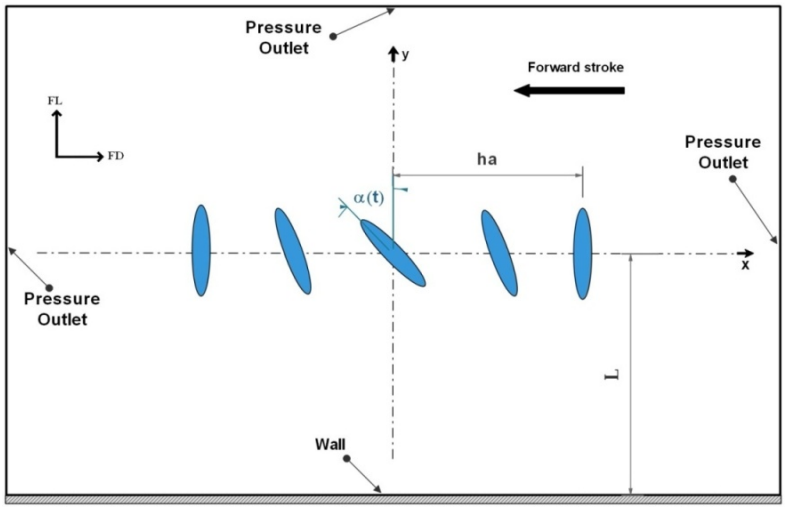

Figure 4.2 Scheme of “normal” hovering mode.

No-slip wall boundary condition is applied on the surface of the wing as well as on the ground at the bottom of the fluid domain. There is no free stream in the hovering flight mode. Therefore, the boundary condition applied on the rest of the domain is pressure outlet as 0 Pa, which resembles to atmospheric pressure.

Most small insects fly at Reynolds number ranging from 100 to 200 [90]. Re=100 corresponds to the Fruit fly flight regime [91], therefore the flow field is investigated at $Re = 100$. The stroke kinematics are set as $h_a = 1.4c$, f=1.66 Hz, c=0.01 m and $\alpha_a = 90°$. The initial angle of rotation for the "water treading" mode $\alpha_0 = 0^0$, while the initial angle of rotation for the "normal" mode $\alpha_a = 90°$. The phase difference between the translation and rotation $\varphi = 90^0$.

The wing motion was handled using a user defined function (UDF), where the macro function DEFINE_CG_MOTION is used for both the translation and rotation of the wing. This Macro requires only velocity equations, where in our case they are taken from the derivation of the displacement equations for (4.1), (4.2), (4.3) and (4.4).

The mathematical description of the translation and rotation velocities for the "water treading" mode are:

$$V(t) = 2\,\pi\,f\,h_a\,cos(2\,\pi\,f\,time\,+\varphi) \tag{4.5}$$

$$\omega(t) = -2\,\pi\,f\,\alpha_a\,cos(2\,\pi\,f\,time) \tag{4.6}$$

While the mathematical description of the translation and rotation velocities for the "Normal" mode are:

$$V(t) = 2\,\pi\,f\,h_a\,cos(2\,\pi\,f\,time\,+\varphi) \tag{4.7}$$

$$\omega(t) = 2\,\pi\,f\,\alpha_a\,cos(2\,\pi\,f\,time) \tag{4.8}$$

The time history of the translation displacement and rotation angle as well as the translation and the rotation velocities are presented in Figure. (4.3) and Figure (4.4) respectively.

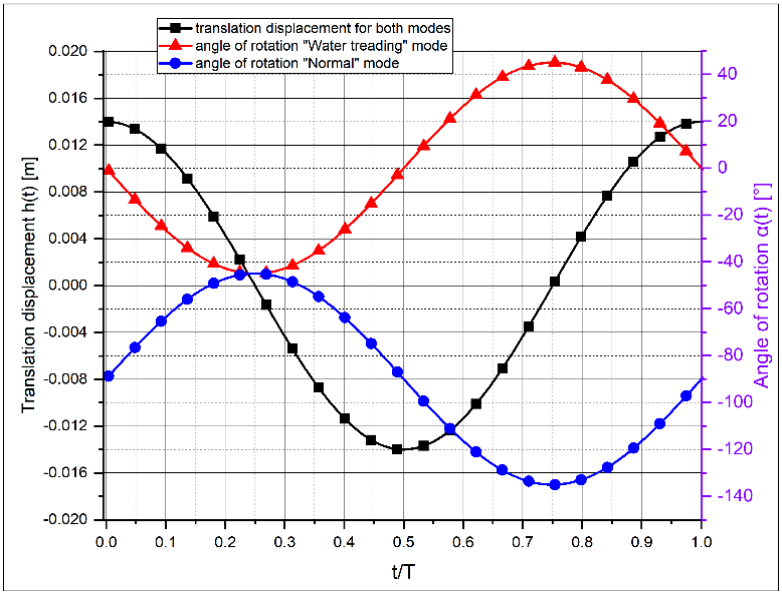

Figure 4.3 Time histories of translation displacement and angle of rotation for the two hovering modes.

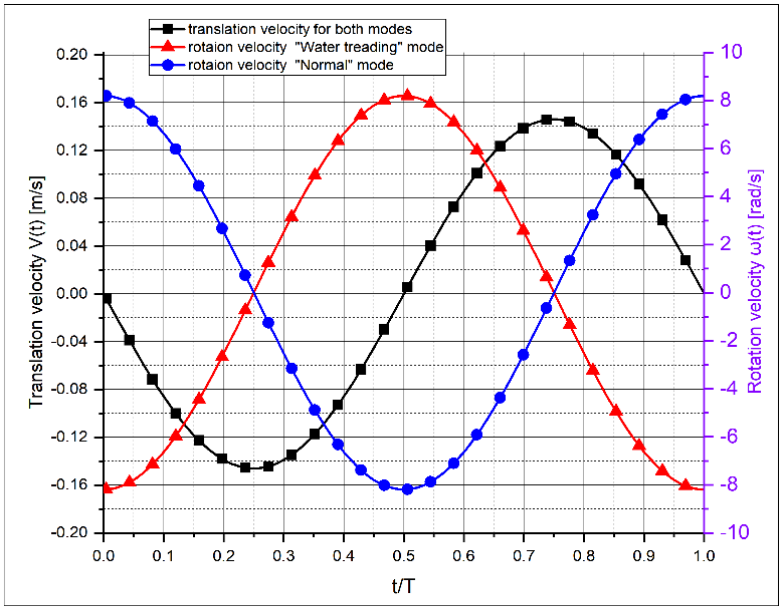

Figure 4.4 Time histories of translation velocity and angular velocity for the two hovering mode.

4.3 Mesh generation

In order to achieve more accurate results especially when the stroke axis is situated closer to the ground, an overset mesh is used, which consists of two domains. An O-shape grid was used for the first domain near the airfoil surface, which is refined drastically in order to capture the steep gradients near airfoil surface. For the second

domain, a structured quadratic mesh refined near the ground was used as shown in Figure 4.5. On Fluent, a moving boundary can be achieved using three methods: remeshing, deformation and oversetting. The deformation of the mesh method allows the use of a quadratic grid but results in highly unstructured mesh. The remeshing method can be applied only on a triangular grid and results on unstructured mesh as well. The overset mesh method guaranties a structured quadratic grid for the long of the stroke period, as shown in Figure. 4 5(b).

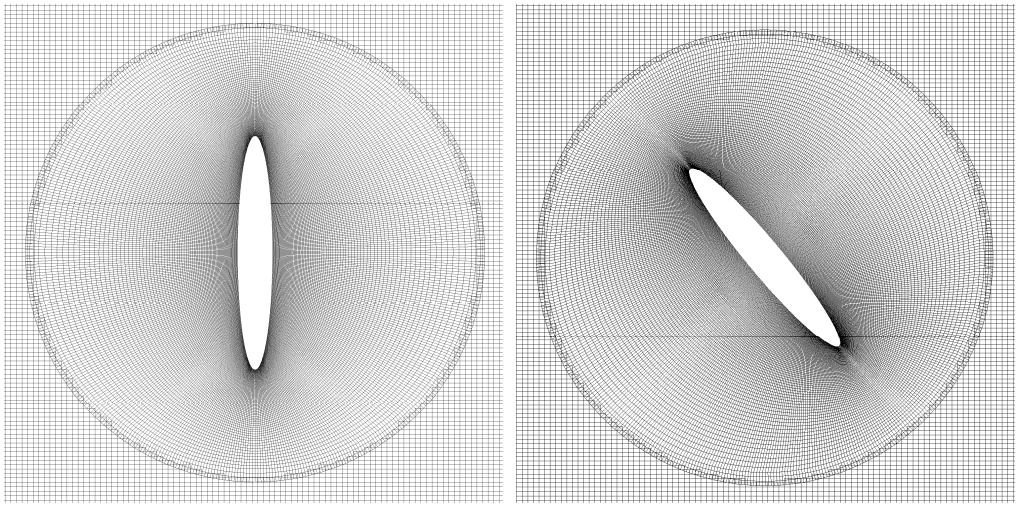

(a) **(b)**

Figure 4.5 close-up view of the mesh near the wing surface, (a) at t/T=0, (b) at t/T=0.25.

4.4 Grid independency analysis

Grid independence study was conducted first to determine the appropriate mesh size. The spatial accuracy of the present algorithm was examined by employing three grid size levels.

Figure 4.6 represents the different grid used in the grid independency study.

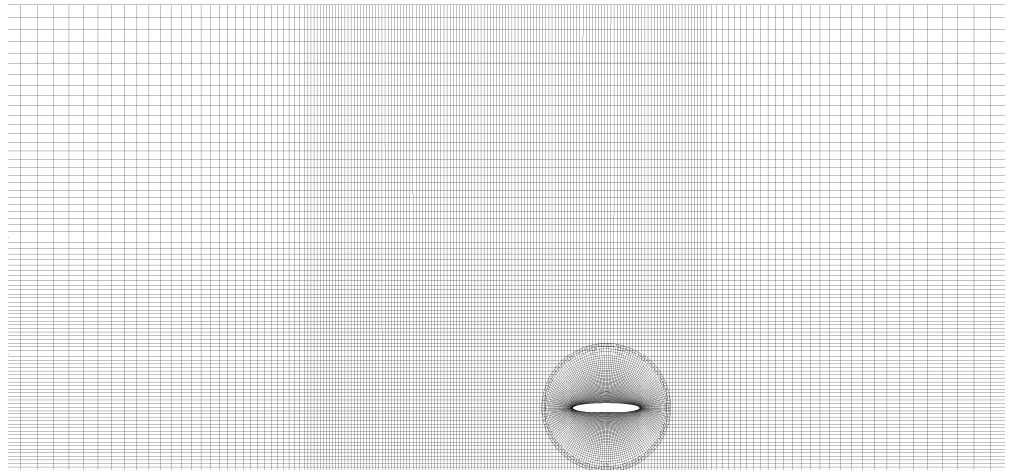

(A)

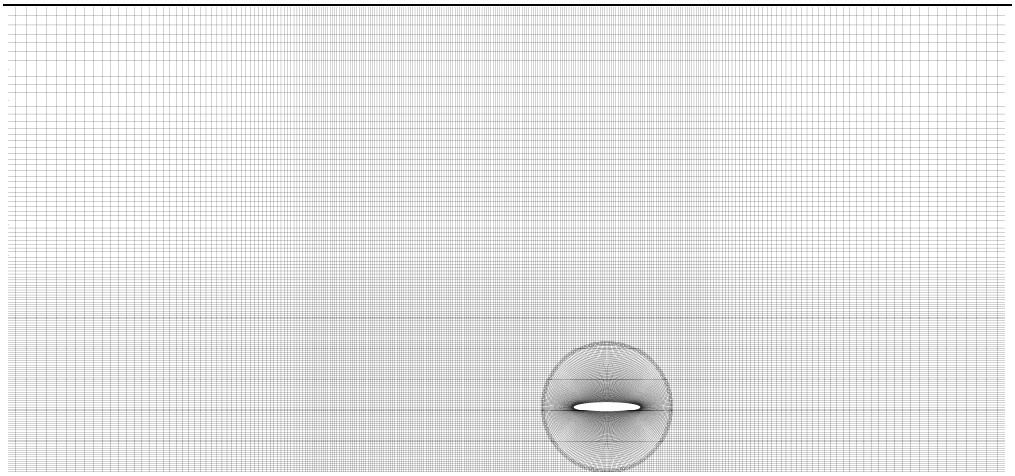

(B)

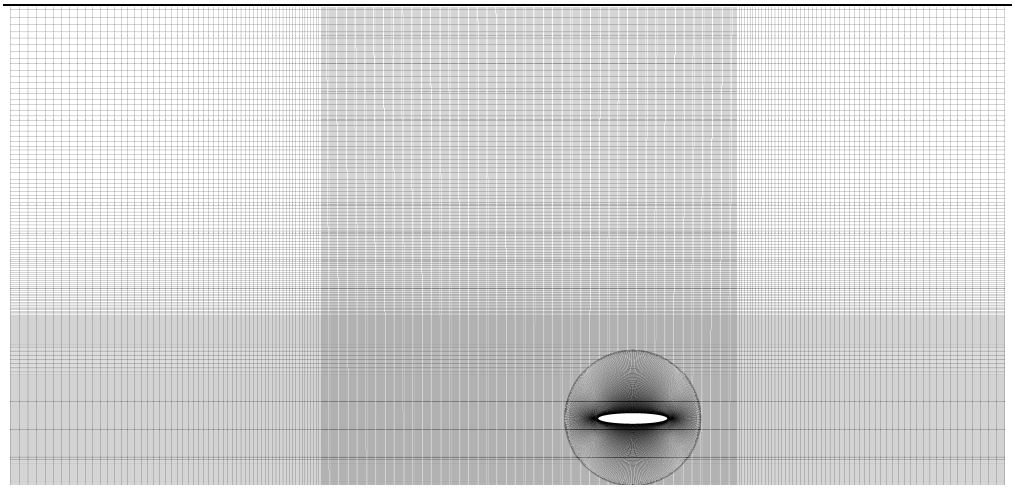

(C)

Figure 4.6 Computational mesh, (A): coarse grid, (B): intermediate grid, (C) Fine grid.

Details regarding the number of elements and nodes as well as average lift coefficient obtained and the computational cost in each analysis are mentioned in Table 4.1. A medium grid distribution with 98 145 cells was refined and coarsened with ratio of 2 to be used as coarse and fine grids respectively (Table 4.1).

Table 4.1 Grid independence study for the case of "water treading" hovering mode at Re=100, h_a=1.4c, α_0=0°, α_a=45°, D=1c.

Grid	Number of elements	Number of nodes	Average lift coefficient $\bar{C}_l$	Difference of $\overline{\lvert C_l \rvert}$ compared with the ultra fine mesh %	Number of periods	Number of logical processors (I7 HQ 4700)	Computational time (hrs)
Coarse	45 970	46 630	1.334	3.317%	20	5	18
Intermediate	98 145	99 072	1,296	0.033%	20	5	26
Fine	206 680	208 023	1.291		20	4	46

Figure 4.7 shows the lift coefficient history obtained with three different grid resolutions.

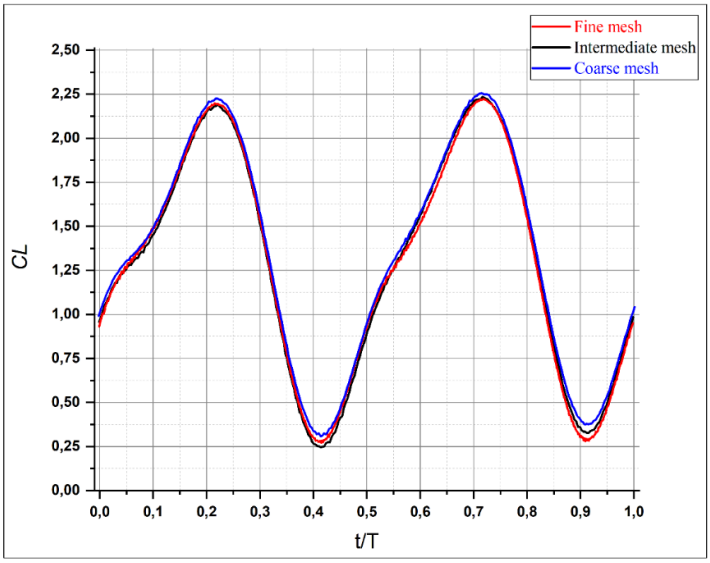

Figure 4.7 Lift coefficient for three different grid size for the case of the "water treading mode at L=1c.

As observed in Figure. 4.7 and Table 4.1, the intermediate grid gives satisfactory balance between numerical accuracy and computational cost. The results

also indicate that reasonable grid independency was obtained, taking into account the unsteadiness of the flapping flight.

4.5 Comparison with Similar Work

The present work was first validated through a comparison with a typical work studied by many researchers, Wang et al [76], Xu and Wang [92] and Gao and Lu [56]. The kinematic parameters used were $A_m = 1.25c$, $\alpha_m = 30°$, $\alpha_m = -45°$ $\alpha_0 = -30°$ $\beta = 60°$ and Re=157. The present results showed a good agreement with the previous results, as it is shown in Figure.4.8.

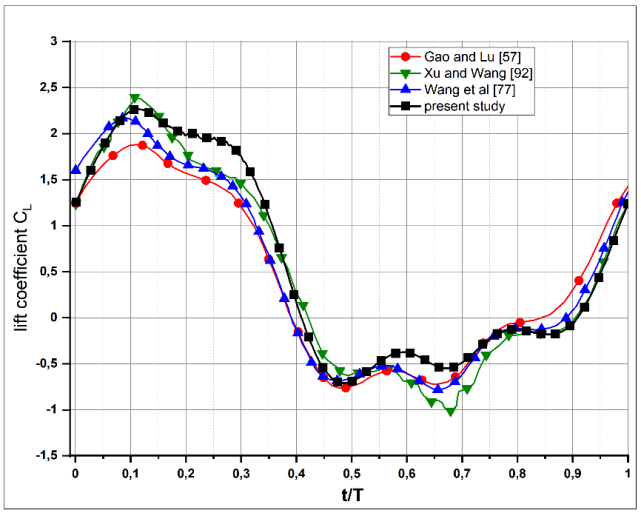

Lift Coefficient

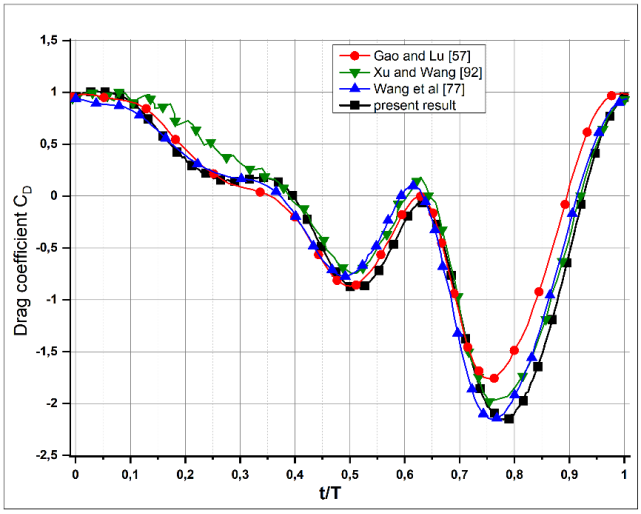

Drag coefficient

Figure 4.8 Comparison of the time histories of the lift and drag coefficients of the present study with the results obtained from the literature.

4.6 Results and discussion

The ground effect on the flow around an elliptic airfoil with two different hovering modes (“water tread” and the “normal” hovering mode) are presented next. The results were taken after the 20th cycle to ensure the periodic state is reached. In order to explain the lift force results obtained in this study, the pressure distribution on the airfoil and the vorticity contours are studied in details.

4.6.1 Water treading hovering mode in ground effect

The time dependent lift coefficient values are plotted in Figure 4.9. The first thing to notice is that the lift peak value is reached before the airfoil attaining the middle of the forward stroke for the case of D=1c (Cl=2.22 at t=0.21T). As the ground clearance increases, the lift peak position moves forward in time and its value decreases till it reaches the lower value at D=3.5c. The vorticity contours for four different values of ground clearance D is presented in Figure 4.10 and Figure 4.11, the blue color represents the clockwise vorticity contours, while the red color represents the counter clockwise vorticity contours.

At the beginning of the stroke the airfoil is placed horizontally, and then accelerates while rapidly pitches up. The flow around the airfoil edges speeds up which leads to the beginning of the formation of the leading and trailing edge vortices (LEV and TEV) as it is labelled with red and blue curved arrows on the vorticity contours at time (a) and (b). The presence of the ground had a significant effect on the strength and magnitude of these vortices.

Due to the strong relation between the vorticity contours and the pressure distribution on the airfoil surfaces, the pressure distribution on both the upper and the lower sides of the airfoil are presented in Figure 4.12. Four time instants are selected for the analysis of both hovering modes, *t(a)= 0.08T, t(b) =0.17T, t(c)= 0.25T, t(d)= 0.45T*.

At D= 1c, the presence of counter clockwise vortex (CCW) on the on the top of the newly formed LEV increases its magnitude as it can be seen in Figure 4.10 at time (a). This resulted in lower pressure distribution on the upper side of the airfoil as the black dashed arrows indicate in Figure 4.12.

It is also noticed that the presence of the ground interrupts the induced flow created by airfoil movement. This increases the pressure on the lower side of the airfoil

(Cushion effect) as it is indicated in Figure 4.12 (a) and (b) with the black arrows. At the reversal, it is noticed that the magnitude of the recirculation bubble on the upper side of the airfoil is affected by the ground clearance distance.

Larger LEV on the top of the airfoil combined with the cushion effect led to a significant increase of lift production. This explains the higher peaks in the lift coefficient at D=1c (Figure 4.9). It is also observed that the TEV shed from the previous stroke moves sideways, driving by the reflected downwash due to the presence of the ground. However, as the ground clearance increases, the previously shed TEV moves downward which reduces the cushion effects. As a result, the lift generation decreases (see Figure 4.9).

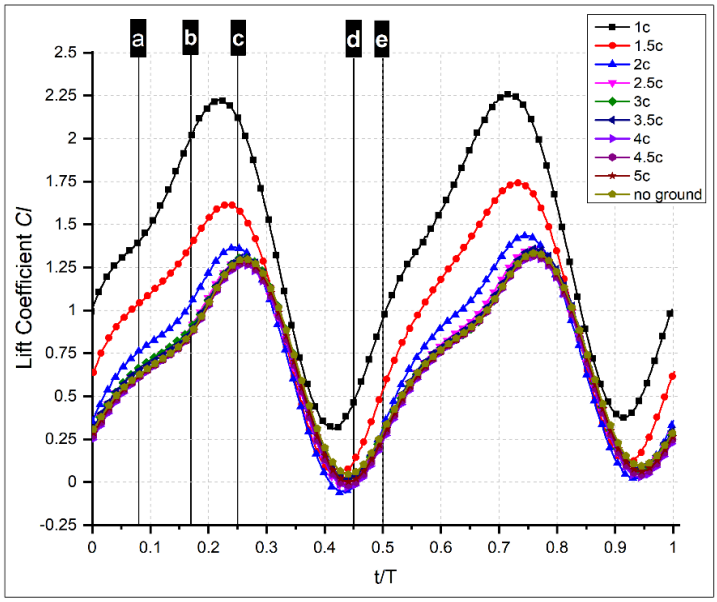

Figure 4.9 Lift coefficient of “water treading” hovering mode.

The high pressure distribution on the lower side of the airfoil due to the cushion effect combined with the low pressure zone create by the larger resulted in higher lift coefficient at the beginning of the stroke for D=1c (Cl=1). The ground effect disappears beyond D=2c, as the vortices contours and the pressure distribution show in Figure 4.11 and Figure 4.12. For this reason, only one regime is identified in this mode, which is the enhancement regime. No wing-wake interaction is observed as the vorticity contours show. This resulted in just one lift peak at each half stroke as shown in Figure 4.9. The lift pattern remained identical for all different values of D.

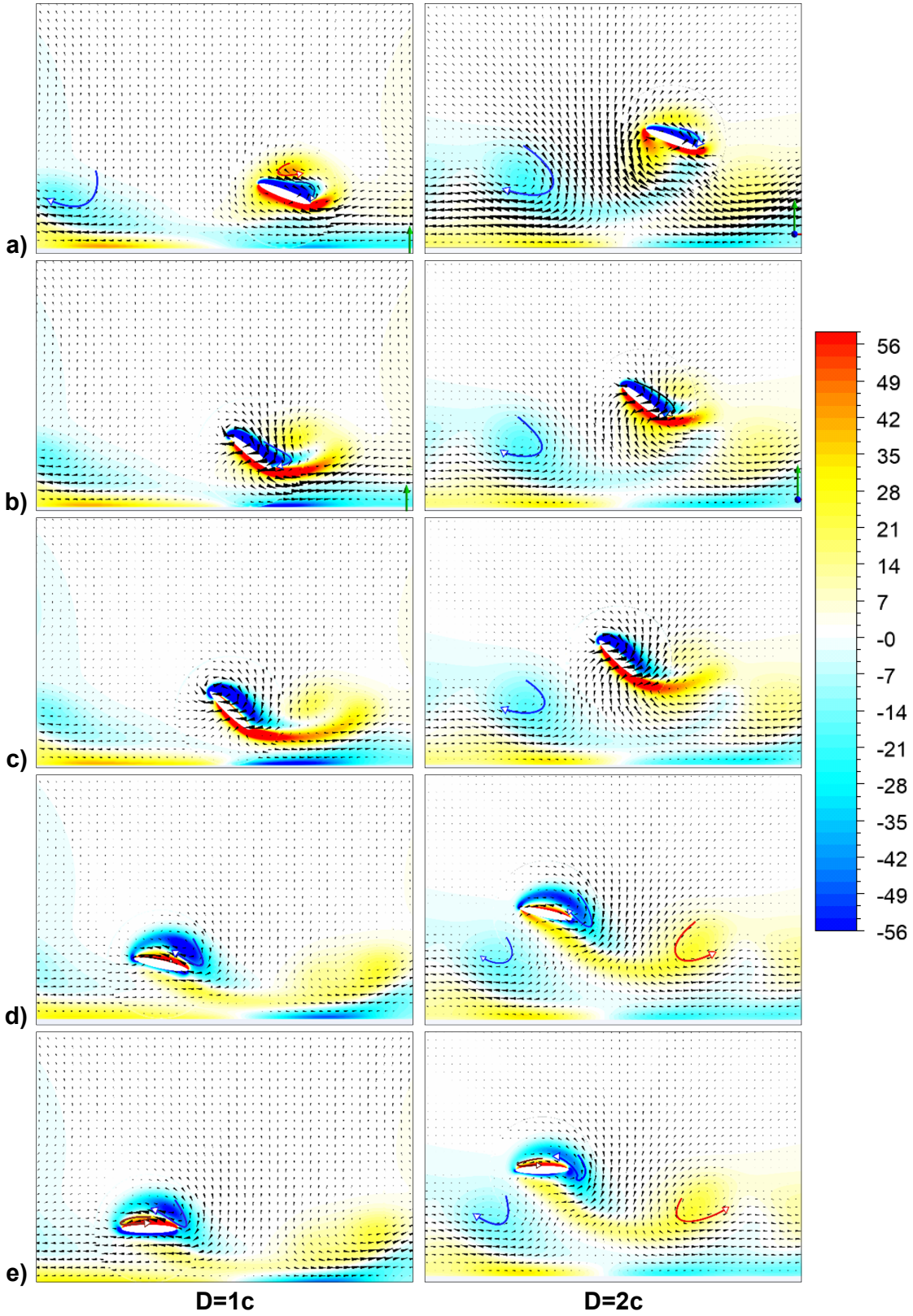

Figure 4.10 Vorticity contours at different instances of the "water treading" hovering mode for D=1c and D=2c.

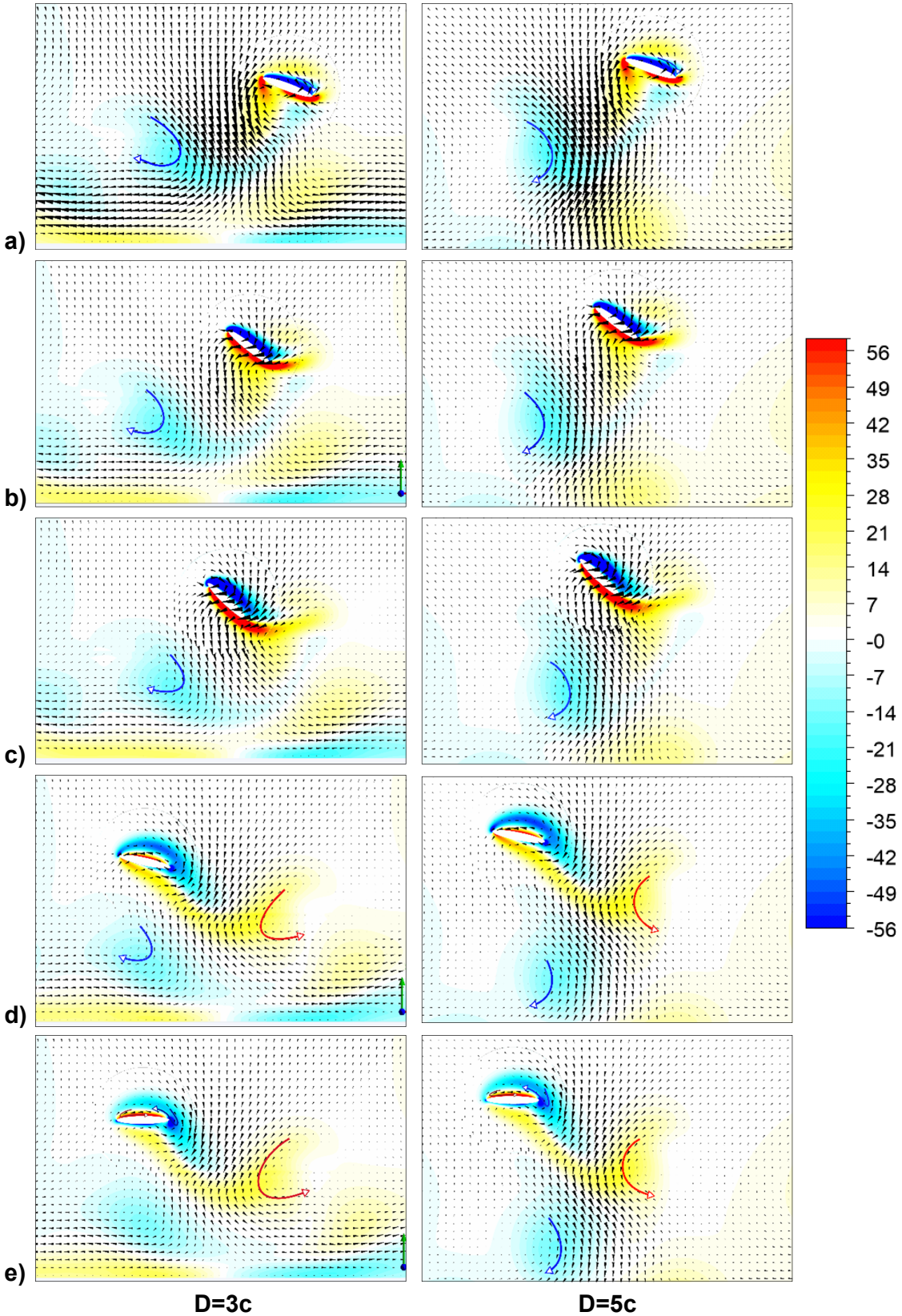

Figure 4.11 Vorticity contours at different instances of the "water treading" hovering mode for D=3c and D=5c.

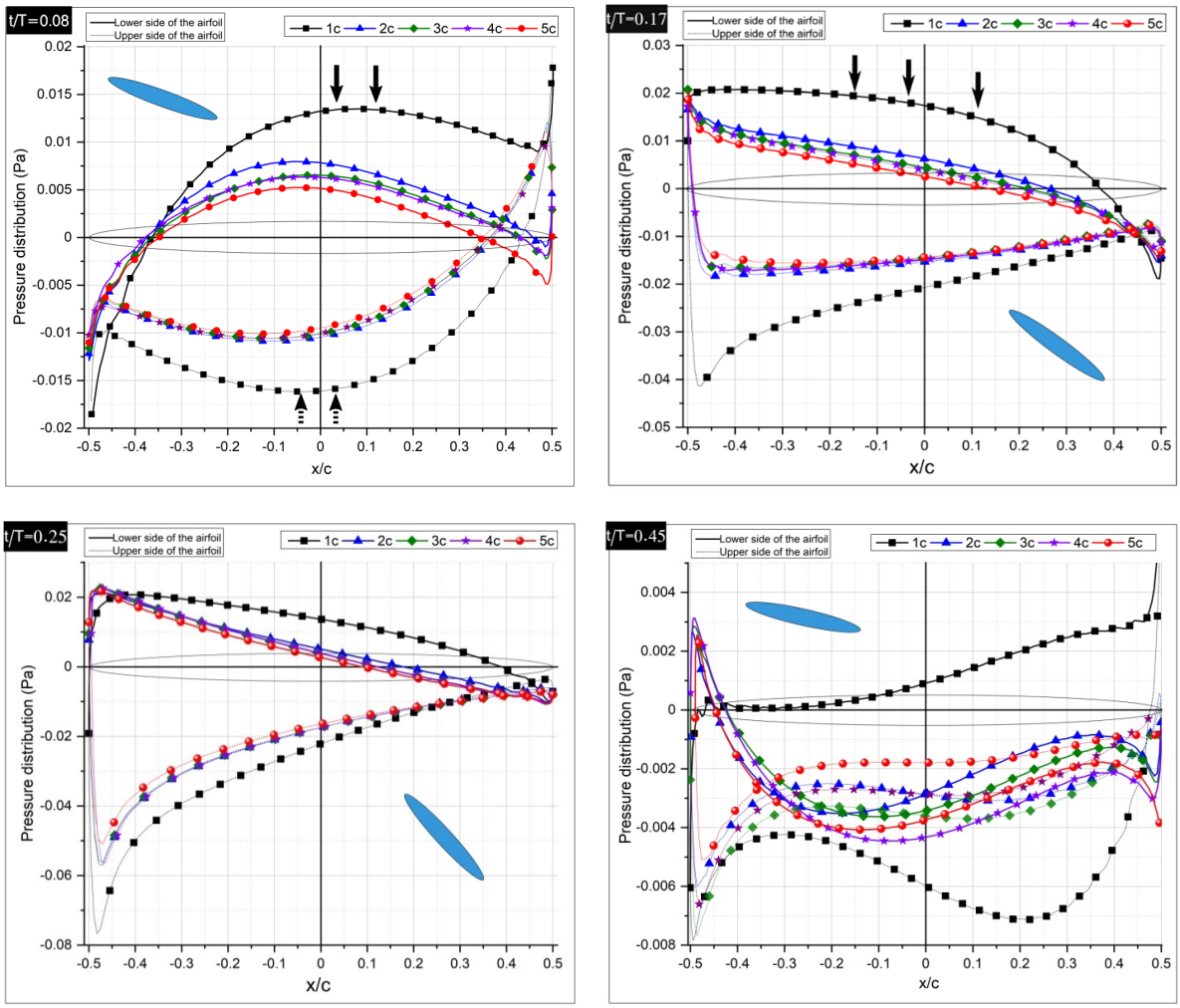

Figure 4.12 Pressure distribution on the airfoil surface for the “water treading” hovering mode.

The energy coefficient variation for several values of D is presented in Figure 4.13. The case of D=1c encounters higher energy consumption. The farther the airfoil moves away from the ground, the less energy consume. Near the reversal (at time (d)), the energy coefficient exhibits a negative value, which is due to the pressure distribution being in favor of the flapping motion. The higher-pressure distribution is saturated on the right side of the airfoil, which makes the airfoil moves forward and forced to spin in the counter clockwise direction.

Figure 4.14 represents the time averaged lift coefficient $\overline{Cl}$, the energy coefficient $\overline{Cp}$ as well as the lift efficiency η. From the averaged lift coefficient behavior, the enhancement regime is captured when D < 2c. Although the airfoil consumes high

energy nearer the ground due the cushion effect, the flight efficiency is higher in this case as well (Figure 4.14).

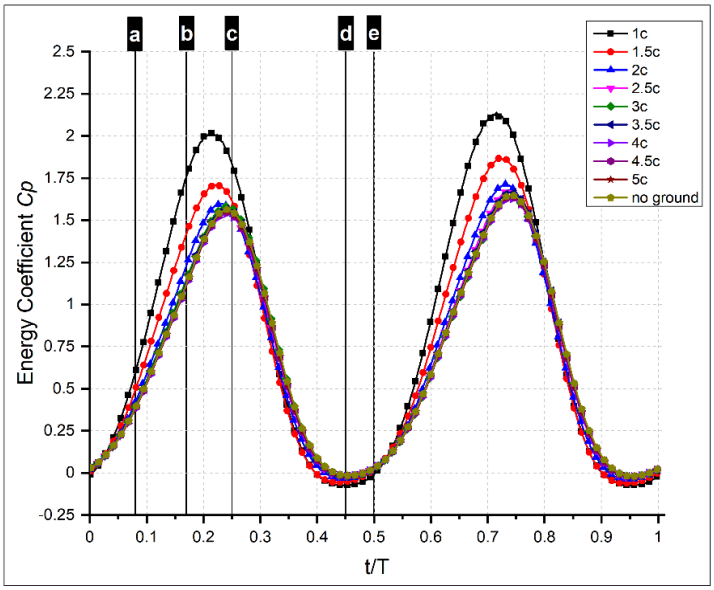

Figure 4.13 Energy coefficient of “water treading” hovering mode.

The lift efficiency had an almost identical pattern as the mean lift coefficient. This is due to the minor difference in the mean energy coefficient values for almost all ground clearance D chosen for this analysis except for the case of D=1c where the maximum energy consumption is located.

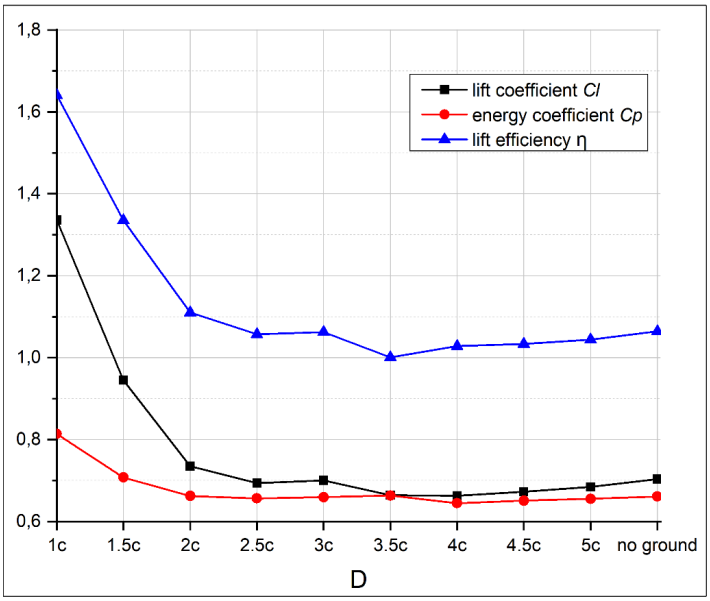

Figure 4.14 Variations of $\overline{C_l}$, $\overline{C_p}$ and η for the “water treading” hovering mode.

4.6.2 Normal hovering mode in ground effect

Unlike the previous hovering mode, the “normal” hovering mode is inspired by insects’ hovering flight. At the beginning of the stroke the airfoil is placed vertically. The airfoil accelerates from the rest while rapidly pitches down until time=0.25T when it reaches its maximal velocity. Then, the airfoil starts to pitch up while decelerating. An identical motion is repeated during the backward stroke.

The lift coefficient variation is plotted in Figure 4.15. When the ground clearance is less than 2c, only one peak at each stroke is produced. The presence of a second peak is noticed when the ground clearance increases, which indicates the presence of the wake capture mechanism as it is shown in Figure 4.15.

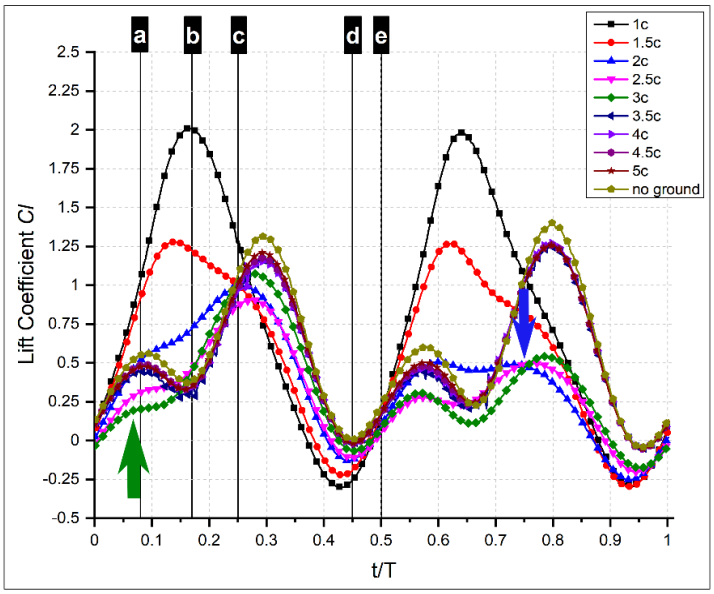

Figure 4.15 Lift coefficient of “normal” hovering mode.

The vorticity field for four different values of D (D=1c, D=2c, D=3c and D=5c) are shown in Figure 4.16 and Figure 4.17. At D=1c, a co-rotating vortices are left from the previous stroke and face the lower side of the airfoil. However, the airfoil does not interact with them as it moves forward but rather they merge with the newly formed LEV and TEV to create larger vortices as it is shown in Figure 4.16 (at time (a) and (b)). After the airfoil reaches the half of the forward stroke, the TEV separates, while a new TEV continues to form, as it can be seen in Figure 4.16 at time (c). During the backward stroke, the same flow structure and the lift coefficient pattern are repeated. However, as the ground clearance increases slightly, the initial stroke condition

persists to form the symmetry in lift pattern between the forward and the backward strokes as it can been seen in Figure 4.15 for the case of D =2c. This is due to the late separation of the LEV, which resulted in a considerably large vortex shed closer to the stroke axis. During the backward stroke, the airfoil interacts with it, which results in a significant decrease in the high-pressure zone on the lower side of the airfoil. This explains the absence of the higher second peak in the lift coefficient as the blue arrow indicates in Figure 4.15.

At the reversal, the jet created by the co-rotating LEV and TEV shed from the previous stroke impinges on the upper side of the airfoil. This explains the high-pressure distribution on the lower side of the airfoil as the black arrow indicates in Figure 4.17 at D=1c. At D=3c, from the vorticity contours at t/T=0.08, we notice the absence of the previously formed LEV on the lower side of the airfoil. Consequently, during the forward stroke only one peak is produced as the green arrow indicates in Figure 4.15. Due to trailing edge of the airfoil being closer to the ground, the shear layers that are attached to the ground are highly disturbed as it is indicated by black rectangles in Figure 4.18.

Figure 4.19 represents the energy coefficient variation for the “normal” hovering mode. Similar to what it was observed in the first hovering mode, at the reversal, a negative energy values are identified (Figure 19 (d)). The variation of the mean lift coefficient $\overline{C_l}$, the mean energy coefficient $\overline{C_p}$ and the lift efficiency η are shown in Figure 4.20. Both coefficients have a maximum value at D=1c. However, the maximum lift efficiency value is reached at D=1.5.

It can be concluded that, the averaged lift coefficient revealed three force regimes, which are:

- The force enhancement regime: for D <1.5. This regime characterised by a high lift force production caused by deflecting the flow downward, which creates sort of a cushion bellow the airfoil.
- The force reduction regime: from D=1.5 to D=3.5.This regime is characterised by significant drop in the lift generation as it can be seen in Figure 4.20. This was due to the destructive wing wake interaction.
- The force recovery regime: from D=4 to D=5.This regime is characterized by a slight increase in the lift generation can be seen (Figure 4.20).

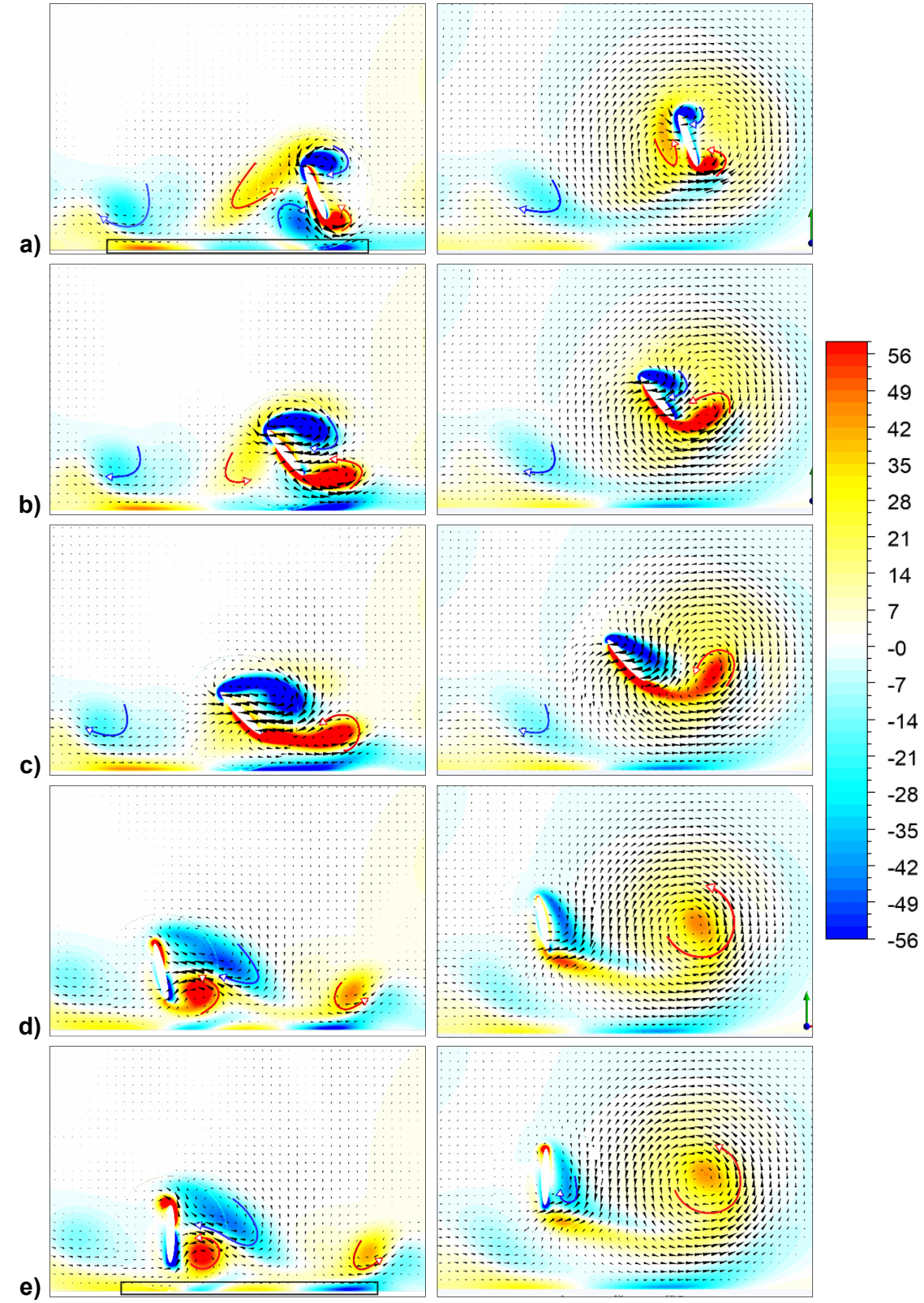

Figure 4.16 Vorticity contours of the “normal” hovering mode at D=1c and D=2c.

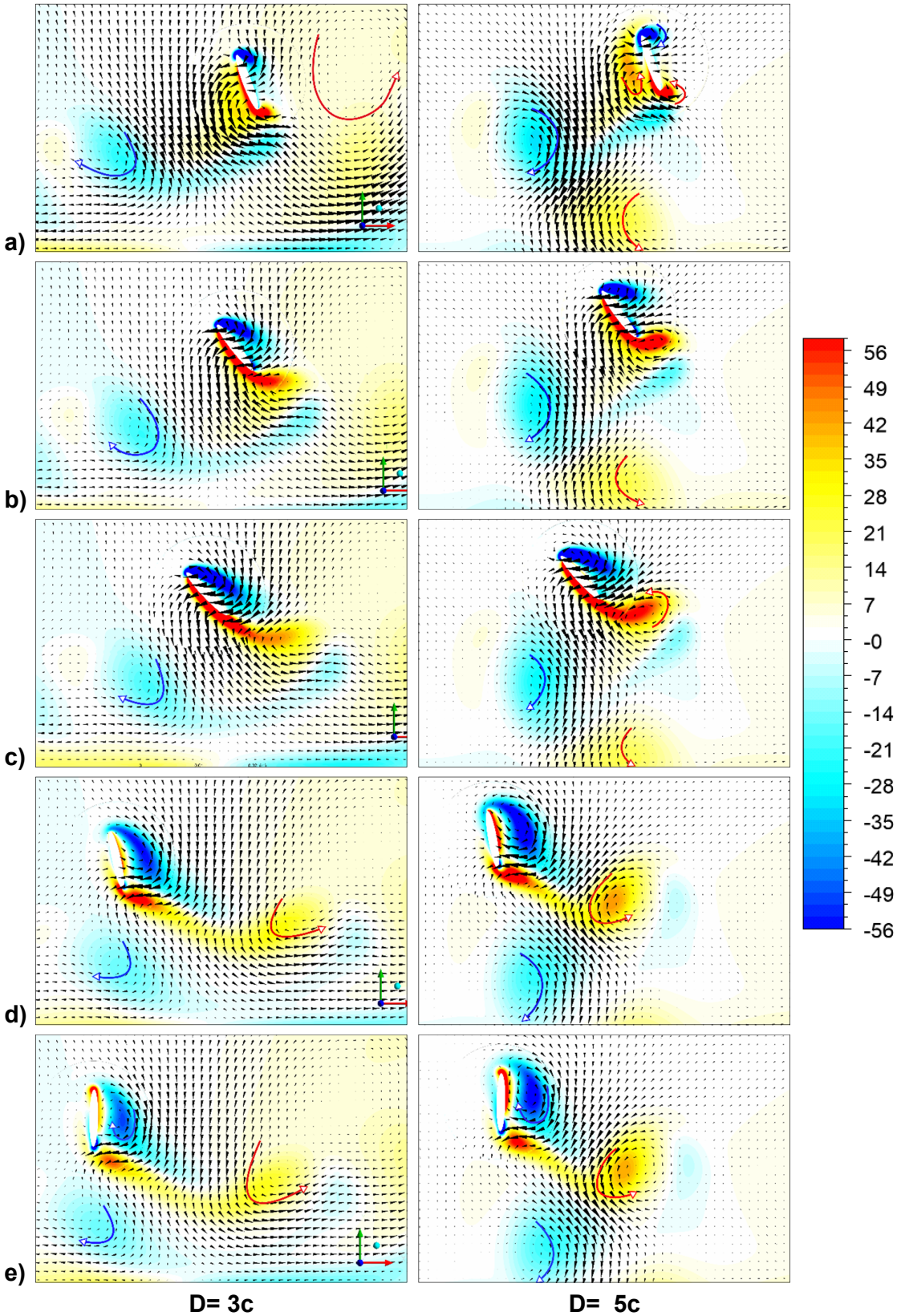

Figure 4.17 Vorticity contours of the “normal” hovering mode at D=3c and D=5c.

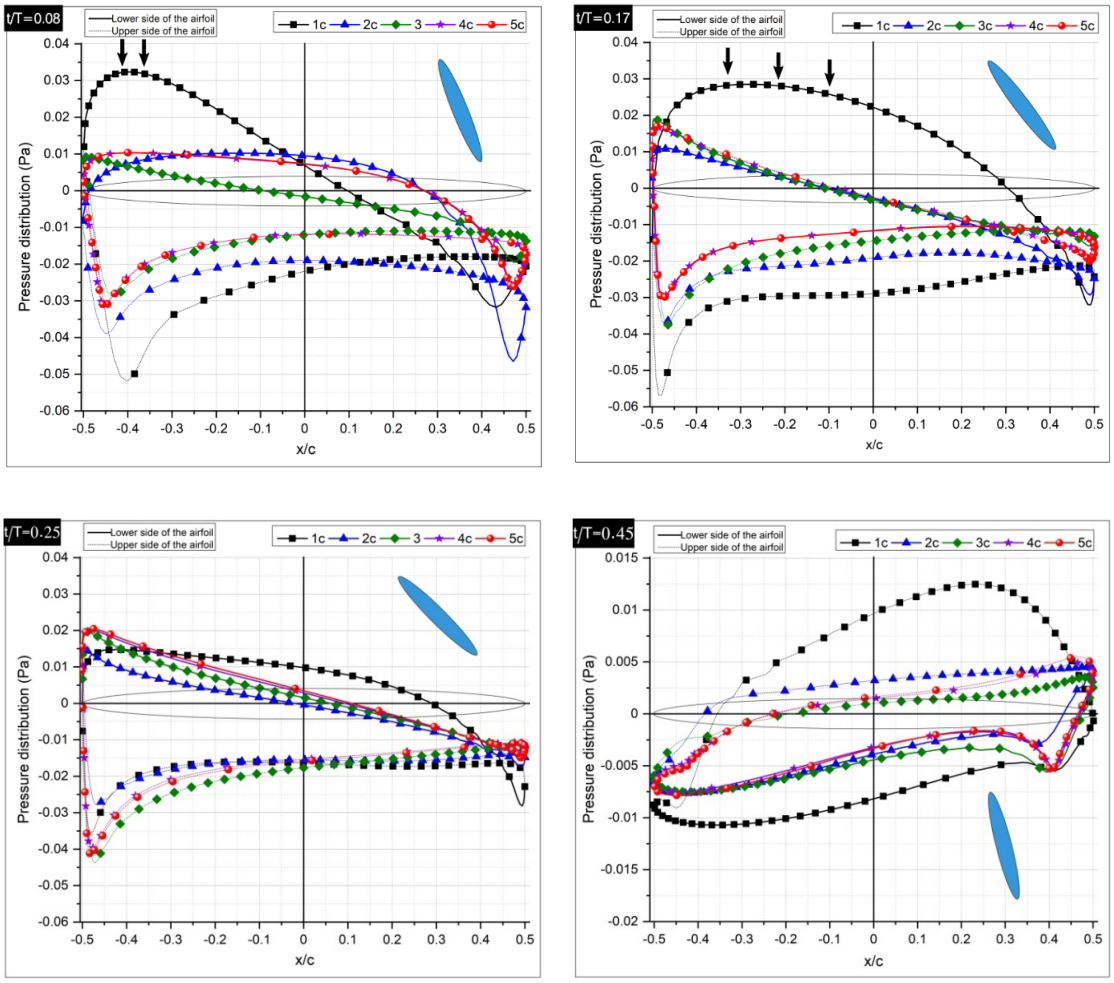

Figure 4.18 Pressure distribution on the airfoil surface for the “normal” hovering mode.

Part of the reason why the mean lift coefficient in the case of “water treading” mode was significantly higher than the “normal” mode is that at the beginning of the stroke, the shed LEV later on merges with the newly formed LEV to form even larger vortex. This leads to a significant drop in pressure when it is compared with the case of the normal mode except for D=1c. Moreover, near the reversal when the airfoil starts decelerating, the vertical force created by the jet flow impinging on airfoil when it is placed almost horizontally, is significantly higher than when it is placed almost vertically. This prevents an important loss of lift production especially at D=1c, where the minimum lift coefficient value for the water treading mode is 0.309, while for the normal mode the minimum lift coefficient reaches -0.301.

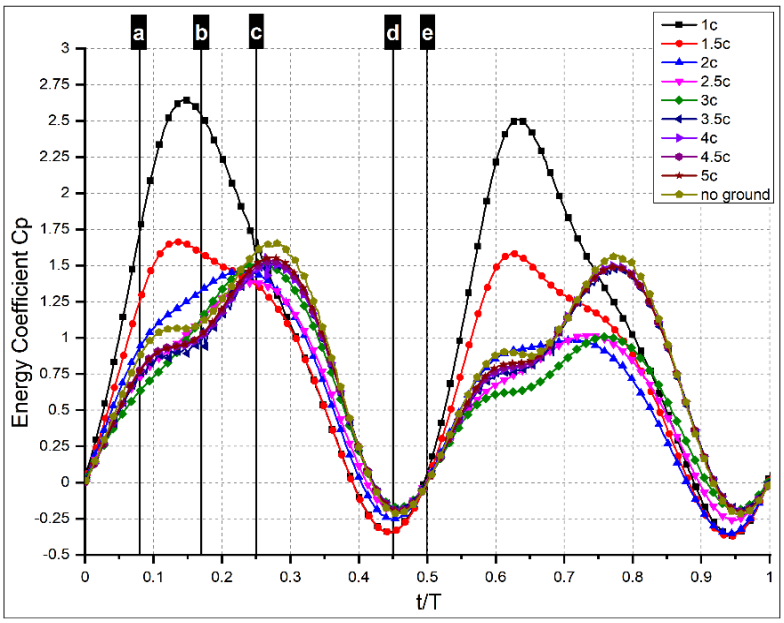

Figure 4.19 Energy coefficient of "normal" hovering mode.

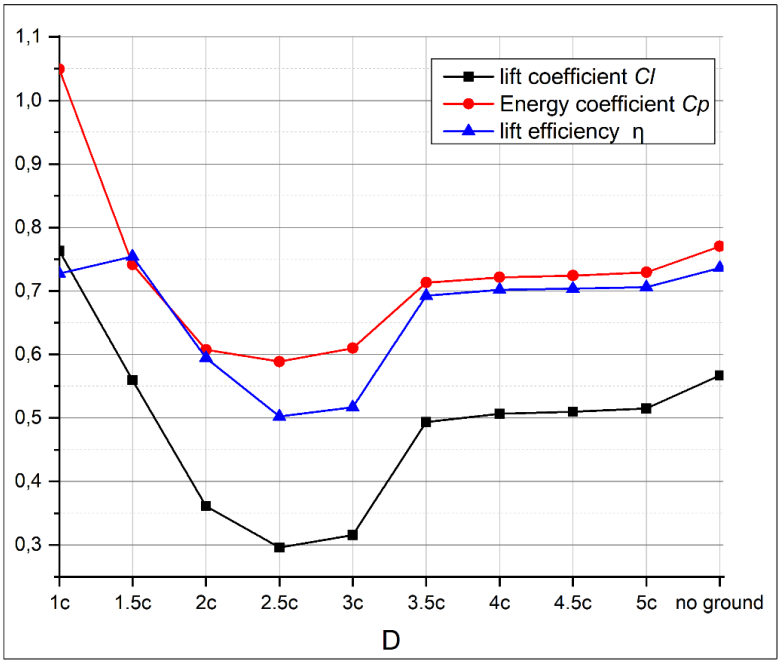

Figure 4.20 Variations of $\overline{C_l}$, $\overline{C_p}$ and η for the "normal" hovering mode.

4.7 Summarized results

To have a better understanding of the underlying physics behind the quantitative and qualitative differences observed in the lift coefficient and the energy consumption in the two hovering modes considered, the time histories of the drag and pitching moment coefficients are plotted in Figure 4.21.

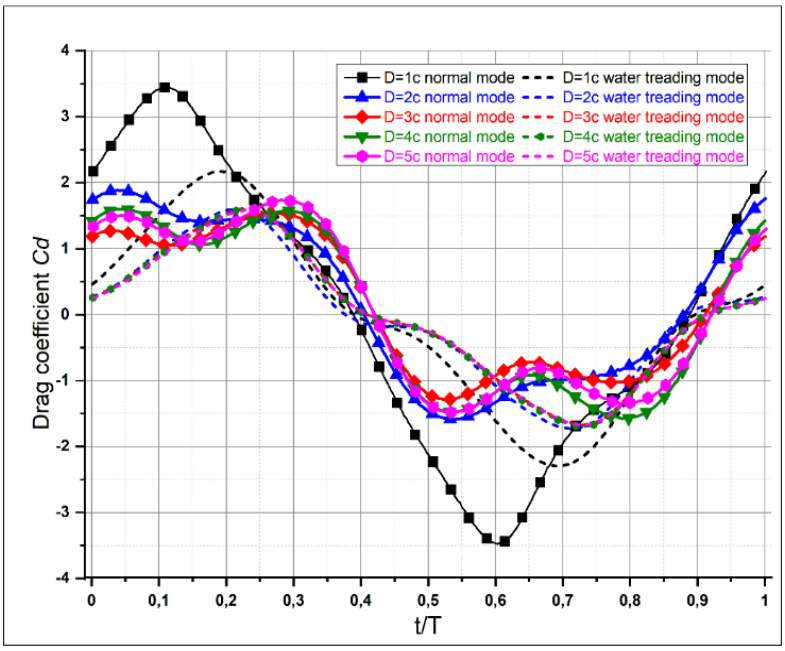

(a)

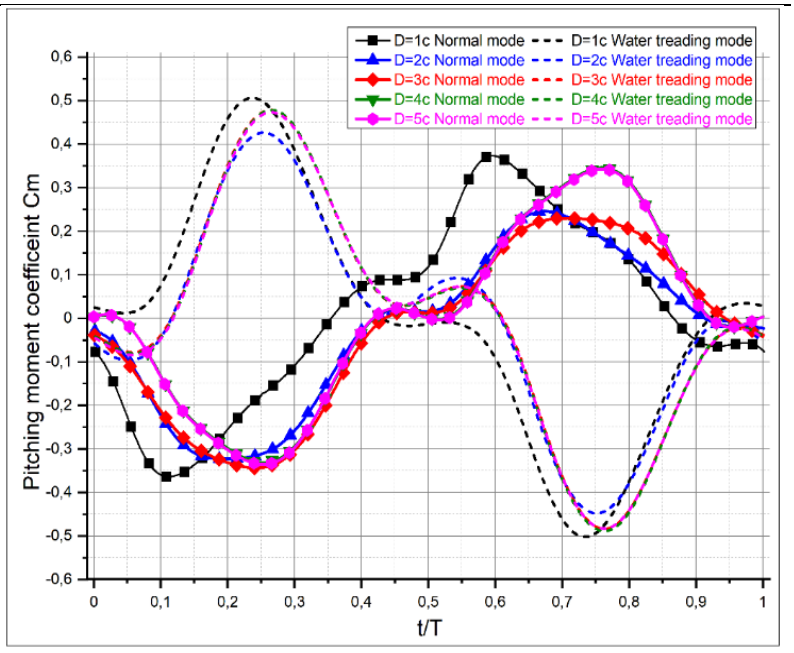

(b)

Figure 4.21 Time histories of C_d and C_m for both hovering modes, (a): Drag coefficient, (b): pitching moment coefficient.

From Figure 4.21(a), it can be seen that the drag coefficient values are higher in the case of the “normal” mode, which explains the higher energy observed in this case. However, the pitching moment values was found slightly lower in the Normal” mode as the plot of the pitching moment coefficient indicates (Figure 4.21(b)). Figure

4.22 represents the variation of mean drag coefficient $\overline{C_d}$ and the lift to drag ratio L/D for both hovering modes.

For the case of the “water treading” mode, it is seen that the lift to drag ratio increases highly as the ground clearance D decreases. Therefore, the maximum lift efficiency coefficient will most likely be located at the minimum ground clearance D. However, due to the large increase in drag coefficient as the ground clearance decreases drastically, the maximum lift efficiency coefficient was located at D=1.5.

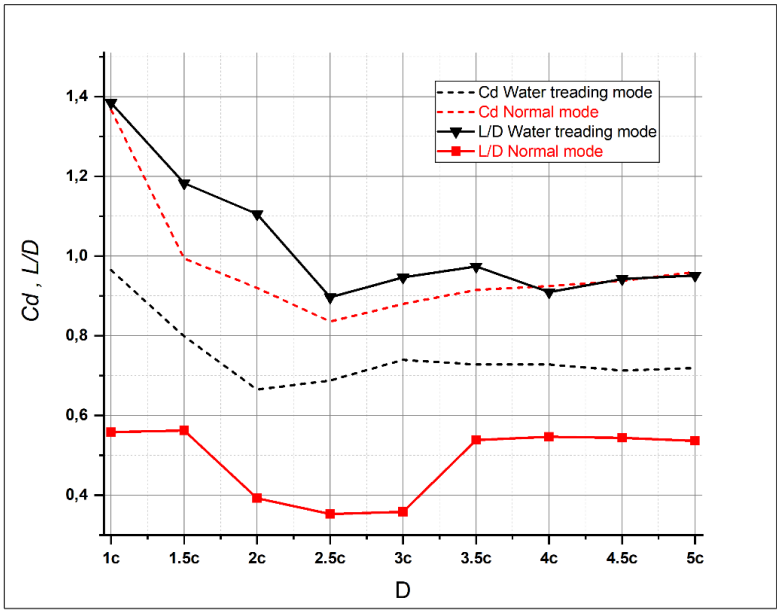

Figure 4.22 Variation of $\overline{C_d}$ and **L/D** for both hovering modes.

From Figure 4.22 and Figure 4.23, it can be seen that the lift efficiency follows the same trend of the lift to drag ratio and the energy coefficient follows the same trend as the drag coefficient, which is reasonable since higher drag coefficient implies higher energy consumption. Moreover, form Figure 4.23, it can be seen that, the energy coefficient values of all D cases are approximately the same. However, the lift efficiency is found to be much higher for the case of the “water treading” mode.

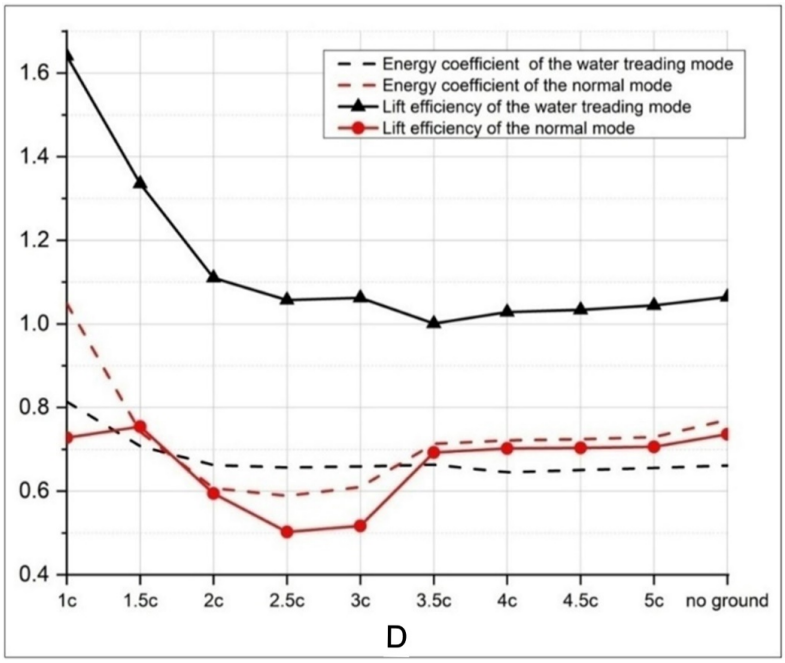

Figure 4.23 Variation of $\overline{C_p}$ and η_L for both hovering modes.

4.8 Conclusion

In this chapter, the influence of the ground on the aerodynamics of an elliptic airfoil that is subjected to translation and rotation motion has been studied. The “water treading” and “normal” hovering modes were investigated. The effects of the ground on the aerodynamics were highlighted by using several distances from the ground to the center of the airfoil.

The delayed-stall mechanism associated with the leading edge vortex and the rapid pitching mechanisms were identified in both hovering modes. However, only for the “normal” hovering mode, the wake-capturing mechanism was identified at the beginning of the stroke. The influence of the ground affected the two hovering modes differently.

When the airfoil is near the ground, the cushion effect combined with large-scale Leading edge vortex increase the lift production drastically. Although this interaction creates two lift peaks at the beginning of each stroke, as the airfoil accelerates, the direct contact of this vortex with the lower side of the airfoil decreases the lift force. This resulted in low mean lift compared with the case of the “water treading” mode.

For the “water treading” mode, the closer the airfoil gets to the ground the higher lift force is produced as well as the energy consumption and the flight efficiency. For the “normal” mode, the maximum lift production was also found when the airfoil is

situated closer to the ground. However, unlike the case of the “water treading” mode, a significant drop in the lift production in the “normal” mode, was located between D= 1.5c and D=3.5c (the force reduction regime).

CHAPTER 5: Effects of the wing spacing, phase difference and downstroke ratio on flapping tandem wing at Re=157

5.1 Introduction

In this chapter, a numerical study on the effects of flapping duration, wing spacing and phase difference on the flow around flapping tandem wing in forward flight is carried out. Three downstroke ratios to flapping period are chosen, ξ= 0.35, ξ =0.5 and ξ =0.65, where ξ=0.5 represents a symmetrical stroke. Four values of wing spacing L are chosen 1.25c, 1.5c, 1.75c and 2c (c is the wing chord length), while the phase difference was ranged from 0° to 270° with an interval of 90°. The effects of these parameters on the lift and thrust generation is investigated. The study of the energy consumption and the flight efficiency has also been taken in consideration. The Reynolds number was set at 157, which is related to a typical value of dragonfly flight regime.

5.2 Kinematic description of the flapping tandem wing

Both single and tandem wing configurations are considered in this study. An elliptical airfoil with 0.1 thickness ratio is employed, following the same wing configuration used by Li el al study [73]. The flapping motion is a combination of a translation *A(t)* and rotation α(t) applied for both single and tandem wing cases.

The mathematical description of translation and rotation motion at the different phases can be described by:

$$A(t) = A_0 + \int_0^t V(t)dt \qquad (5.1)$$

$$\alpha(t) = \alpha_0 + \int_0^t \omega(t)dt \qquad (5.2)$$

φ= 0°:

$$V(t)=\begin{cases}-\dfrac{A_m}{2\xi T}\pi\, sin\left(\dfrac{\pi t}{\xi T}\right) & 0\le t<\xi T\\ -\dfrac{A_m}{2(T-\xi T)}\pi\, sin\left(\dfrac{\pi(t-\xi T)}{(T-\xi T)}\right) & \xi T\le t<T\end{cases}$$

$$\omega(t)=\begin{cases}\alpha_m\dfrac{2\pi}{\Delta t_r}cos\left(\dfrac{2\pi t}{\Delta t_r}\right) & 0\ \le\ t\ <\ \dfrac{\Delta t_r}{4}\\ 0 & \dfrac{\Delta t_r}{4}\le\ t\ <\ \xi T-\dfrac{\Delta t_r}{4}\\ \alpha_m\dfrac{2\pi}{\Delta t_r}cos\left(\dfrac{2\pi(t-\xi T-\frac{\Delta t_r}{2})}{\Delta t_r}\right) & \xi T-\dfrac{\Delta t_r}{4}\ \le\ t\ <\ \xi T\\ \alpha_m\dfrac{2\pi}{\Delta t_r}cos\left(\dfrac{2\pi(t-\xi T+\frac{\Delta t_r}{2})}{\Delta t_r}\right) & \xi T\ \le\ t\ <\ \xi T+\dfrac{\Delta t_r}{4}\\ 0 & \xi T+\dfrac{\Delta t_r}{4}\ \le\ t\ <\ T-\dfrac{\Delta t_r}{4}\\ \alpha_m\dfrac{2\pi}{\Delta t_r}cos\left(\dfrac{2\pi(t-T)}{\Delta t_r}\right) & T-\dfrac{\Delta t_r}{4}\ \le\ t\ <\ T\end{cases}$$

φ= 90°:

$$V(t)=\begin{cases}-\dfrac{A_m}{\xi T}\ \pi\, cos\left(\dfrac{\pi t}{\xi T}\right) & 0\le t<\xi T/2\\ \dfrac{A_m}{(T-\xi T)}\ \pi\, sin\left(\dfrac{\pi(t-\frac{\xi T}{4})}{(T-\xi T)}\right) & \dfrac{\xi T}{2}\le t<T-\xi T/2\\ -\dfrac{A_m}{\xi T}\ \pi\, sin\left(\dfrac{\pi(t-\frac{\xi T}{4}-T)}{\xi T}\right) & T-\xi T/\le t<T\end{cases}$$

$$\omega(t)=\begin{cases}0 & 0 \le t < \frac{\xi T}{2}-\frac{\Delta t_r}{4}\\ \alpha_m \frac{2\pi}{\Delta t_r} sin\left(\frac{2\pi(t-\frac{\xi T}{2}-\frac{\Delta t_r}{2})}{\Delta t_r}\right) & \frac{\xi T}{2}-\frac{\Delta t_r}{4} \le t < \frac{\xi T}{2}\\ -\alpha_m \frac{2\pi}{\Delta t_r} sin\left(\frac{2\pi(t-\frac{\xi T}{2}+\frac{\Delta t_r}{2})}{\Delta t_r}\right) & \frac{\xi T}{2} \le t < \frac{\xi T}{2}+\frac{\Delta t_r}{4}\\ 0 & \frac{\xi T}{2}+\frac{\Delta t_r}{4} \le t < T-\frac{\xi T}{2}-\frac{\Delta t_r}{4}\\ -\alpha_m \frac{2\pi}{\Delta t_r} cos\left(\frac{2\pi\left(t-T+\frac{\xi T}{2}+\frac{\Delta t_r}{44}\right)}{\Delta t_r}\right) & T-\frac{\xi T}{2}-\frac{\Delta t_r}{4} \le t < T-\frac{\xi T}{2}\\ -\alpha_m \frac{2\pi}{\Delta t_r} cos\left(\frac{2\pi\left(t-T+\frac{\xi T}{2}-\frac{\Delta t_r}{4}\right)}{\Delta t_r}\right) & T-\frac{\xi T}{2} \le t < T-\frac{\xi T}{2}+\frac{\Delta t_r}{4}\\ 0 & T-\frac{\xi T}{2}+\frac{\Delta t_r}{4} \le t < T\end{cases}$$

φ= 180°

$$V(t)=\begin{cases}\frac{A_m}{(T-\xi T)}\pi\, sin\left(\frac{\pi t}{(T-\xi T)}\right) & 0 \le t < T-\xi T\\ -\frac{A_m}{\xi T}\pi\, sin\left(\frac{\pi(t-T+\xi T)}{\xi T}\right) & T-\xi T \le t < T\end{cases}$$

$$\omega(t)=\begin{cases}-\alpha_m \frac{2\pi}{\Delta t_r} cos\left(\frac{2\pi t}{\Delta t_r}\right) & 0 \le t < \frac{\Delta t_r}{4}\\ 0 & \frac{\Delta t_r}{4} \le t < T-\xi T-\frac{\Delta t_r}{4}\\ \alpha_m \frac{2\pi}{\Delta t_r} cos\left(\frac{2\pi(t-T+\xi T-\frac{\Delta t_r}{4})}{\Delta t_r}\right) & T-\xi T-\frac{\Delta t_r}{4} \le t < T-\xi T\\ \alpha_m \frac{2\pi}{\Delta t_r} cos\left(\frac{2\pi(t+\xi T+\frac{\Delta t_r}{4})}{\Delta t_r}\right) & T-\xi T \le t < T-\xi T+\frac{\Delta t_r}{4}\\ 0 & T-\xi T+\frac{\Delta t_r}{4} \le t < T-\frac{\Delta t_r}{4}\\ -\alpha_m \frac{2\pi}{\Delta t_r} cos\left(\frac{2\pi(t-T)}{\Delta t_r}\right) & T-\frac{\Delta t_r}{4} \le t < T\end{cases}$$

φ= 270°

$$V(t)=\begin{cases}\dfrac{A_m}{(T-\xi T)}\,\pi\cos\left(\dfrac{\pi t}{(T-\xi T)}\right) & 0 \le t < \dfrac{T}{2}-\xi T/2\\ -\dfrac{A_m}{\xi T}\,\pi\sin\left(\dfrac{\pi(t-\frac{T}{2}+\frac{\xi T}{4})}{\xi T}\right) & \dfrac{T}{2}-\dfrac{\xi T}{2} \le t < \dfrac{T}{2}+\xi T/2\\ \dfrac{A_m}{(T-\xi T)}\,\pi\sin\left(\dfrac{\pi(t-\frac{T}{2}-\frac{\xi T}{4})}{(T-\xi T)}\right) & \dfrac{T}{2}+\xi T/2 \le t < T\end{cases}$$

$$\omega(t)=\begin{cases}0 & 0 \le t < \dfrac{T}{2}-\dfrac{\xi T}{2}-\dfrac{\Delta t_r}{4}\\ \alpha_m\dfrac{2\pi}{\Delta t_r}\cos\left(\dfrac{2\pi(t-\frac{T}{2}+\frac{\xi T}{2}-\frac{\Delta t_r}{2})}{\Delta t_r}\right) & \dfrac{T}{2}-\dfrac{\xi T}{2}-\dfrac{\Delta t_r}{4} \le t < \dfrac{T}{2}-\dfrac{\xi T}{2}\\ \alpha_m\dfrac{2\pi}{\Delta t_r}\cos\left(\dfrac{2\pi(t-\frac{T}{2}+\frac{\xi T}{2}+\frac{\Delta t_r}{2})}{\Delta t_r}\right) & \dfrac{T}{2}-\dfrac{\xi T}{2} \le t < \dfrac{T}{2}-\dfrac{\xi T}{2}+\dfrac{\Delta t_r}{4}\\ 0 & \dfrac{T}{2}-\dfrac{\xi T}{2}+\dfrac{\Delta t_r}{4} \le t < \dfrac{T}{2}+\dfrac{\xi T}{2}-\dfrac{\Delta t_r}{4}\\ \alpha_m\dfrac{2\pi}{\Delta t_r}\cos\left(\dfrac{2\pi(t-\frac{T}{2}-\frac{\xi T}{2}-\frac{\Delta t_r}{2})}{\Delta t_r}\right) & \dfrac{T}{2}+\dfrac{\xi T}{2}-\dfrac{\Delta t_r}{4} \le t < \dfrac{T}{2}+\dfrac{\xi T}{2}\\ \alpha_m\dfrac{2\pi}{\Delta t_r}\cos\left(\dfrac{2\pi(t-\frac{T}{2}-\frac{\xi T}{2}+\frac{\Delta t_r}{2})}{\Delta t_r}\right) & \dfrac{T}{2}+\dfrac{\xi T}{2} \le t < \dfrac{T}{2}+\dfrac{\xi T}{2}+\dfrac{\Delta t_r}{4}\\ 0 & \dfrac{T}{2}+\dfrac{\xi T}{2}+\dfrac{\Delta t_r}{4} \le t < T\end{cases}$$

where A_m is the amplitude of translation, α_m the amplitude of rotation, Δt_r is the time duration to perform a rotation which is chosen to be 0.2T, T is the stroke period, ξ is the downstroke duration ratio which can be described by $\xi = t_{down}/T$.

The schematic of the tandem wing motion is shown in Figure 5.1.

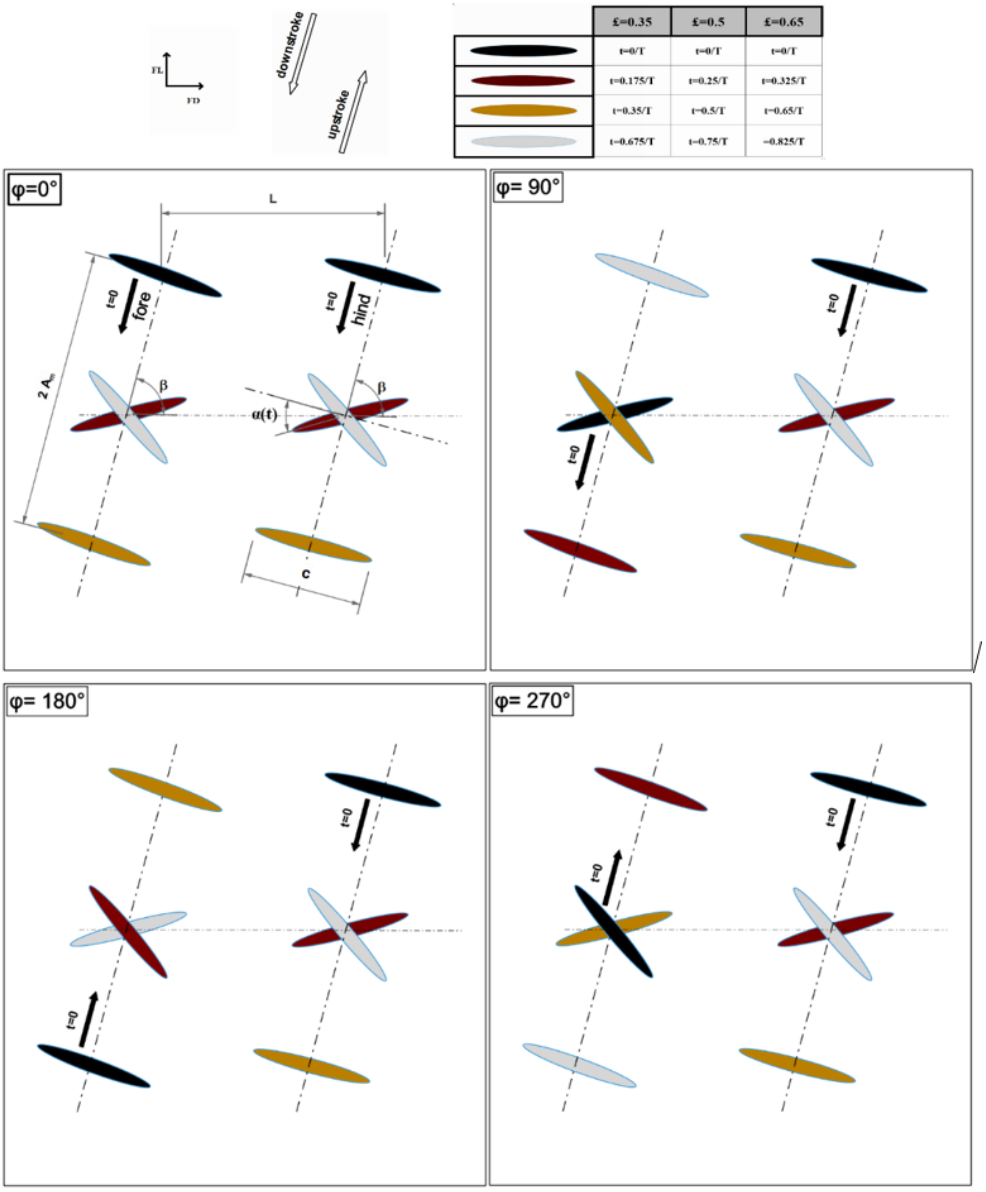

Figure 5.1 Schematic of the tandem wing motion.

For the case of ξ=0.35, the time histories of the translation displacement as well as rotation angle for different phases are plotted in Figure 5.2.

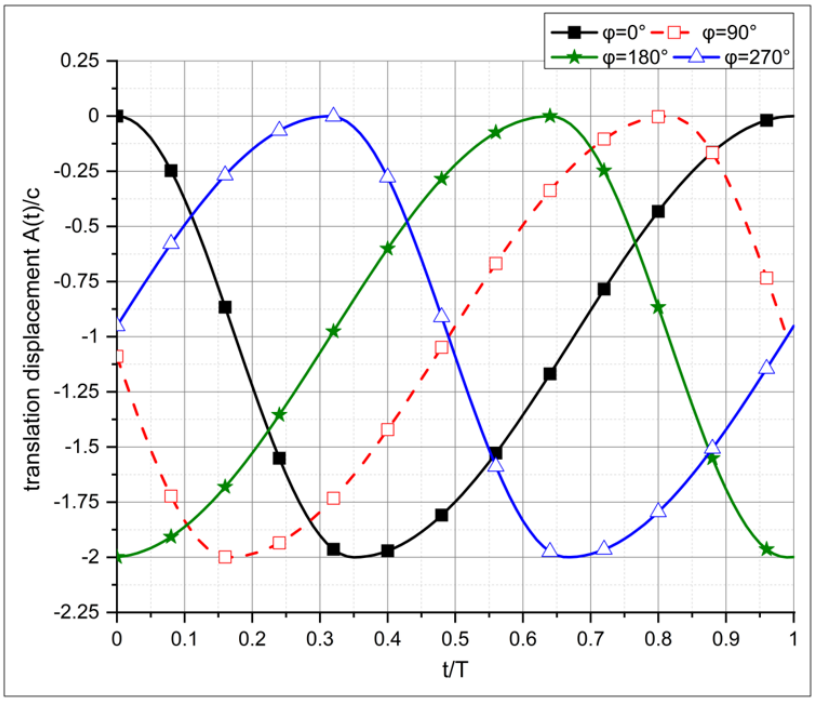

a)

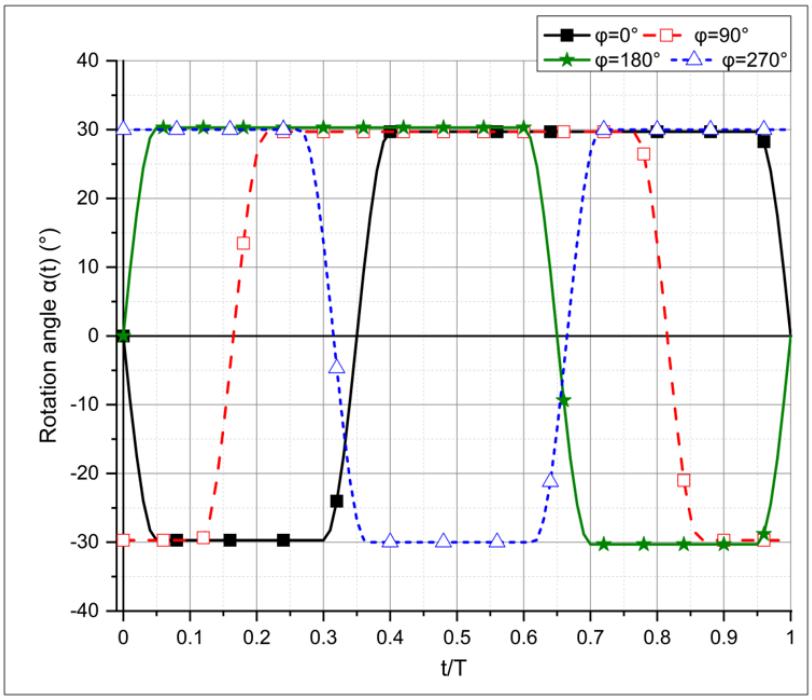

b)

Figure 5.2 Time histories of the flapping motion used in this study at ξ=0.35. *a)* Translation displacement A(t), *b)* angular rotation, α(t)

5.3 Boundary conditions and mesh generation

The computation domain dimensions are 25c by 20c as it is shown in Figure 5.3. The wall surface of the wings was set as no slip. The inlet boundary was set to the left side of the domain while the right, top and bottom of the domain was set as pressure outlet. The wing motion was achieved using a user defined function (UDF). The macro function DEFINE_CG_MOTION was used for both the translation and rotation of the tandem wings. The computational domain was divided into two zones, the dynamic zone were the re-meshing occurs and the stationary zone which covers the rest of the domain outside the dynamic zone. For the dynamic zone, a triangular mesh was used while the stationary zone a structured quadrilateral mesh was used as shown in Figure 5.4.

A pressure based Navier stokes solver was applied. The pressure velocity coupling is achieved by using coupled scheme. The momentum equation is discretized using a second order upwind scheme. With CFL (Courant-Friedrichs-Lewy number) less than one, the time step is guaranteed to be capable to capture all the flow fluctuations [86].

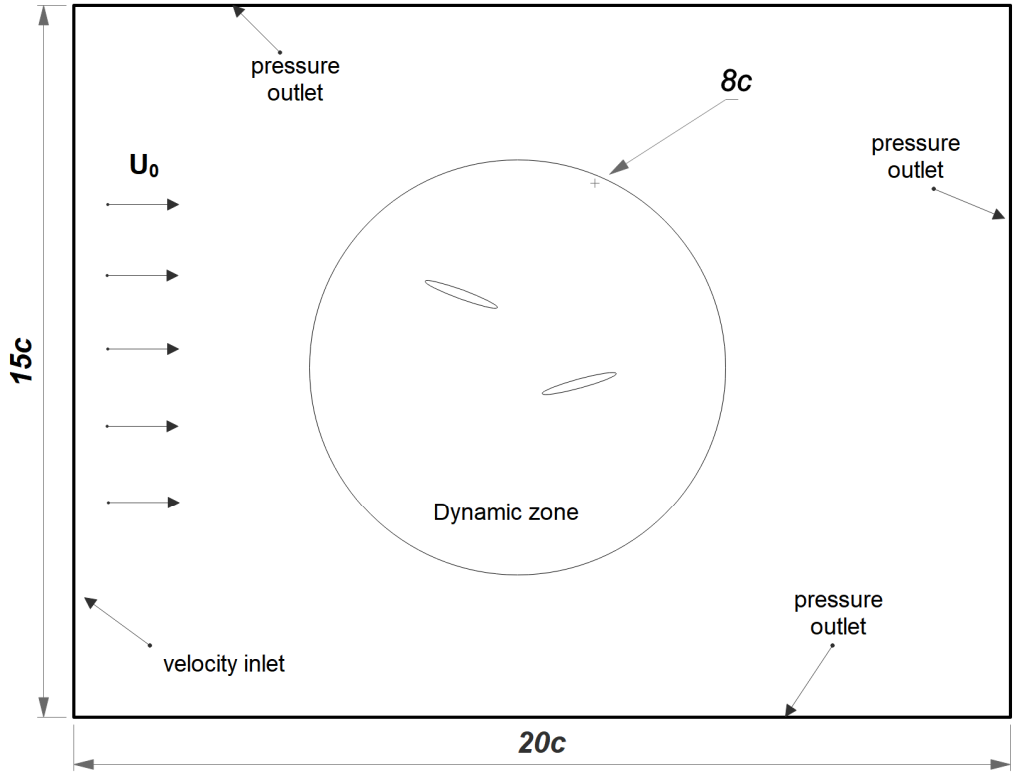

Figure 5.3 Computational domain and boundary conditions

5.4 Grid independency

Grid independence study is conducted first to determine the appropriate mesh size. The spatial accuracy of the present algorithm is examined by employing three grid size levels. Details regarding the number of elements and nodes as well as average lift coefficient obtained and the computational cost in each analysis are listed in Table 5.1. A medium grid distribution with 99973 cells was refined and coarsened with ratio of 2 (Table 5.1).

Figure 5.4, Figure 5.5 and Figure 5.6 represent the different grids used in the grid independency study.

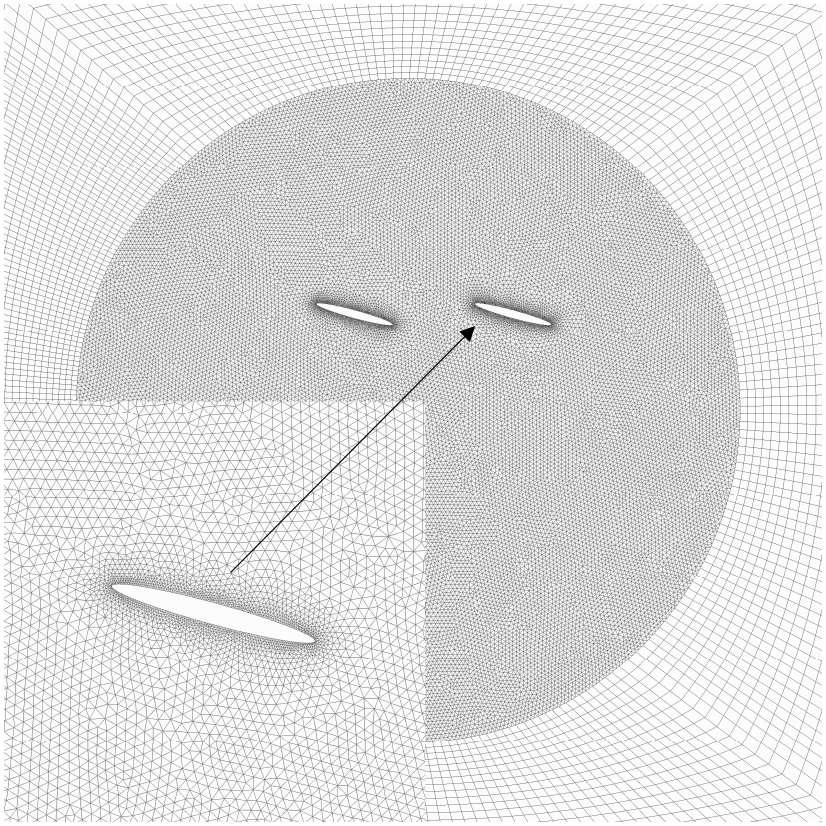

Figure 5.4 Coarse mesh

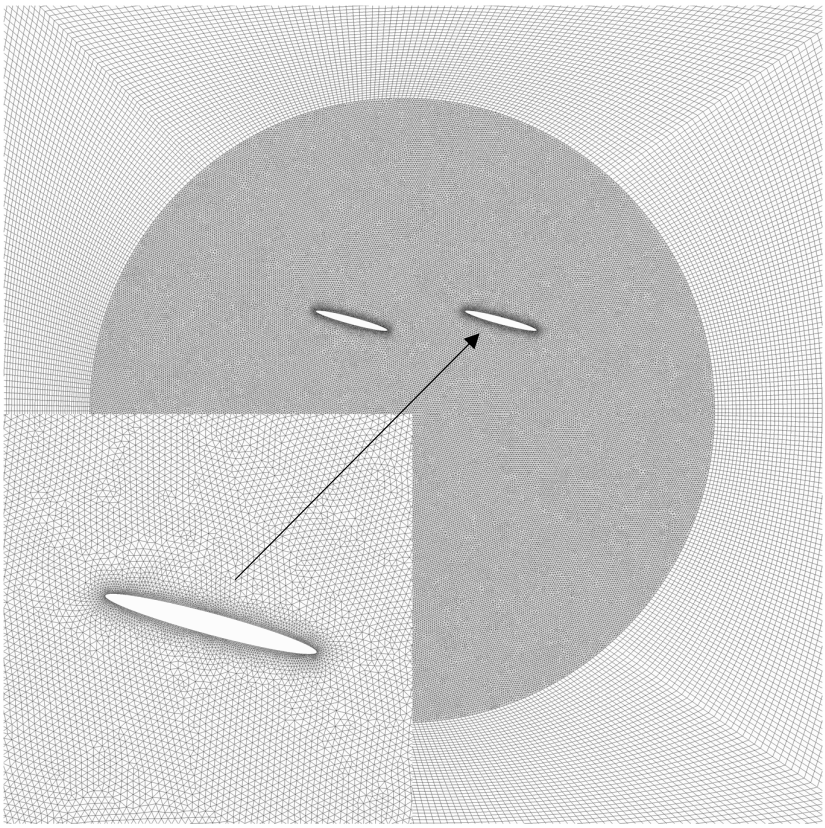

Figure 5.5 Intermediate mesh

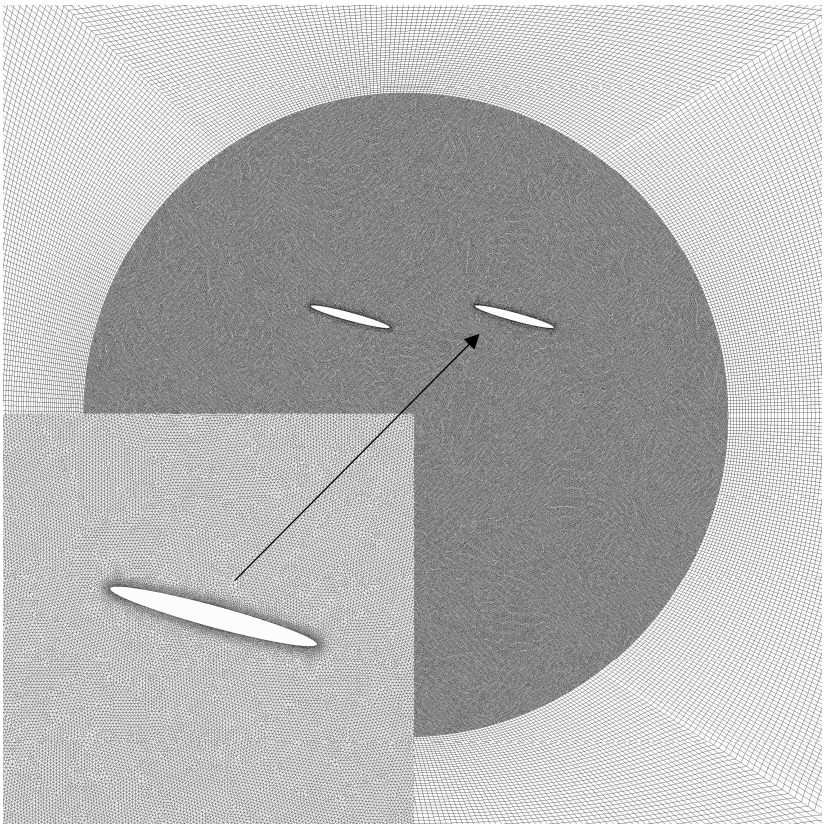

Figure 5.6 Fine mesh

Table 5.1 Grid independence study results for tandem wing configuration. Re=157, L=2c, $\xi = 0.5\ and\ \varphi = 0°$

Grid	Number of elements	Average Lift Coefficient $\overline{C_l}$	Difference of $\overline{C_l}$ compared with the ultra fine mesh %	Number of periods	Number of logical processors (I7 HQ 4700)	Computational time (hrs)
Coarse	53609	0,526	12.4%	12	4	6
Intermediate	99973	0.480	2.69	10	2	10
Fine	217932	0,467		9	5	14

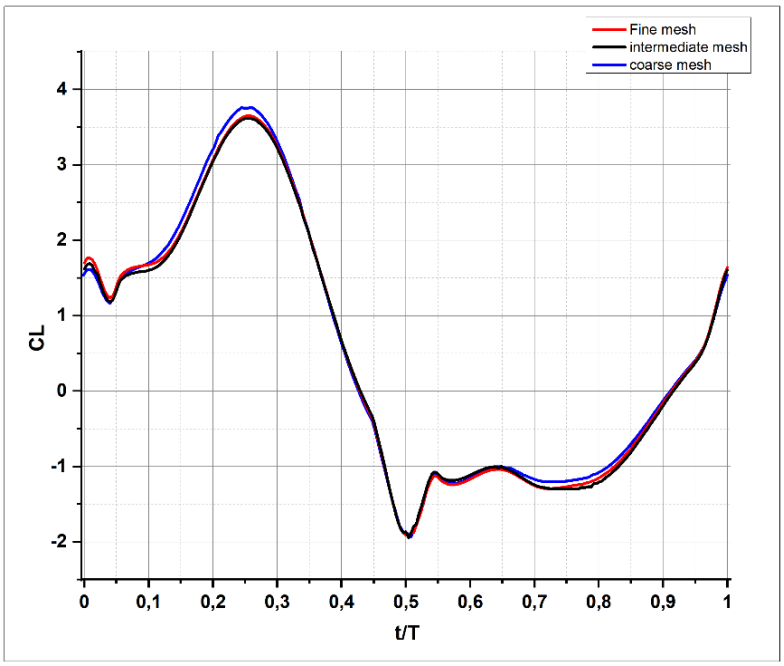

Figure 5.7 Lift coefficient for three different grid sizes for the hindwing with L=2c and ξ=0.5.

As observed in Figure. 5.7 and Table 4.1, the intermediate grid gives satisfactory balance between numerical accuracy and computational cost. The results also indicate that reasonable grid independence was obtained, taking into account the unsteadiness of the flapping flight.

5.5 Validation study

The present case was first validated through a comparison with a typical work studied by many researchers, wang [93], Xu and Wang [92] and Gao and Lu [56]. The kinematic parameters used were: $\xi = 0.5$, K=0.4, $A_m = 1.25c$, $\alpha_m = 45°$ $\alpha_0 = -30°$ $\beta = 60°$ and Re=157. The present results showed a good agreement with the results obtained in the studies mentioned above, as it is shown in Figure 5.8.

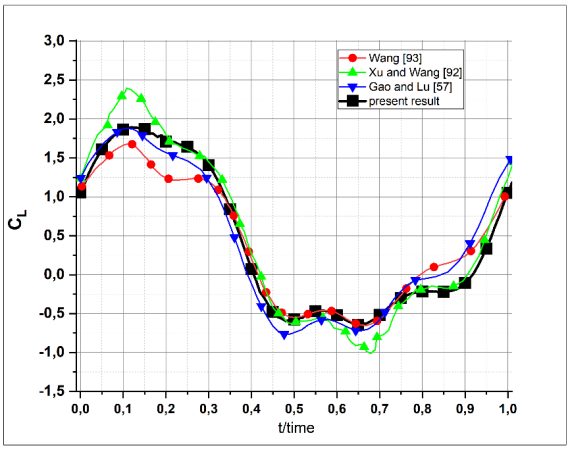

Lift Coefficient

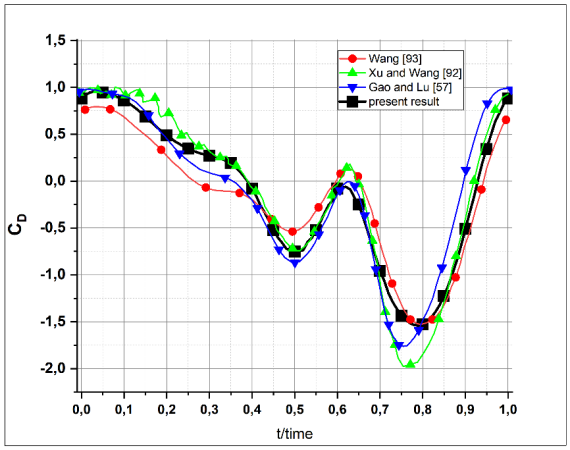

Drag coefficient

Figure 5.8 Comparison of the time histories of the lift coefficient and drag coefficient of the present study and the results obtained from the literature.

5.6 Results and discussion

The Reynolds number was fixed at 157, which suits the dragon fly flight range [94]. We followed the same kinematic parameters used by Zhu et al. [75], where the stroke amplitude is 1.25c, the stroke angle β is 75°, the initial stroke angle $\alpha_0 is$ 15°, and

the reduced frequency K is 0.4. The results obtained in this work were taken from 8th period where the flow is guaranteed to reach a periodic state.

At the beginning of the analyses, a detailed investigation of the effects of the downstroke ratio on an isolated wing was proposed. The results obtained are used for comparison with the results obtained in the case of the tandem wing analysis.

5.6.1 Effects of the downstroke ratio on a single wing:

The transient thrust, lift and energy consumption coefficient histories are displayed in Figure 5.9.

The first thing to notice is that the asymmetry in stroke duration leads to a remarkable difference in the thrust and lift generation. From Figure 5.9 (a), we notice that the thrust force is generated during the downstroke at ξ =0.35 and during the upstroke at ξ =0.65. However, at ξ =0.5 the thrust force is generated during both the downstroke and the upstroke.

The lift is generated mainly during the downstroke for all ξ cases as it is shown in Figure 5.9 (b).

From the energy coefficient plot (Figure 5.9 -c), it is seen that the energy coefficient peaks are achieved during the faster stroke (the downstroke at ξ=0.35 and the upstroke at ξ=0.65). However, at ξ =0.5 the energy consumption peak is achieved during the downstroke which was used to generate the most of the lift force.

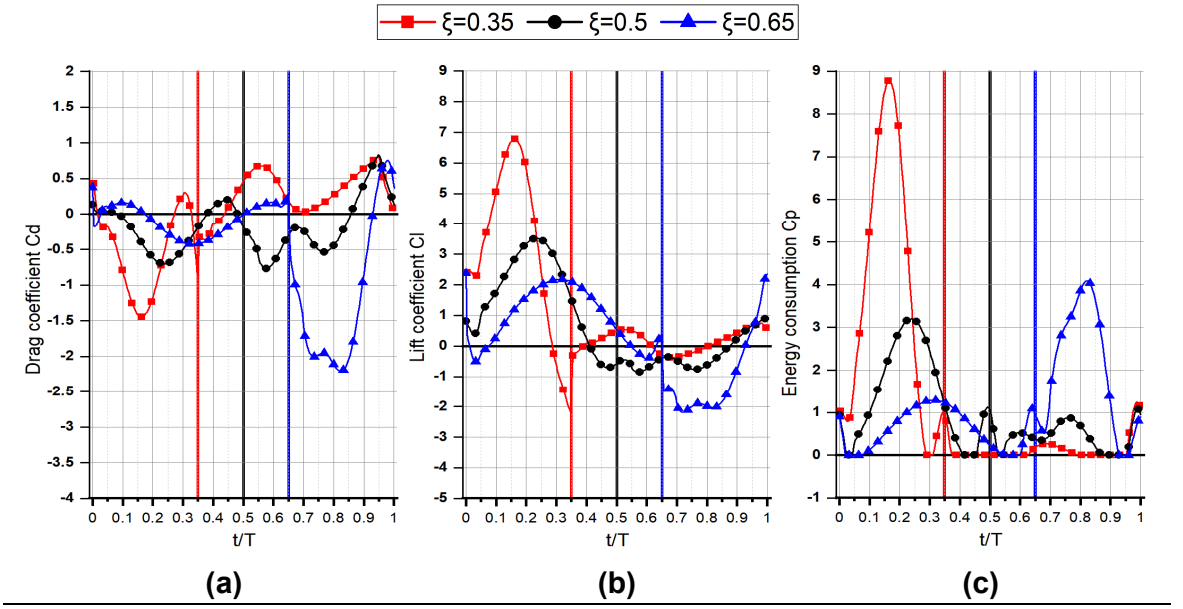

Figure 5.9 Time histories of C_d, $C_l$and C_p: a) drag coefficient, b) lift coefficient, c) energy consumption coefficient for an isolated single wing at 3 downstroke ratios

5.6.2 Effects of wing spacing on flapping tandem wing configuration

Figure 5.10 and Figure 5.11 summarize respectively the cycle-averaged of the thrust and the lift coefficients for the fore and hind wings compared with a single wing. Both the fore and hind wings had higher averaged thrust coefficient than that of a single wing for all wing spacing and downstroke ratio values (see Figure 5.10). Consequently, the combined results of the fore and hind wings produce more thrust forces than that of a single wing.

From Figure 5.11, it is noticed that the forewing has higher lift coefficient than the hindwing for all wing spacing L for the cases of ξ =0.35 and ξ =0.5. However, at ξ =0.65, the hindwing has higher lift coefficient as L increases

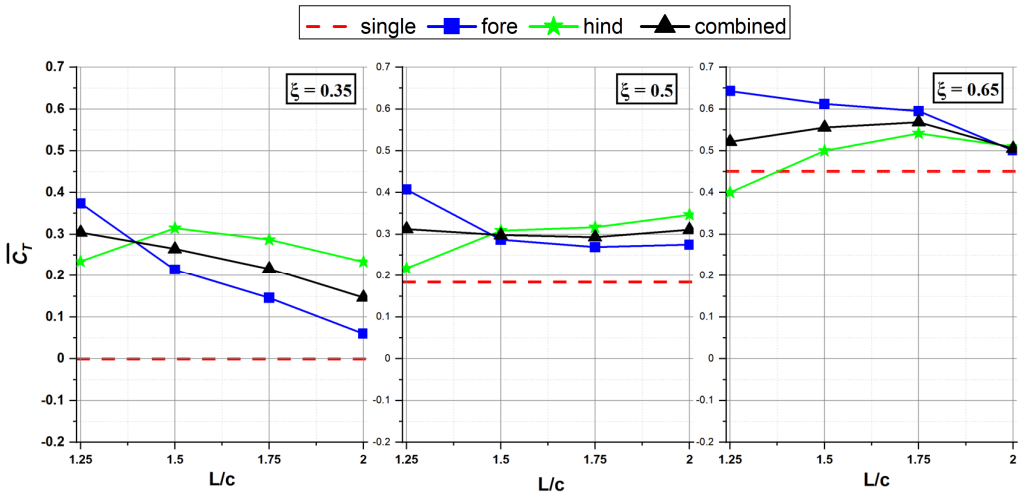

Figure 5.10 Variation of the mean thrust coefficient at different wing spacings and downnstroke rations at φ=0°

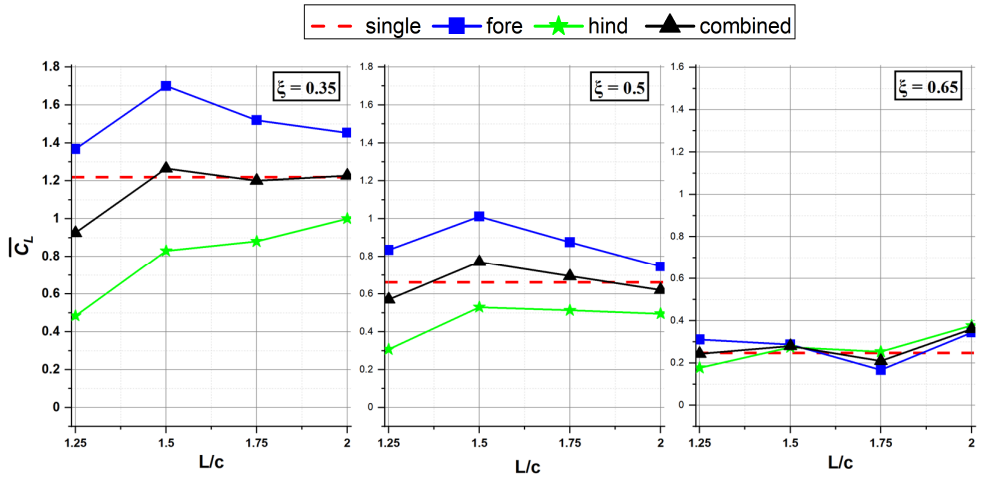

Figure 5.11 Variation of the mean lift coefficient at different wing spacings and downnstroke rations at φ=0°

As the wing spacing L increases, the effects of the hindwing on the flow structure around the forewing decrease as it is shown in Figure 5.12.

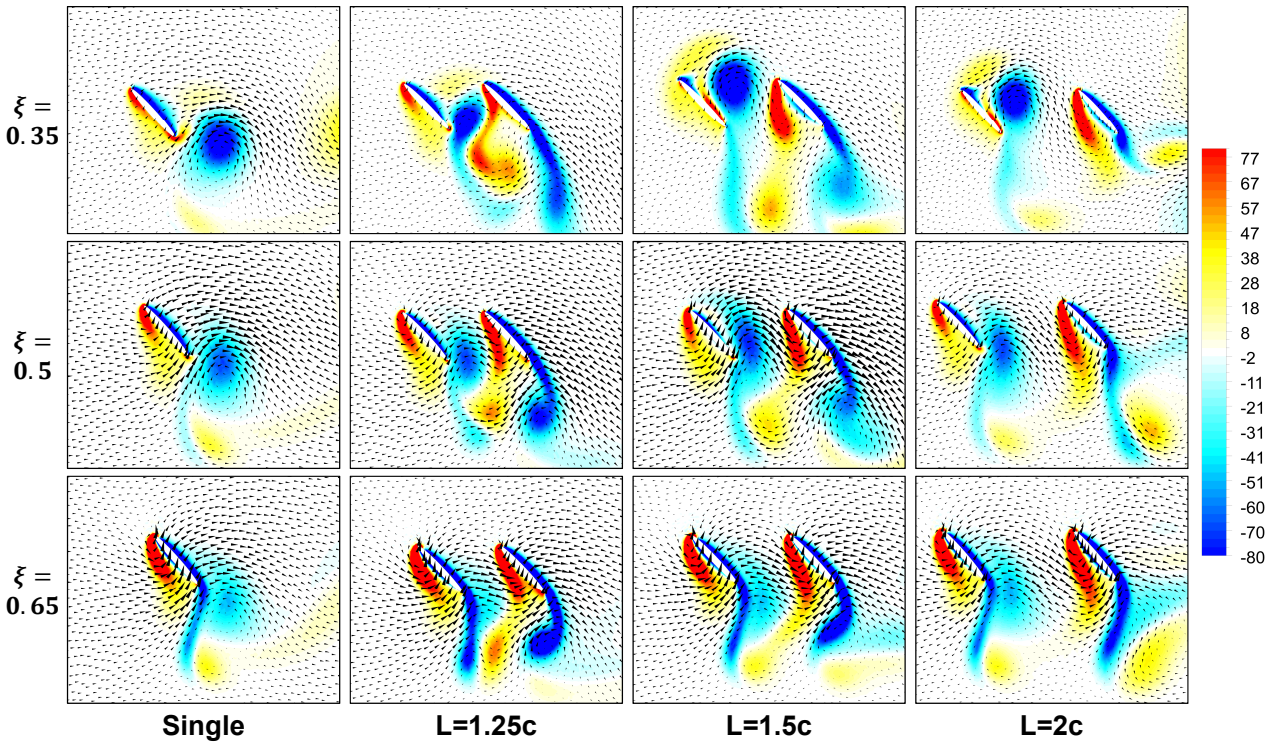

Figure 5.12 vorticity contours around a single and tandem wing configurations with 0° of phase difference at L=1.25, L=1.5 and L=2c at time 0.75T

5.6.3 Effects of wing spacing, phase difference and downstroke ratio on the lift generation

Figure 5.13 compares the time histories of the lift coefficient of the hindwing at different values of the wing spacings L, phase differences φ and downstroke ratios ξ. The lift generation was located during the downstroke for all cases. The positive lift peaks were significantly higher at ξ=0.35, which is due to the rapid acceleration effects as suggested by Sun and Tang [51].

In the case of ξ=0.35 and ξ=0.65, the lift pattern remained almost unchanged as the wing spacing increases. However, in the case of ξ=0.5, it is seen that the lift pattern at φ=180° changes as the wing spacing increases. Where we notice the disappearance of the lift peak during the downstroke at L=1.75c and L=2c. This is due to the destructive interaction between the TEV left from the forewing during its upstroke and the LEV formed on the hindwing as it can be seen in Figure 5.14. This interaction dampens out the leading edge vortex, which leads to a weak lift production.

The lift coefficient plots suggest that in-phase flapping as well as with a phase of 270° at ξ=0.35 enhance the lift generation of the tandem wing configuration.

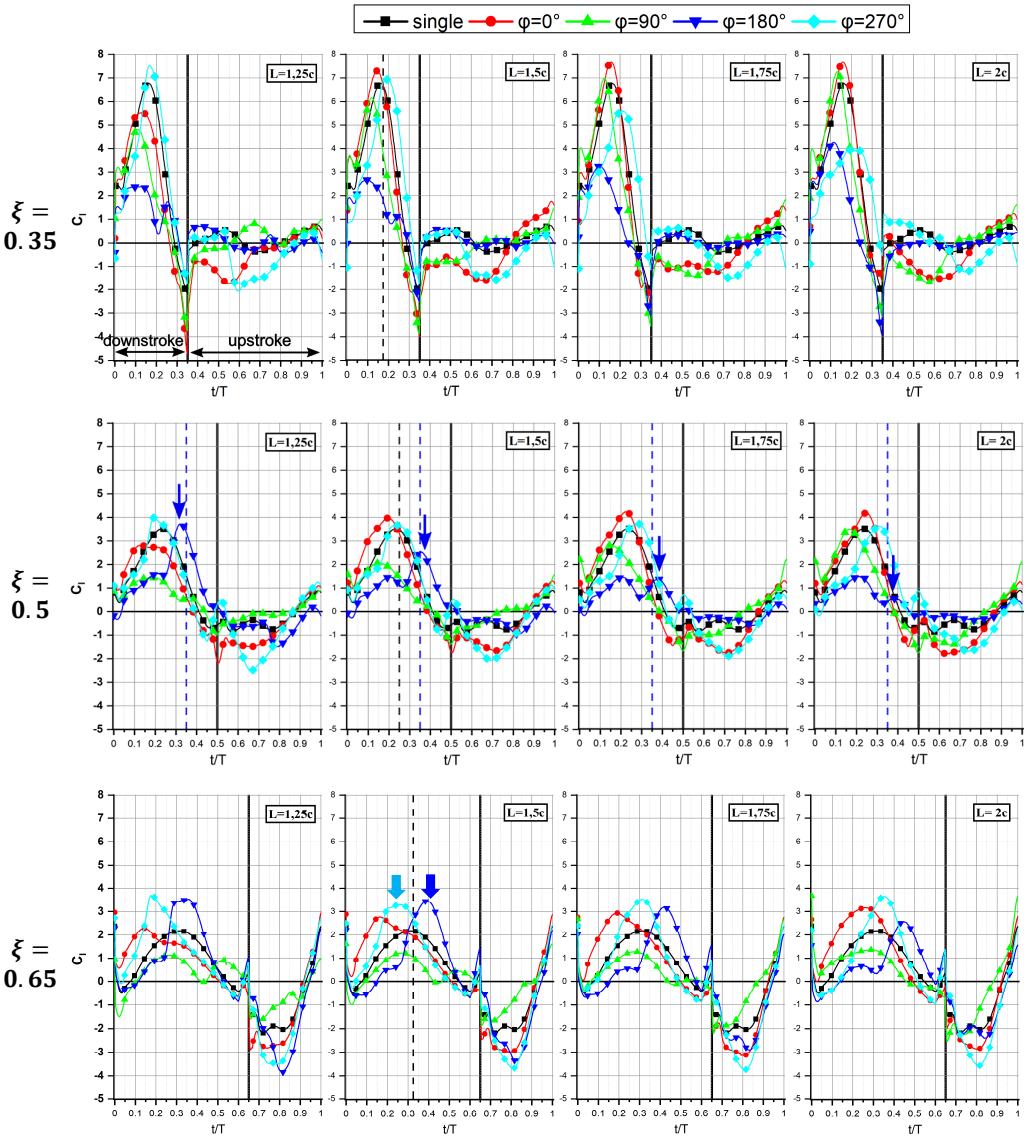

Figure 5.13 Time histories of the lift coefficient of the hindwing at different wing spacing L, phase difference φ and downstroke ratio ξ.

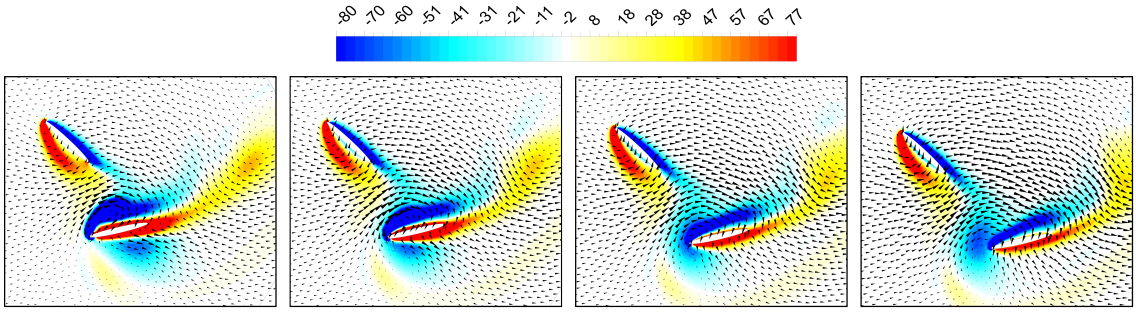

Figure 5.14 Vorticity contours for different wing spacing L. For ξ=0.5 at time=0.35T

For better insight into the effects of the downstroke ration and the phase difference on the thrust generation and the flow structure, a detail analysis on the vorticity contours is presented next.

Figure 5.15 compares the instantaneous vorticity snapshots at different phases and downstroke ratios at the middle of the downpstroke for a wing spacing of 1.5c. The vorticity contours of that of the case of a single wing are also shown as reference baseline alongside each case. The blue color represents the clockwise vorticity contours, while the red color represents the counter clockwise vorticity contours. The black arrowheads displayed on the vorticity contours represent the velocity vectors.

To get a better insight into the effects of the vorticity distribution on the lift and thrust generation, the distribution of the pressure on the hindwing is plotted in Figure 5.16.

As indicated with black rectangles in Figure 5.15, the strength of the leading edge vortex increases with the increase of the downstroke ratio, for the single wing as well as the tandem wing at φ=0°. This resulted in a significant enhancement in lift generation.

At ξ=0.35:

The counter clockwise vortex (CCW) trailing edge shed from the forewing during its downstroke induces the downwash on the lower side of the hindwing at φ=180° (as it can be seen in Figure 5.15). The increase of the velocity in the same direction of the hindwing downstroke decreased the pressure on the underside of the hindwing (as indicated with blue arrow in Figure 5.16), which resulted in low lift generation. This is consistent with the results of Wang and Sung [95], which they revealed that the production of lift force is realized through creating a downward flow. When the hindwing moves though the downwash field, the vertical force decreases.

The single wing as well as the hindwing at φ=0° and φ=270° had the highest lift generation. This is because during the downstroke, the wings avoids all the destructive vortices on its lower surface created during the previous stroke. This increases the high-pressure distribution on their lower side. Moreover, due to the absence of the vortex-vortex interaction on the upper side of the wing, the LEV formed on the top of the wing remained attached the whole of the stroke, which leads to a significant decrease of the pressure on the upper side of the wing. The combination of high-low pressure resulted in higher lift generation (see Figure 5.13).

At ξ=0.5:

At φ=90° the hindwing passes on top of the elongated TEV shed from the forewing that resulted in a drop of the pressure distribution on the lower side of the wing (see Figure 5.16). Moreover, due to induced flow created by the shed LEV from the forewing that impinges on the leading edge of the hindwing, the size of the LEV formed on the hindwing is reduced. This reduced the low pressure on the upper side of the hindwing as the green arrows indicate in Figure 5.16. As it was seen at ξ=0.35, at φ=180° the hindwing also passes through the induced downwash created by the she LEV of the forewing which had a negative effect on pressure distribution on both the upper and lower sides of the hindwing(see blue hatched area in figure 5.16).

The delayed shedding of the LEV combined with the absence of the destructive vortex-vortex interaction resulted in higher lift generation. This explains why the case of φ=270° generates the maximum lift.

It was also noticed that the lift coefficient pattern and the peaks values of the single wing and the hindwing at φ=0° were almost identical. This is due to the absence of the interaction between the hindwing and wakes shed from the forewing motion.

At ξ=0.65:

As it can be seen in Figure 5.15 (φ=90°), the LEV had the lowest magnitude. This had a negative effect on the low-pressure distribution on the upper side of the wing (see green hatched area at φ=90° in Figure 5.16), which resulted in a significantly low lift production (Figure 5.13 at ξ=0.65).

The LEV of the hindwing at φ=180° and φ=270° had a reinforcement from the shed vortices of the forewing. Where, at φ=180° the reinforcement of the LEV of the hindwing occurs after the middle of the downstroke. While at φ=270°, the reinforcement occurs before the hindwing reaches the middle of the downstroke. This explains the two peaks in the lift coefficient plots (as indicated with blue and light blue arrows in Figure 5.13).

Table 5.2 Lift coefficient at the middle of the downstroke for L=1.5c

Downstroke ratio ξ	single	φ=0°	φ=90°	φ= 180°	φ =270°
0.35	**6.65**	**6.63**	3.7	**1.74**	**6.84**
0.5	3.45	3.25	1.4	**1.19**	**3.62**
0.65	2.17	1.96	**1.05**	2.69	**2.71**

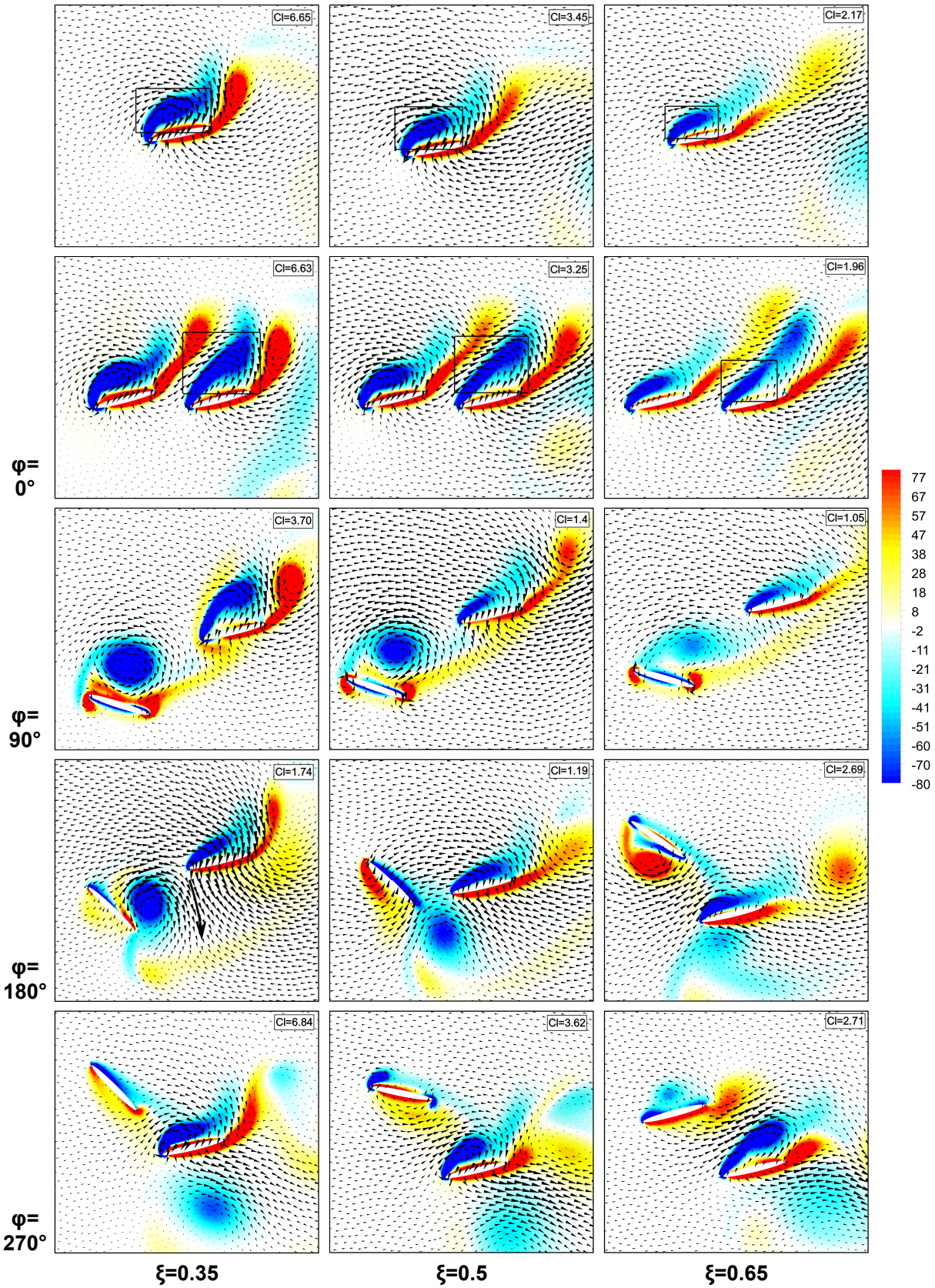

Figure 5.15 Vorticity contours for different phase difference angles and flapping ratios at the middle of the downstroke with L=1.5c.

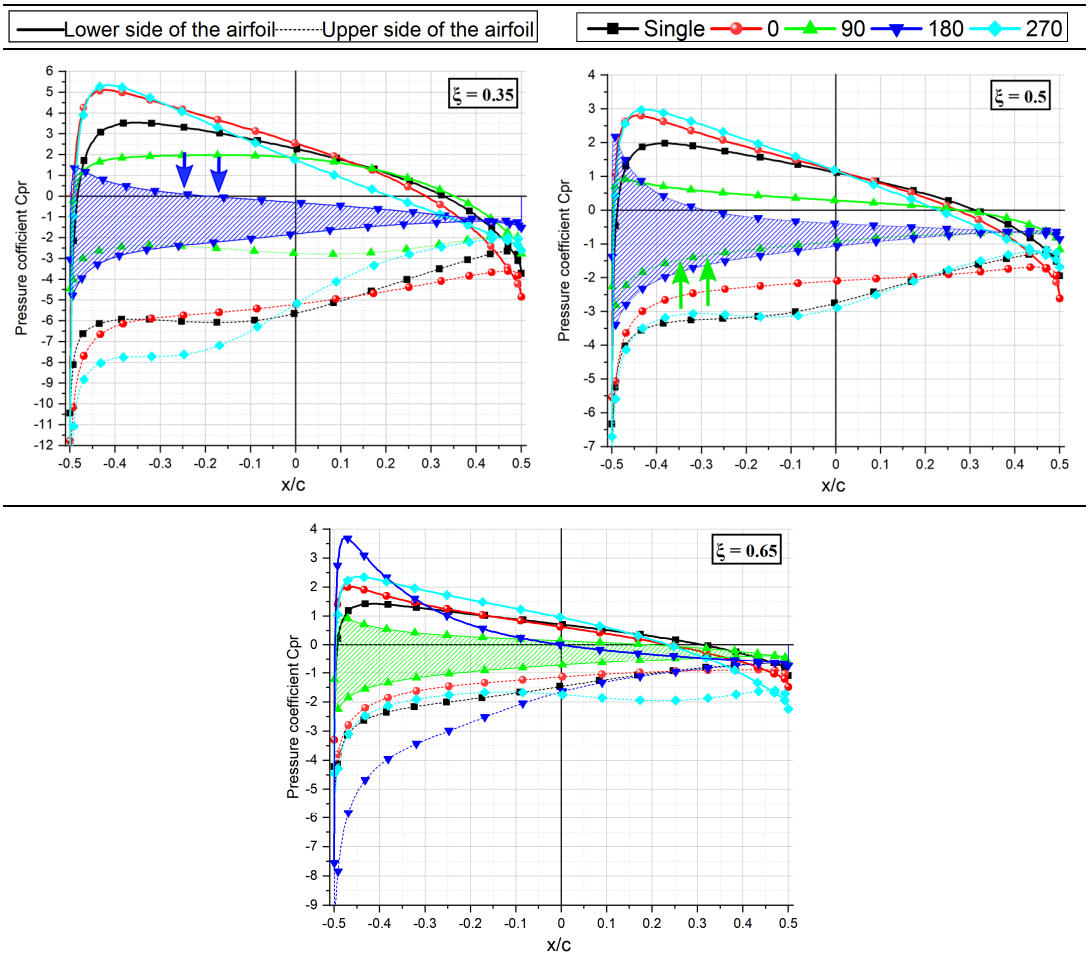

Figure 5.16 Pressure distribution on the hindwing surface for L=1.5c at the middle of the downstroke for different phases and downstroke ratios

Figure 5.17 represents the cycle-averaged values of the lift coefficient $\overline{C_l}$ responding to different values of ξ , L, at φ.

The average lift production of the tandem wing was lower than that of the single wing for all φ chosen in this study except at φ=0°.The negative lift peaks at ξ=0.65 during the upstroke were significantly higher than the other two cases (Figure 5.13). This led the average lift coefficient to drop to near zero.

The lowest averaged lift coefficient was found at φ=180° for all ξ and L values. This indicates that flapping in counter phase is not beneficial for the lift generation.

As expected from the high lift peaks observed at ξ=0.35, the averaged lift coefficient for the combined wings was also maximized at ξ=0.35. Where the highest $\bar{C}_L$ was located at L=1.5c. Compared with the case of a single wing at ξ=0.35 and the

best performance at ξ=0.5 (which was at φ=0° with L=1.5c), the maximum $\bar{C}_L$ of tandem wing showed respectively an increase of **4%** and **64%**. This indicates that using faster downstroke on tandem arrangement is very beneficial for the lift generation.

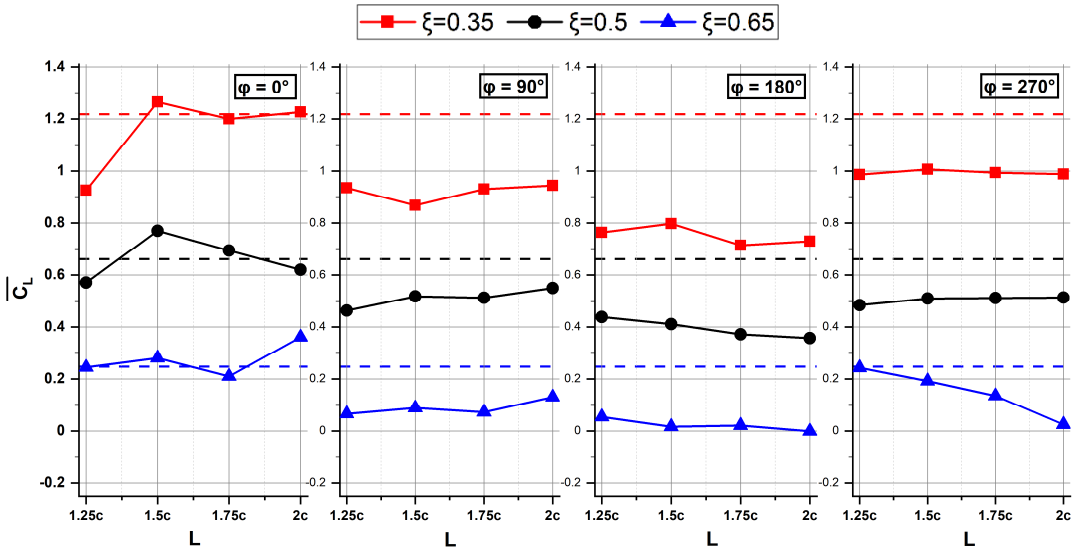

Figure 5.17 Variation of the mean lift coefficient $\overline{C_L}$

5.6.4 Effects of wing spacing, phase difference and downstroke ratio on the thrust generation

Figure 5.18 compares the time histories of the thrust coefficient of the hindwing at different values of the wing spacings L, phase differences φ and downstroke ratios ξ. Each graph also plots the results of the case of an isolated wing, which is used as a reference.

The results show that the highest thrust peaks are achieved during the upstroke for ξ =0.5 and ξ =0.65. The thrust patterns remained almost identical as the wing spacing varies. The effects of the downstroke ratio is found to be considerably larger than the other two effects.

The thrust force increases monotonically with the increase of the downstroke ratio. Where it peaked in the case of faster upstroke with a wing spacing of 1.25c and a phase difference of 180°. At the reversal (during the end of the downstroke and the beginning of the upstroke), we noticed a brief thrust peak in all cases studied. This is due to the rapid pitching-up mechanism as suggested by Dickinson et al [48].

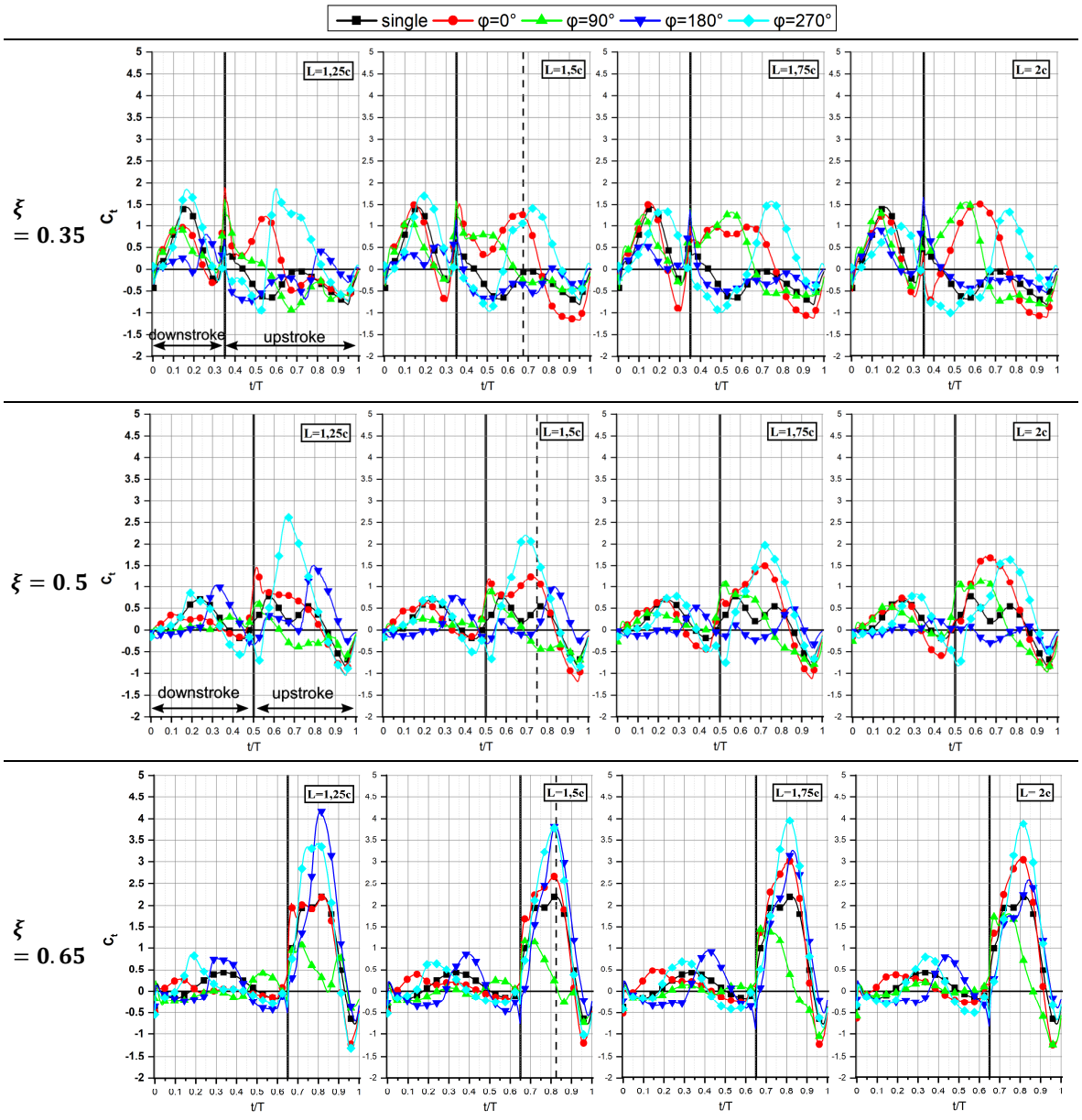

Figure 5.18 Time histories of the thrust coefficient of the hindwing at different wing spacing L, phase difference φ and downstroke ratios ξ.

It is also observed that the thrust peaks and the highest negative lift peaks are achieved at the middle of the upstroke for almost all studied cases. The thrust and lift coefficients values at that instant are presented in table 5.3 and table 5.4 respectively. These values are also labelled on the vorticity contours.

Figure 5.19 compares the instantaneous vorticity snapshots at different phase angles and downstroke ratios at the middle of the upstroke for a wing spacing of 1.5c. The vorticity contours of the case of a single wing are also shown as reference baseline

alongside each case. The pressure distribution on the hindwing at the middle of the downstroke is plotted in Figure 5.20.

As it can be seen from Figure 5.19 and Figure 5.20, the asymmetry in stroke duration influenced considerably the flow structure and the pressure on the hindwing.

For ξ=0.35:

During the upstroke, the hindwing at φ=90° passes through the LEV shed from the forewing (labelled with black squared in Figure 5.19). This explains why this case has the lowest negative lift peak. A similar behavior was also observed in the case of φ=180°. However, at φ=0° the wake-wing interaction on the upper side of the wing was not observed, which resulted a higher negative lift peak (see Figure 5.13).

The presence of the forewing side by side with the hindwing at φ=0° alters the incoming flow, which results in a significant higher thrust generation. However, for the single wing case as well as the counter stroking case (φ=180°), the incoming flow or the induced flow created by the vortex shed from the forewing impinges directly on the lower side of the wing, which results in lower thrust generation (as the black arrow shows in Figure 5.19).

For ξ=0.5:

The presence of the vortices that were shed from either the forewing or the hindwing on the upper side of the hindwing decreases the pressure distribution on the wing (as Figure 5.19 and Figure 5.20 at φ=90° show). For this reason, the case of φ=90° had the lowest thrust generation. However, this presence had a positive effect on the lift generation by lowering the negative lift peak observed during the upstroke. For this reason, the lowest negative peak was also observed at φ=90° (see Figure 5.13).

For ξ=0.65:

As it can be seen in Figure 5.19 at φ=180° & φ=270°, the size of the arrowheads on the upper side of the hindwing are relatively small which indicates low flow velocity. This implies higher-pressure stagnation (see Figure 5.20) that is due to the absence of shed vortex on the hindwing at this instance. This resulted in higher thrust generation.

At φ= 90°, the hindwing passes through the induced upwash created by the shed CW TEV from the forewing. As a result, the pressure drops on the upper surface of the hindwing. Moreover, as the black arrows indicates, the impingement of the induced flow

created by the TEV as well as the inlet flow decreases the low pressure on the lower surface of the wing (see green hatched area in Figure 5.20). This resulted in a significant low thrust production. However, as it is seen previously, this behavior leads to a significant reduction in the negative lift peak.

Table 5.3 Thrust coefficient at the middle of the upstroke for L=1.5

Downstroke ratio ξ	single	φ=0°	φ=90°	φ= 180°	φ =270°
0.35	-0.066	**1.25**	-0.25	**-0.35**	1.09
0.5	0.51	1.18	**-0.42**	0.03	**1.68**
0.65	2.2	2.64	**0.136**	**3.819**	3.73

Table 5.4 Lift coefficient at the middle of the upstroke for L=1.5c

Downstroke ratio ξ	single	φ=0°	φ=90°	φ= 180°	φ =270°
0.35	-0.37	**-1.55**	**0.15**	-0.11	-1.38
0.5	-0.75	-1.55	**0.08**	-0.44	**-1.69**
0.65	-2.03	-2.85	**-0.67**	-3.38	**-3.6**

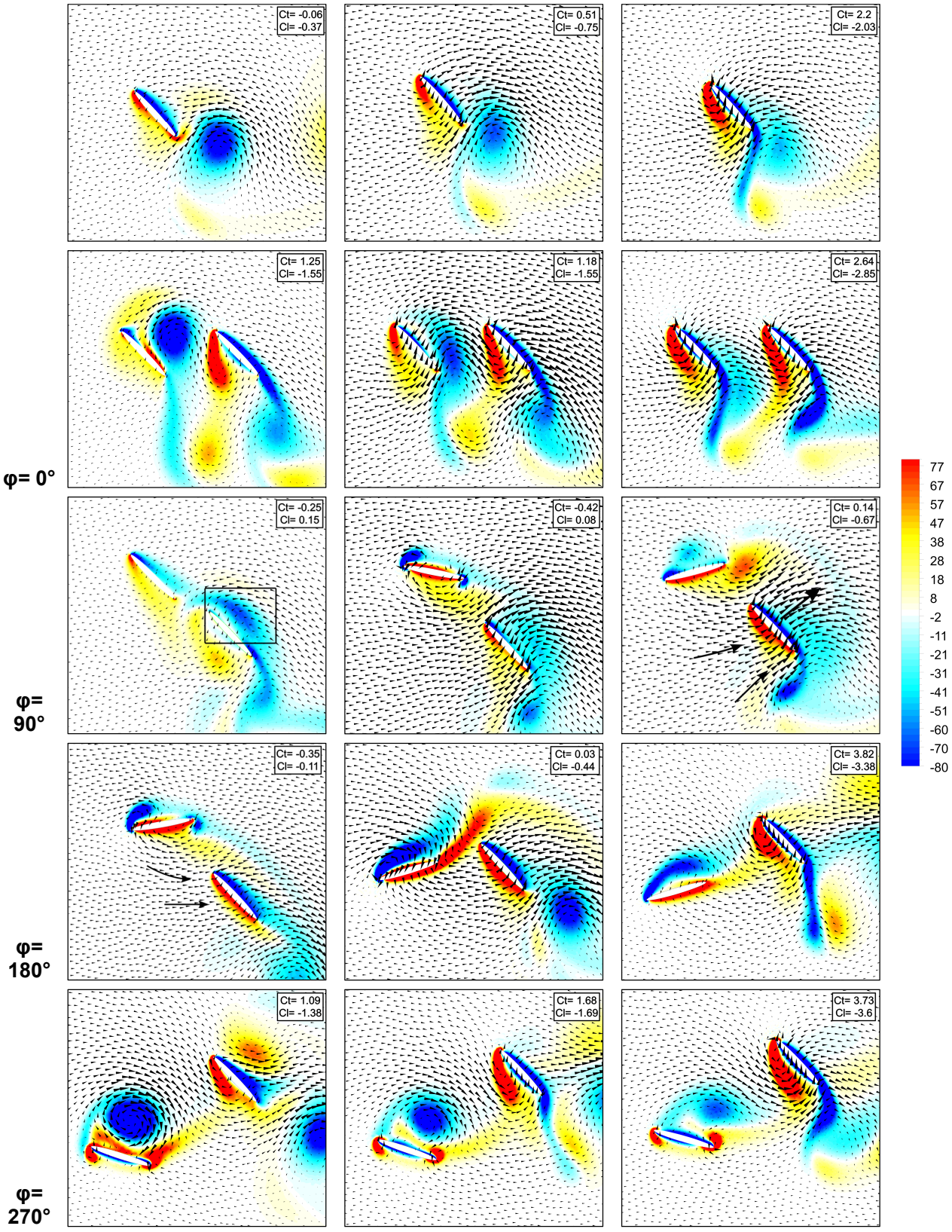

Figure 5.19 Vorticity contours for different phase difference angles and flapping ratio at the middle of the upstroke for L=1.5c.

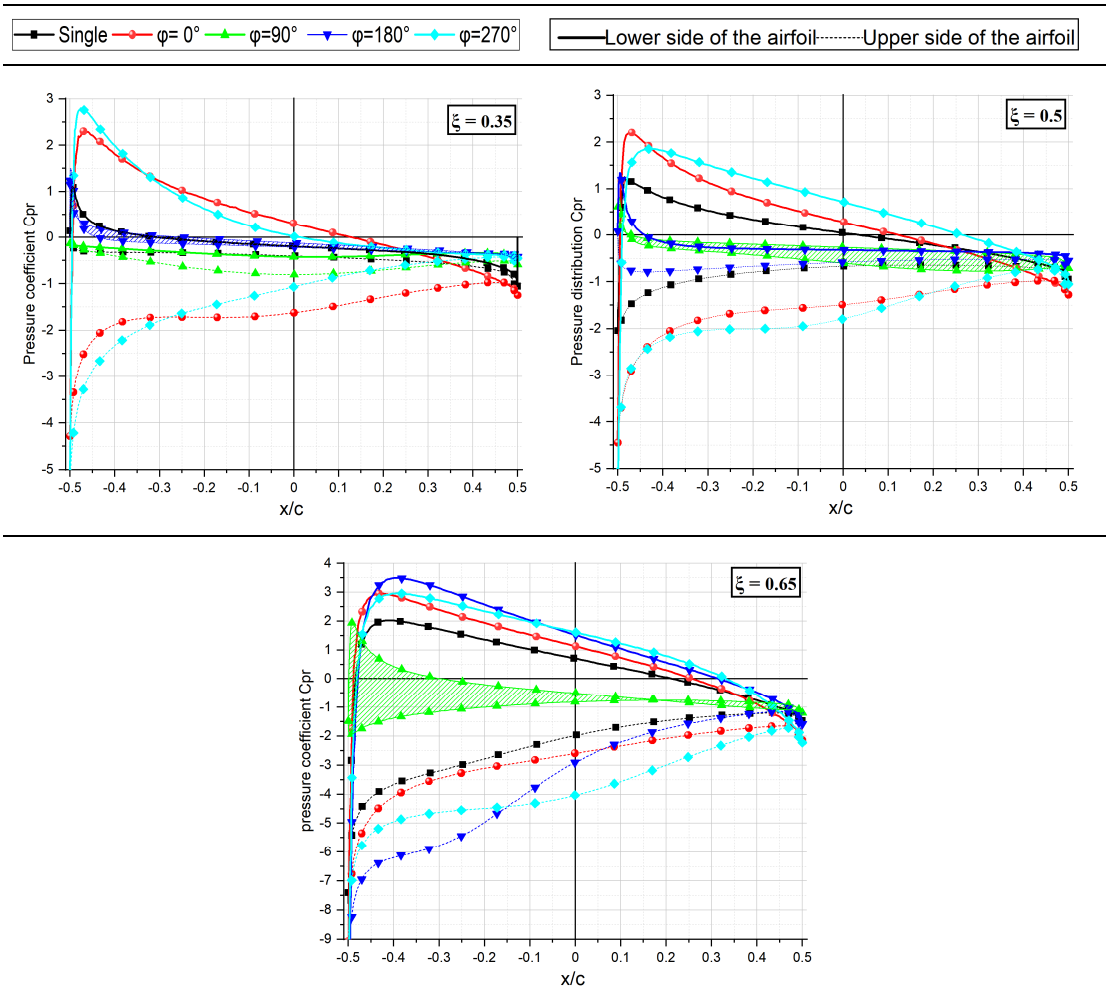

Figure 5.20 Pressure distribution on the hindwing surface for L=1.5c at the middle of the upstroke for different phases and downstroke ratios

The results of the mean thrust force coefficient $\overline{C_T}$ are presented in Figure 5.21.

As the wing spacing and the difference angle varies, the changes in the mean lift coefficient become quit complex. Unlike for the lift production, the Tandem wing configuration produced more thrust than the case of a single wing except in the case of ξ=0.35 at φ= 90°. This is due to the destructive vortex interaction observed in this case.

As it is seen from the averaged lift coefficient results, flapping in counter phase also produces the lowest thrust at φ= 180°.

The thrust force of the tandem wing was maximized in the case of the faster upstroke with wing spacing of 1.75c and phase difference of 0°, where it showed **26%** and **43%** increase relative to the case of single wing at ξ=0.65 and the best performance at ξ=0.5 (which it was at φ= 270° and L=1.75c), respectively.

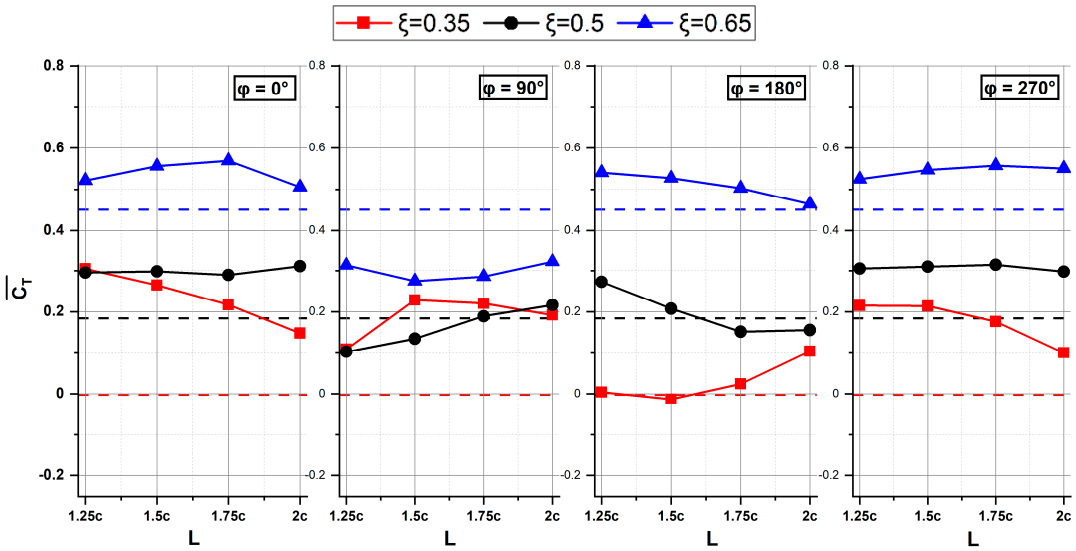

Figure 5.21 Variation of the mean thrust coefficient $\overline{C_T}$

The purpose of this study is to develop a better understanding onto the effects of the three kinematic parameters mentioned above for possible application on the Micro and Nano air vehicle designs. Since these vehicles use batteries as power source to generate the flapping movement, the study the energy required to perform a complete stroke is highly important.

Figure 5.22 compares the time histories of the energy coefficient of the hindwing at different values of the wing spacing L, phase difference φ and downstroke ratios ξ.

The positive energy coefficient represents power output by the system. However, a negative energy coefficient represents power put back to the system and since it is impractical for the wing to regenerate energy, the negative values of the energy coefficient are set as zero. It is noticed that the energy coefficient peaks were found at the same location of the highest lift and thrust production. This concludes that high aerodynamic forces come with a cost of high-energy consumption.

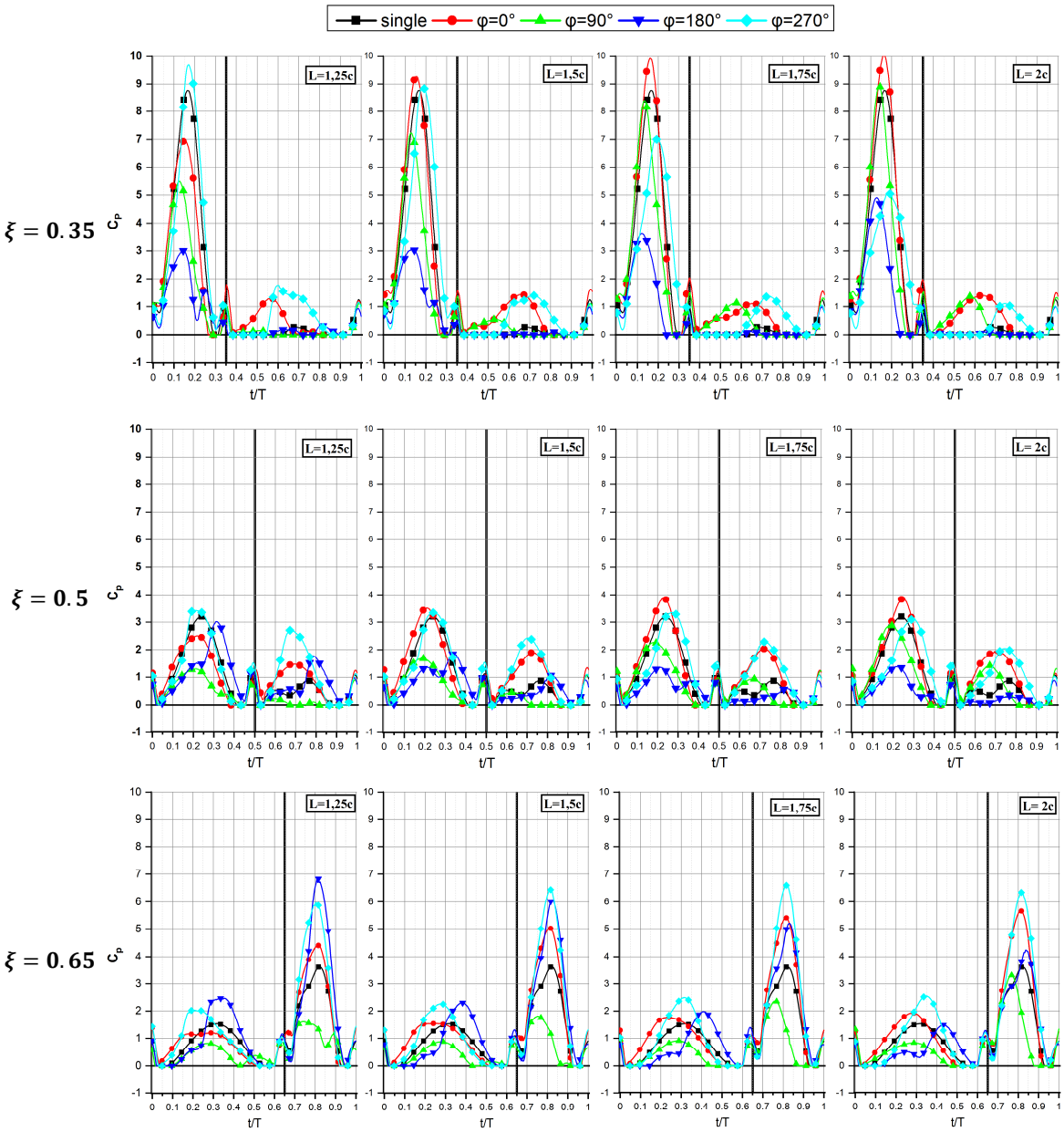

Figure 5.22 Time histories of the energy coefficient of the hindwing at different wing spacing L, phase difference φ and downstroke ratio ξ.

The results of the mean energy coefficient $\overline{C_p}$ responding to different ξ are presented in Figure 5.23.

It was found that the case of symmetrical stroke (ξ=0.5) results in minimal energy consumption. Where the lowest energy consumption was found for the case of counter phase flap (φ=180°). The energy consumption was maximized at φ =0° for all wing spacings L.

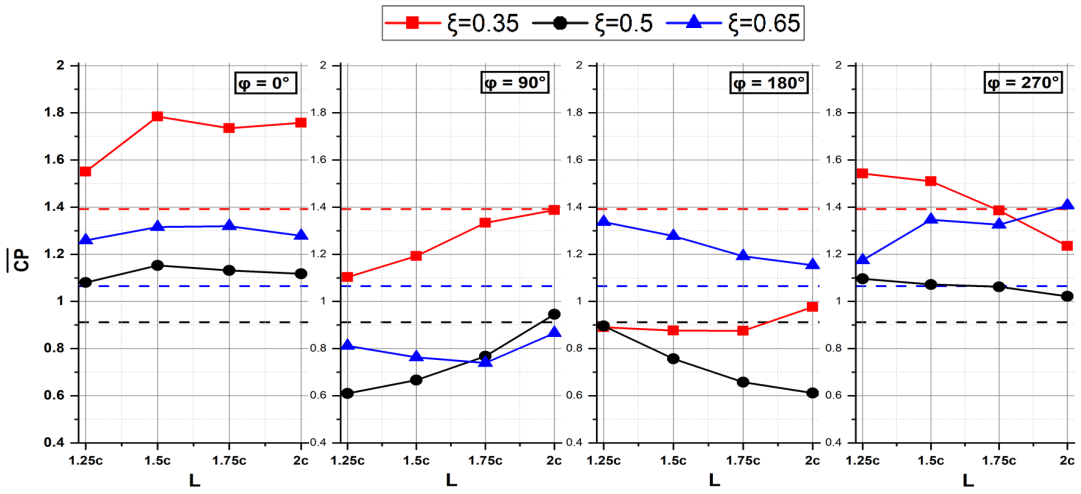

Figure 5.23 Variation of the mean energy coefficient $\overline{C_p}$

5.6.5 Effects of wing spacing, phase difference and downstroke ratio on the thrust and lift efficiencies

Figure 5.24 represents the thrust efficiency η_T , at different ξ, φ and L.

The variation of wing spacing and phase difference had a negligible effect on the thrust efficiency at ξ=0.65.

The lowest propulsive efficiency was located in the case with faster downsroke at φ=180° which was due to the effect of direct impingement of the incoming flow on the hindwing. The maximum thrust efficiency is located at ξ=0.65 for all wing spacing and phase differences studied. Where it was maximized at φ =270° with L=1.25c with over **6%** higher than the case of a single wing at ξ=0.65 and **46%** than the best performing tandem configuration at ξ=0.5.

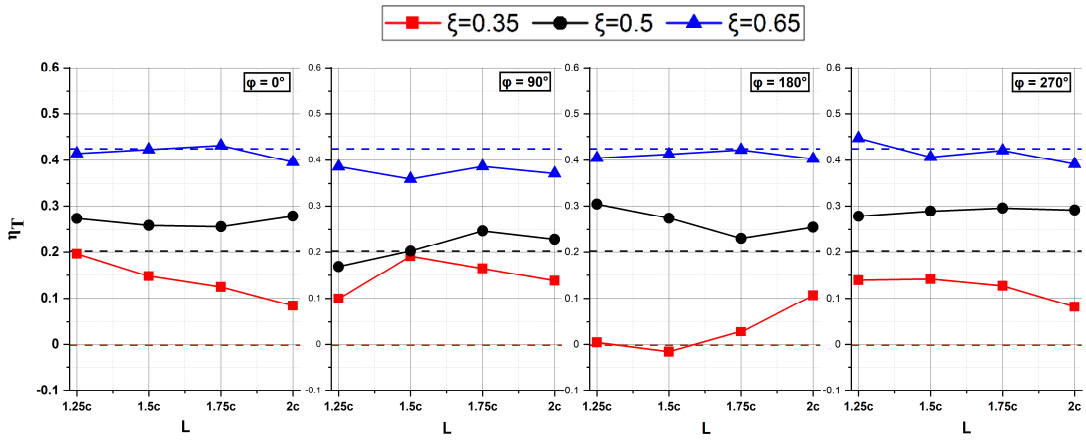

Figure 5.24 variation of the thrust efficiency η_T.

The results of the lift efficiency η_L are presented in Figure 5.25. A linear response is observed between the downstroke ration and the lift efficiency. As it is seen from the results of the average lift coefficient, the lowest lift efficiency was also located at ξ=0.65.

The case of ξ=0.35 is found to generate the highest lift as well as highest lift efficiency. Unlike what it was seen from the results of the average lift coefficient where the lowest lift generation was located at φ=180°, the highest lift efficiency was also located at this phase angle. This is consistent with the experimental results of Dong and Liang [96], where they concluded that the instructive interaction increases the lift force while the destructive interaction increases the efficiency. The case with L=1.5c showed an increase of 4% and 17% than that of a single wing at ξ=0.35 and the best performance configuration at ξ=0.5 (which it was at φ=90° with L=1.5c).

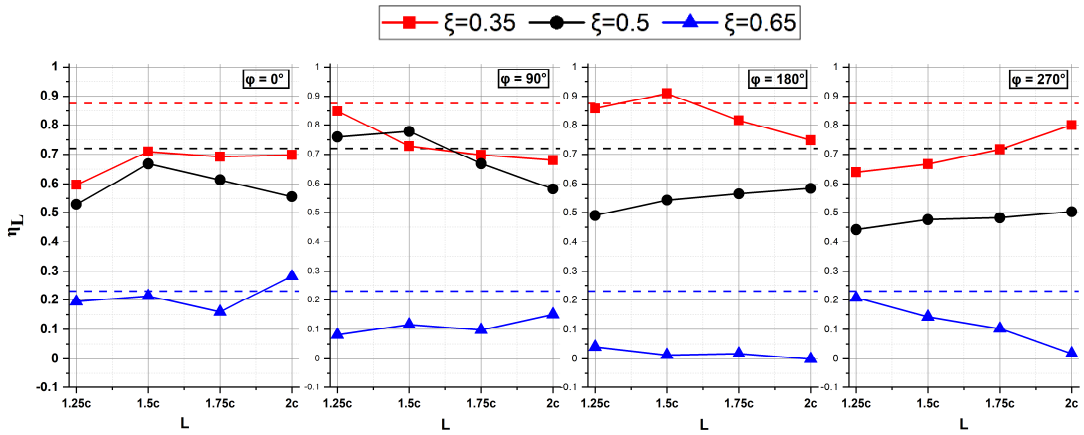

Figure 5.25 variation of the lift efficiency $\boldsymbol{\eta_L}$.

5.7 Conclusion

In this chapter, the effects of the asymmetry in flapping duration, wing spacing and phase difference on the thrust and lift generation as well as energy consumption and the flow structure were investigated. The effects of the downstroke ratio were dominating. Three unsteady mechanisms used by naturel flyers were identified in this analysis, the wake capturing, fast pitching rotation and rapid acceleration. It was noticed from the overall results that during the downstroke the wings generate most of lift force, and during the upstroke the wings generate most of the thrust force. The lift and thrust forces were maximized in the case of the faster downstroke and upstroke, respectively. This was due to the effects of rapid acceleration mechanism.

As for the energy consumption, it was found that the case of symmetrical stroke results in minimal energy consumption, where the lowest energy consumption was found for the case of counter phase flap which was due to destructive wing wake interaction observed in at this phase.

The thrust efficiency with faster upstroke was higher than the symmetrical stoke in all cases studied. However, the lift efficiency was maximized with faster downstroke instead. This concludes that the asymmetry in flapping duration has more importance that the wing spacing and phase difference.

CHAPTER 6: Effects of initial position and asymmetry in flapping frequency on tandem wing at Re=5000

6.1 Introduction

In this chapter, we investigate the effects of the initial position and the dissimilarity in the flapping frequency on tandem wing in forward flight. The Reynold number chosen for this study is 5000.

In the first part of this study, we vary the initial position of the forewing with an interval of 0.25c (c is the chord length) while keeping the flapping frequency of both wings the same. Each initial position is tested at four phases of 0°, 90°, 180° and 270°. In the second part, we vary the frequency of both wings regularly so that the periodic state can be achieved. The effects of these parameters on the aerodynamic forces, energy consumption and the flow structure are deeply investigated.

6.2 Kinematic description and boundary conditions

6.2.1 Kinematic description

Both the single and tandem wing arrangements are considered in this study. The wings configuration and kinematics used in this chapter are chosen the same as the studies of Broering and Lian [97, 66], where the Strouhal number and the reduced frequency are set respectively at St=0.3 and K=0.942.

A flat plat with 0.05 of thickness ratio is employed. The flapping motion is a combination of a translation A(t) and rotation α(t) applied for both the single and tandem wing cases.

The mathematical description of translation and rotation motion at different phases can be described by:

$$A(t) = A_0 + \int_0^t V(t)dt \qquad (6.1)$$

$$\alpha(t) = \alpha_0 + \int_0^t \omega(t)dt \qquad (6.2)$$

Where

$$V(t) = 2\,\pi\,\varepsilon f\,A_m\,sin(\,2\,\pi\varepsilon f t\,) \qquad (6.3)$$

$$\omega(t) = 2\,\pi\,\varepsilon f\,\alpha_m(\,2\,\pi\varepsilon f t + \varphi) \qquad (6.4)$$

Where A_0 is the initial position, α_0 is the initial rotation ($\alpha_0 = 5°$), $V(t)$ is the translation velocity, $\omega(t)$ is the angular velocity, A_m is the amplitude of translation, t is the time, α_m the amplitude of rotation, ε is the frequency factor and f (f= 0.3Hz) is the flapping frequency.

The amplitude of translation and rotation are fixed at 0.5c and 20° respectively. The wing spacing L is fixed at 2c.

The schematic of the tandem wing motion is shown in Figure 6.1.

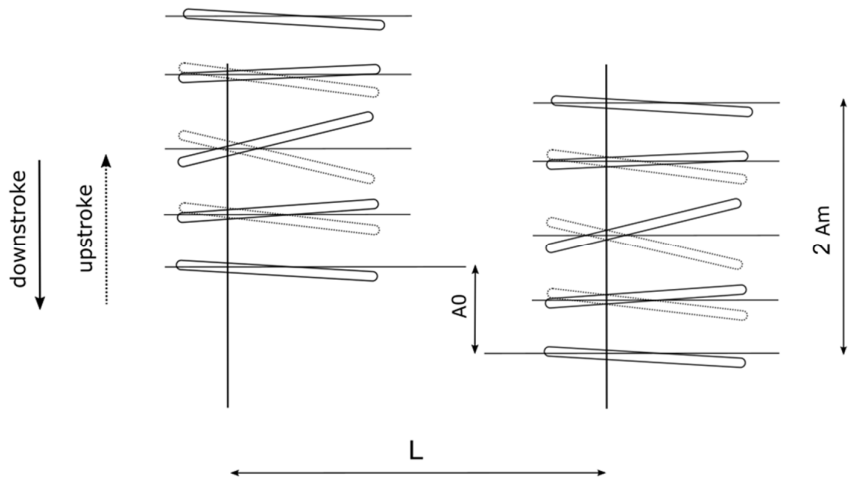

Figure 6.1 Schematic of the tandem wing motion.

6.2.2 Boundary conditions and mesh generation

To solve the flow field around flapping tandem wing, the commercial software ANSYS Fluent was employed. The computation domain dimensions are 20c by 15c as it is shown in Figure 6.2. The wall surface of the wings was set as no slip. The inlet boundary was set to the left side of the domain while the right, top and bottom of the domain were set as pressure outlet.

The computational domain was divided into two zones, the dynamic zone were the re-meshing occurs and the stationary zone which covers the rest of the domain outside the dynamic zone. For both zones, a triangular mesh was used as shown in Figure 6.3.

A pressure based Navier stockes solver is applied. The pressure velocity coupling is achieved by using SIMPLE algorithm. The momentum equation is discretized using a second order upwind scheme.

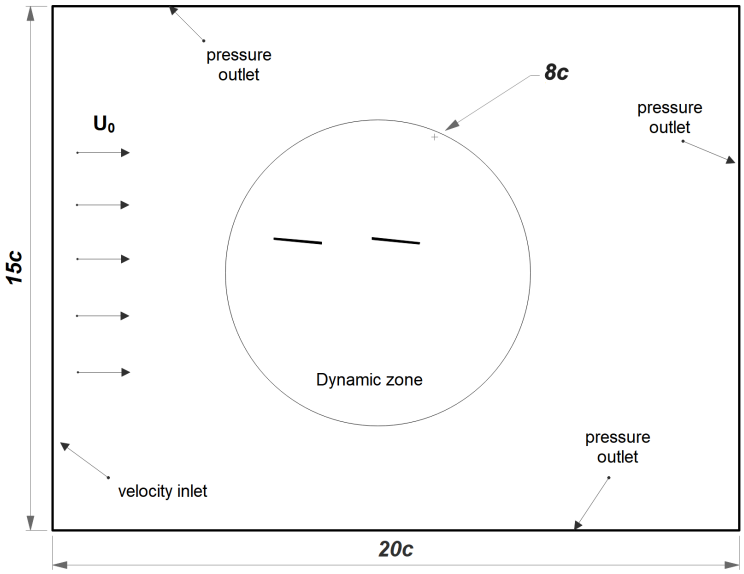

Figure 6.2 Computational domain and boundary conditions

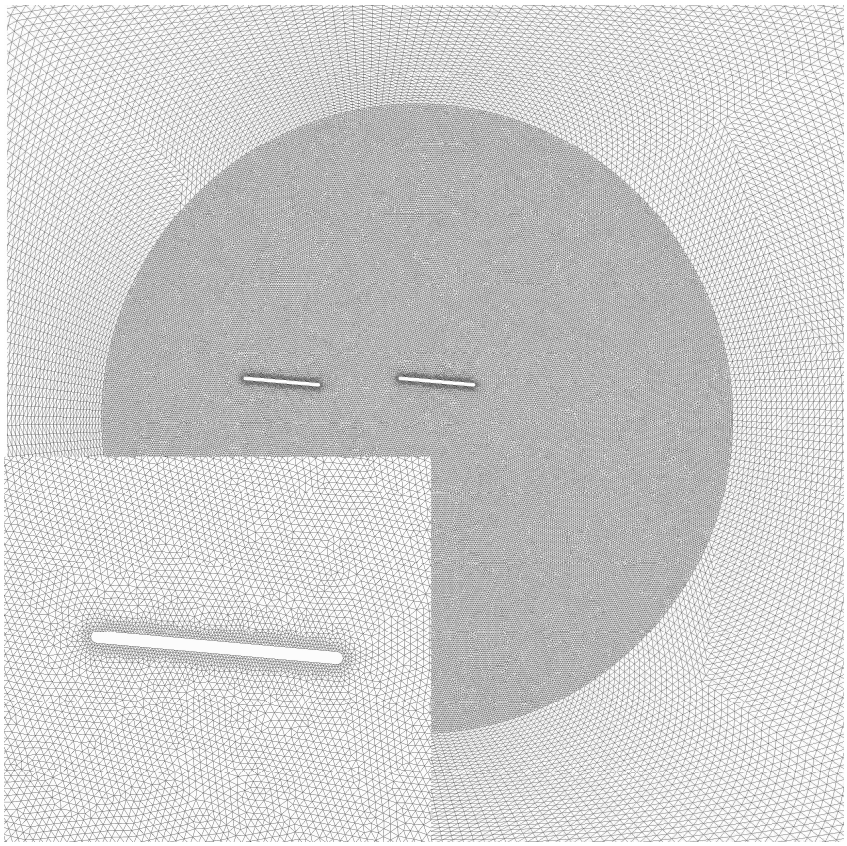

Figure 6.3 Computational grid used in this study.

6.3 Validation of numerical method

The present case was first validated through a comparison with the results obtained by Broering and Lian [97]. The present results showed a good agreement with the results obtained in the study mentioned above, as it is shown in Figure 6.4.

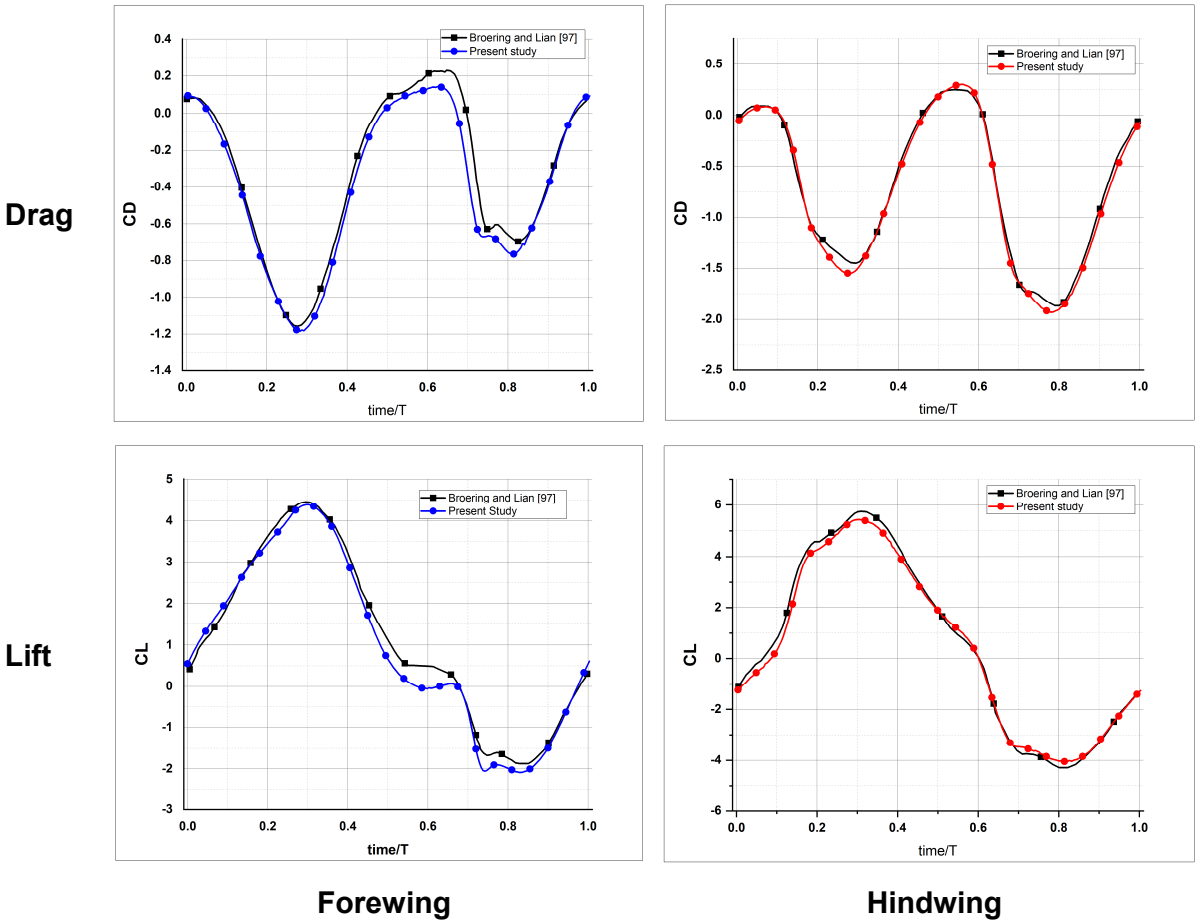

Figure 6.4 Comparison of the time histories of the lift coefficient and drag coefficient of the present study and the results obtained from the literature.

6.4 Results and discussion

The Reynolds number was fixed at 5000. The results obtained in this work were taken from at least the 20th period where the flow is guaranteed to reach a periodic state.

6.4.1 Effect of initial position

In this part, the starting position of the forewing is shifted upward and downward with an interval of 0.25c. Four phase differences were considered $\varphi = 0°, 90°, 180° \text{ and } 270°$. The frequency factor ε is set as 1.

The time histories of the translation displacement and rotation velocities for the case of $\varphi = 180°$ are plotted in Figure 6.5.

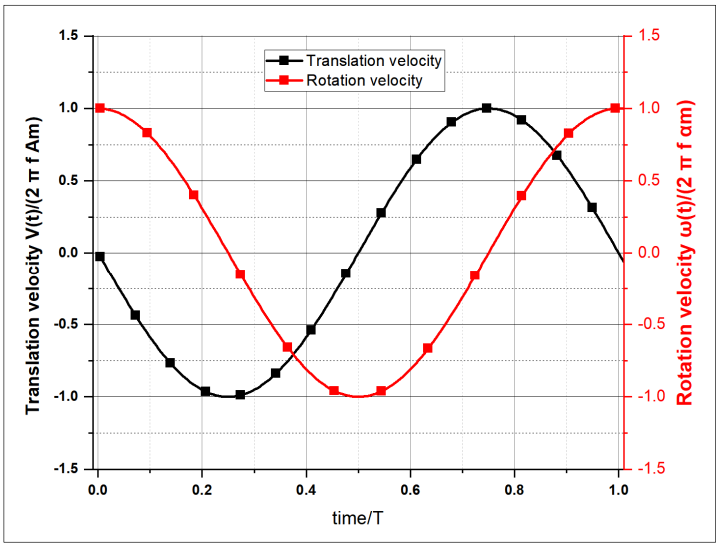

Figure 6.5 Time histories of the flapping motion used in this study. a) Translation velocity $V(t)$, b) rotation velocity $\omega(t)$

Figure 6.6 and Figure 6.7 plot respectively the results of the lift for the fore and hind wings at different initial positions and phase differences. As it can be seen in Figure 6.6, the variation of the lift coefficient of the forewing remained almost unchanged as the A_0 and φ vary, which indicates that the hindwing had minor effect on the aerodynamics of the forewing. However, the lift generation of the hindwing was considerably affected by the variation of A_0 and φ as Figure 6.7 shows. The enhancements in the aerodynamic performance that were due to the variation in the phase difference were suggested by previous study of Lim and Tay [98]. To highlight the interplay between the flow contours and lift generation, the vorticity (left side) and pressure (right side) contours are presented side-by-side next in each of Figure 6.8 and Figure 6.9.

For φ=0°

As A_0 increases, the shed CCW LEV created during the upstroke of the hindwing is delayed (see Figure 6.8), which causes the pressure distribution on the lower side of the hindwing to drop. Moreover, the hindwing passes under the shed LEV of the forewing, which dampens out the strength of the LEV that is created on the hindwing. Consequently, the low-pressure area created on the upper side of the hindwing is reduced. This resulted in significant low lift production as Figure 6.7 indicates.

For φ=90°

As it was seen in the case of φ=0°, the lift production decreases with the increases of A_0 which was due to the decrease of the pressure distribution on the lower side of the hindwing. However, the lift production in this case was maximized at A_0=0c. This is due the constructive interaction between the elongated TEV shed from the forewing and the LEV forming on the hindwing. This led to a significant increase in the size of the LEV, which resulted in larger lower pressure area on the hindwing as Figure 6.8 shows.

The benefit of the hindwing from the unsteady flow generated by the forewing was also observed by Somps and Luttges in their experiments on dragonfly's wings motion [99].

For φ=180°

Unlike the previous cases, the lift production increases with the increase of A_0 in the case of counter stroking. Whereas A_0 increases, the hindwing avoids the destructive vortex left from the forewing. This increases the pressure on the lower side of the hindwing. Moreover, the induced flow caused by the shed LEV of the forewing enlarges the size the forming LEV on the hindwing, which resulted in lower pressure on the hindwing. The combination of lower pressure on the upper side and higher pressure on the underside of the hind wing resulted in higher lift production at the maximum A_0=1.5c.

As A_0 decreases, the shed LEV by the forewing generates a downwash on the underside of the hindwing. The induced velocity decreases the pressure on the underside of the wing, which results in low lift production. This was also suggested by Wang and Sun [95] in their paper.

For φ=270°

At A_0=0.5c, the hindwing passes through the CW LEV shed from the forewing. This interaction led the pressure on the lower side of the wing to drop significantly when it is compared with the other cases. This explains the low lift production observed in this case. Conversely, due to the absence of the destructive interaction between the hindwing and the shed forewing resulted in a relatively higher pressure on the underside of the hindwing, which, as a result enhanced the lift production.

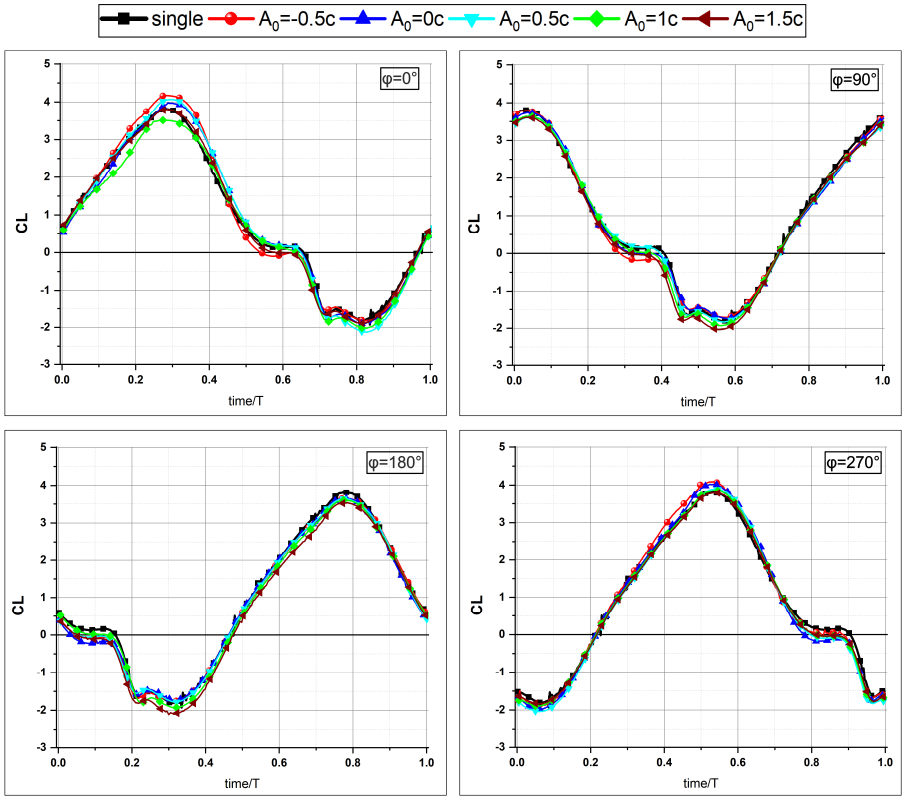

Figure 6.6 Time histories of the lift coefficient of the Forewing at different phase angles.

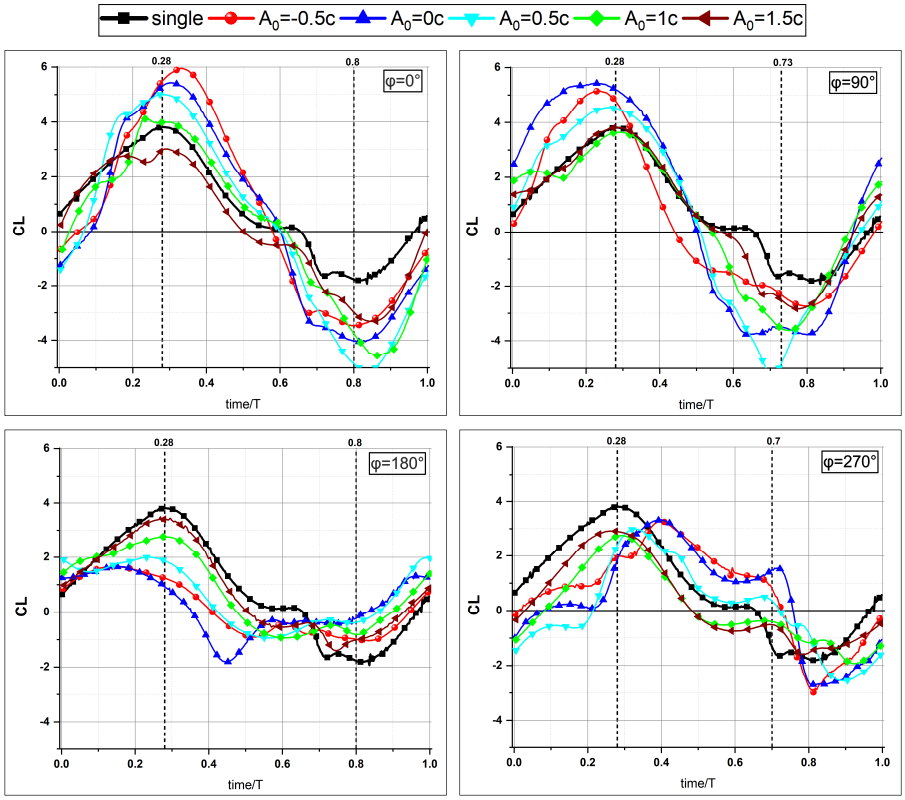

Figure 6.7 Time histories of the lift coefficient of the Hindwing at different phase angles

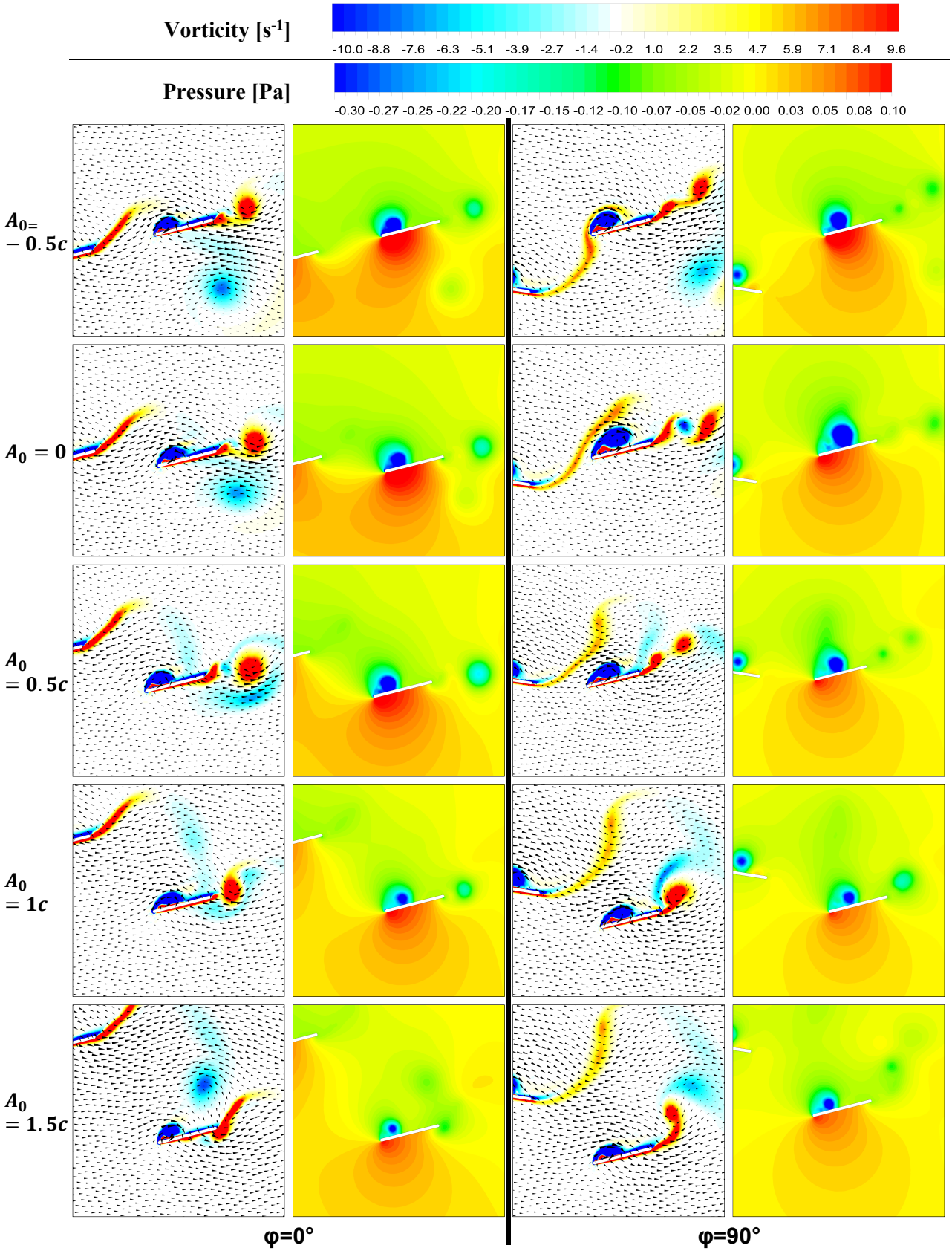

Figure 6.8 Vorticity and pressure contours around the hindwing for φ=0° and φ=90°at t/T=0.25.

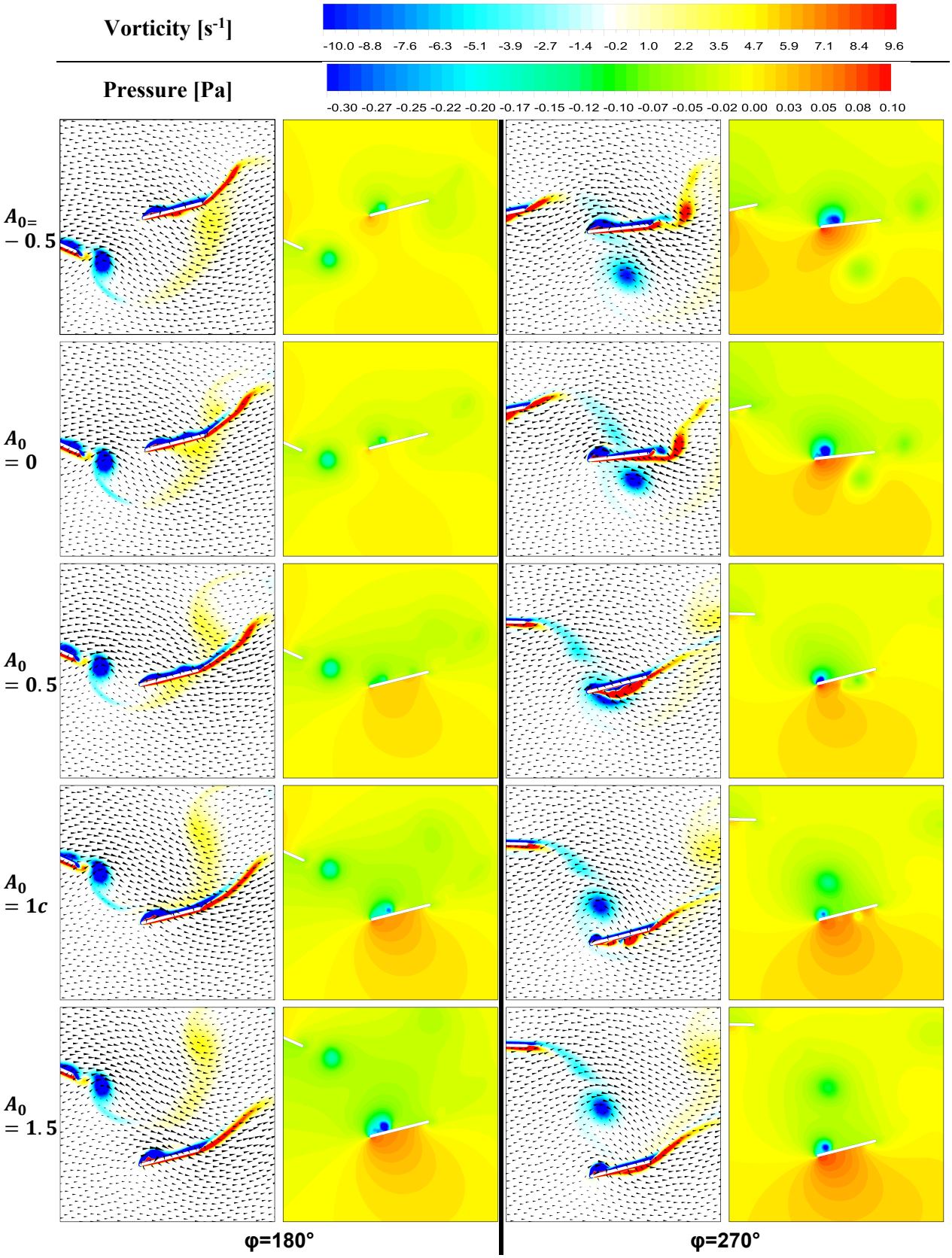

Figure 6.9 Vorticity and pressure contours around the hindwing for φ=0° and φ=90°at t/T=0.25

Figure 6.10 represents the average values of the lift coefficient for both the fore and hind wings compared with the case of a single wing. The case of φ=180° showed an increase of lift production as A_0 increases. However the case of φ=0° and φ=270° showed an increase of lift production as the A_0 decreases. The single wing outperformed all cases studied except the case of φ=90° with A_0=0c. This can be seen in Table 6.1, which shows an increase of **0.5%** in the average lift coefficient compared with the single wing case. At φ=180°, shifting the initial position upward with 1c resulted in a highest increase of the average lift with **43.8%.**

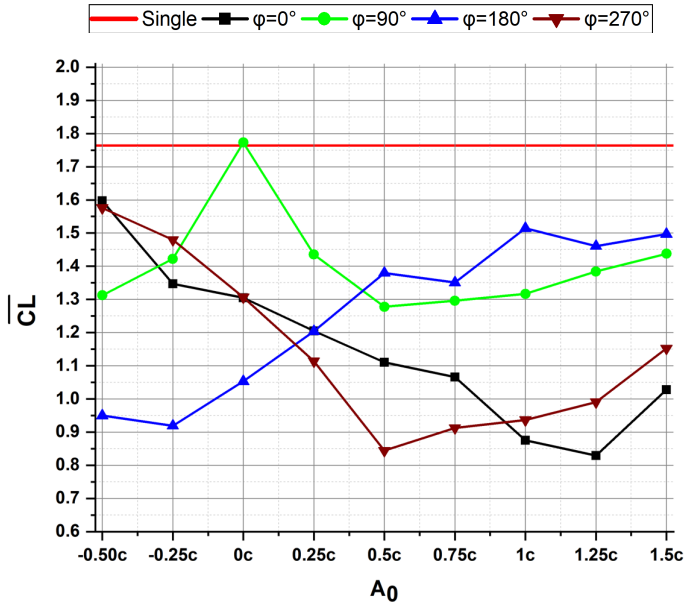

Figure 6.10 Time averaged $\overline{C_L}$ of combined Fore/hind wing

Table 6.1 average lift coefficient of the best performing tandem wing configuration ($\overline{C_{Lb}}$) compared with the single ($\overline{C_{Ls}}$) case as well as the tandem wing at A_0=0c ($\overline{C_{L\,0c}}$)

Phase difference	Increase compared with that of a single wing (%) $\frac{\overline{C_{Lb}} - \overline{C_{Ls}}}{\overline{C_{Ls}}} \times 100$	Increase compared with Tandem wing at A_0=0c (%) $\frac{\overline{C_{Lb}} - \overline{C_{L\,0c}}}{\overline{C_{L\,0c}}} \times 100$	Best performing configuration
φ=0°	**-9.4%**	**22.3%**	A_0= -0.5c
φ=90°	**0.5%**	**-18.9%**	A_0=1.5c
φ=180°	**-15.1**	**43.8%**	A_0=1c
φ=270°	**-10.6**	**20.6%**	A_0= -0.5c

The results of the thrust for the fore and hind wings at different initial positions and phase differences are plotted in Figure 6.11 and Figure 6.12 respectively. Figure 6.13 and Figure 6.14 illustrate the vorticity and the pressure contours at the middle of the upstroke at different initial positions and phase differences.

It is seen that the effects of the initial position on thrust coefficient of the hindwing are significant where we notice a distinct pattern of C_t as A_0 varies. However, the variation of the thrust coefficient of the forewing remained almost unchanged as A_0 varies

The thrust peaks occur around the middle of the downstroke (where most of the thrust force is generated) and the middle of the upstroke for both the fore and hind wings. Increasing the initial position tends to increase the thrust peaks of the hindwing, whether during the downstroke or the upstroke.

For φ=0°

As Figure 6.12 indicates, the case of A_0=0.5c had the maximum thrust peak and as a result the thrust generation was maximized around this position. This was due to the larger CCW LEV formed on the lower side of the hindwing. Moreover, as A_0 decreases, the shed LEV generated by the forewing passes below the hindwing during its upstroke. This increases the high pressure on the upper side of the hindwing.

For φ=90°

At A_0=0.5c, the hindwing interacts with shed CW LEV by the forewing. This interaction reinforces the CCW LEV formed on the hindwing, which, as a result, the pressure on the lower side of the hindwing decreases significantly (see Figure 6.13). This low pressure creates a suction zone, which pulled the hindwing against the incoming flow. Consequently, the thrust production is significantly improved by created a much higher thrust coefficient peak (see Figure 6.12).

For φ=180°

The size of the LEV formed on the top of the hindwing at the middle of the downstroke increases slightly as A_0 increases till it reaches its maximum size at A_0 =1.5. At A_0=0, during the upstroke the hindwing passes through the vortex shed from the forewing. This accelerates the flow on the upper side of the hindwing during its upstroke. As a result, the pressure on the upper side of the wing decreases as the pressure contours indicate (see Figure 6.14). This results in significant drop in thrust production.

As A_0 increases, this interaction slowly disappears as indicated with black squares in Figure 6.14 (t=0.8T)

For φ=270°

In Figure 6.12, we notice for the first time the presence of a significant negative thrust peak during the upstroke at A_0=-0.5c, A_0=0c and A_0=0.5c. The shed of the LEV created by the hindwing during its downstroke was delayed as A_0 decreases. This was due to the reinforcement of the elongated TEV of the forewing. The diminution of the pressure on the upperside of the hindwing resulted in the negative thrust production.

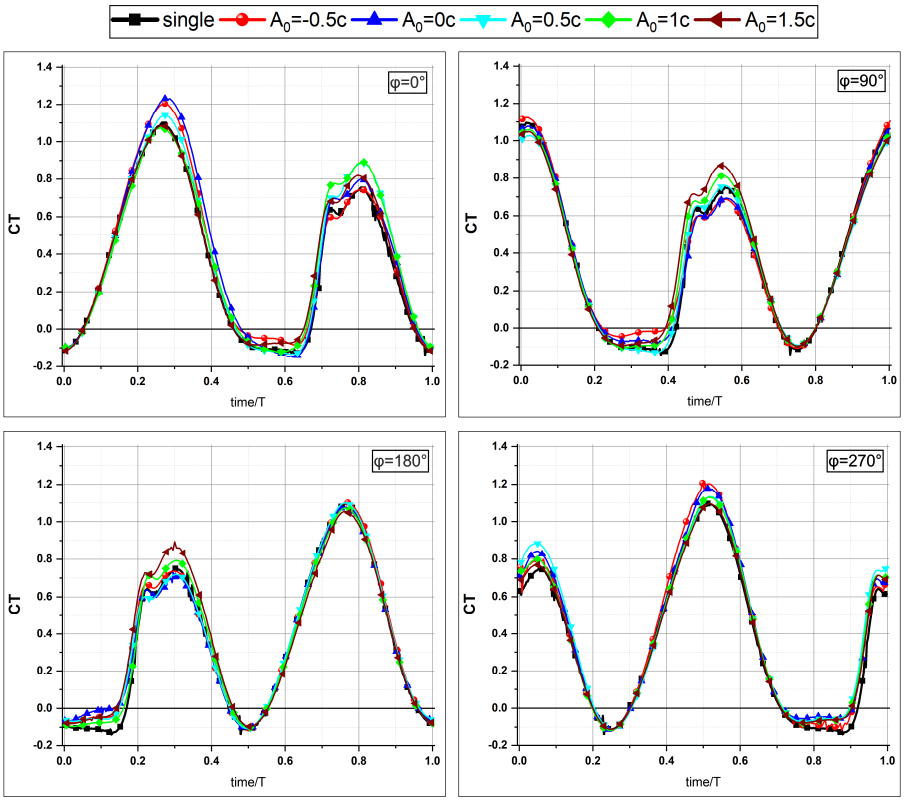

Figure 6.11 Time histories of the thrust coefficient of the Forewing at different phase angles.

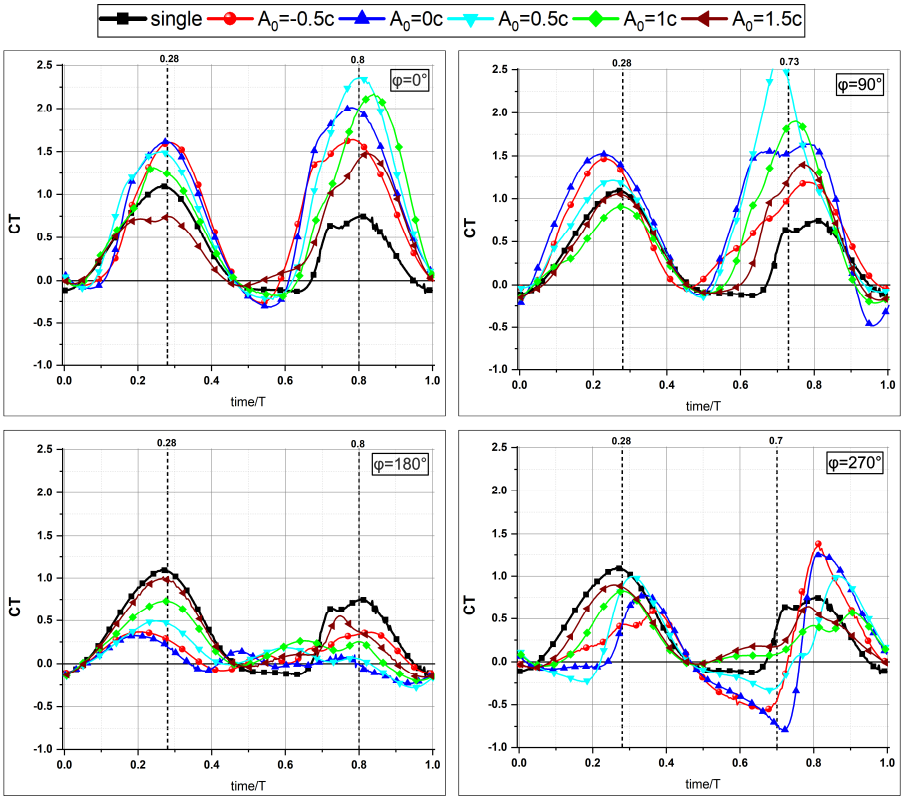

Figure 6.12 Time histories of the thrust coefficient of the Hindwing at different phase angles.

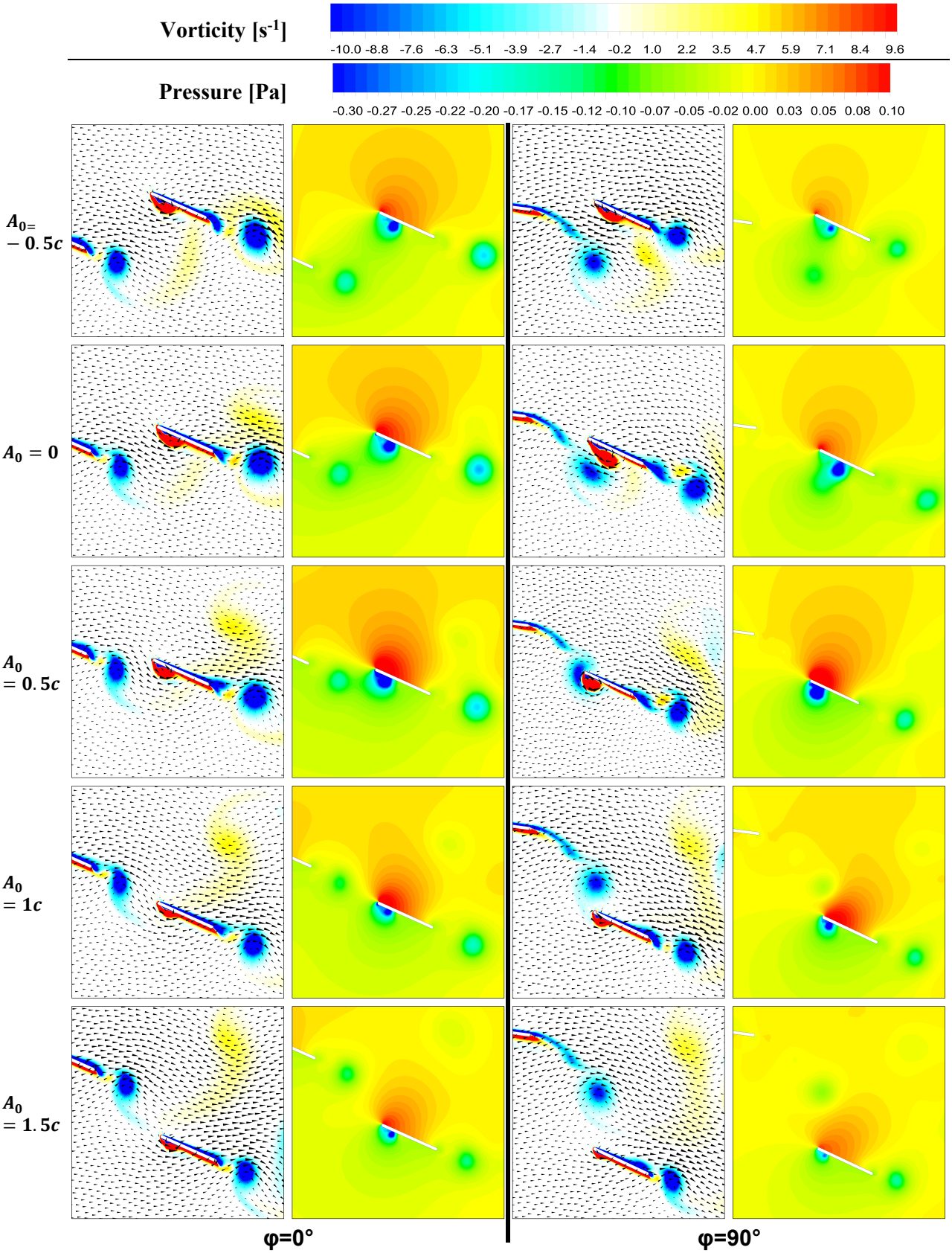

Figure 6.13 Vorticity and pressure contours around the hindwing for φ=0° and φ=90°at t/T=0.75.

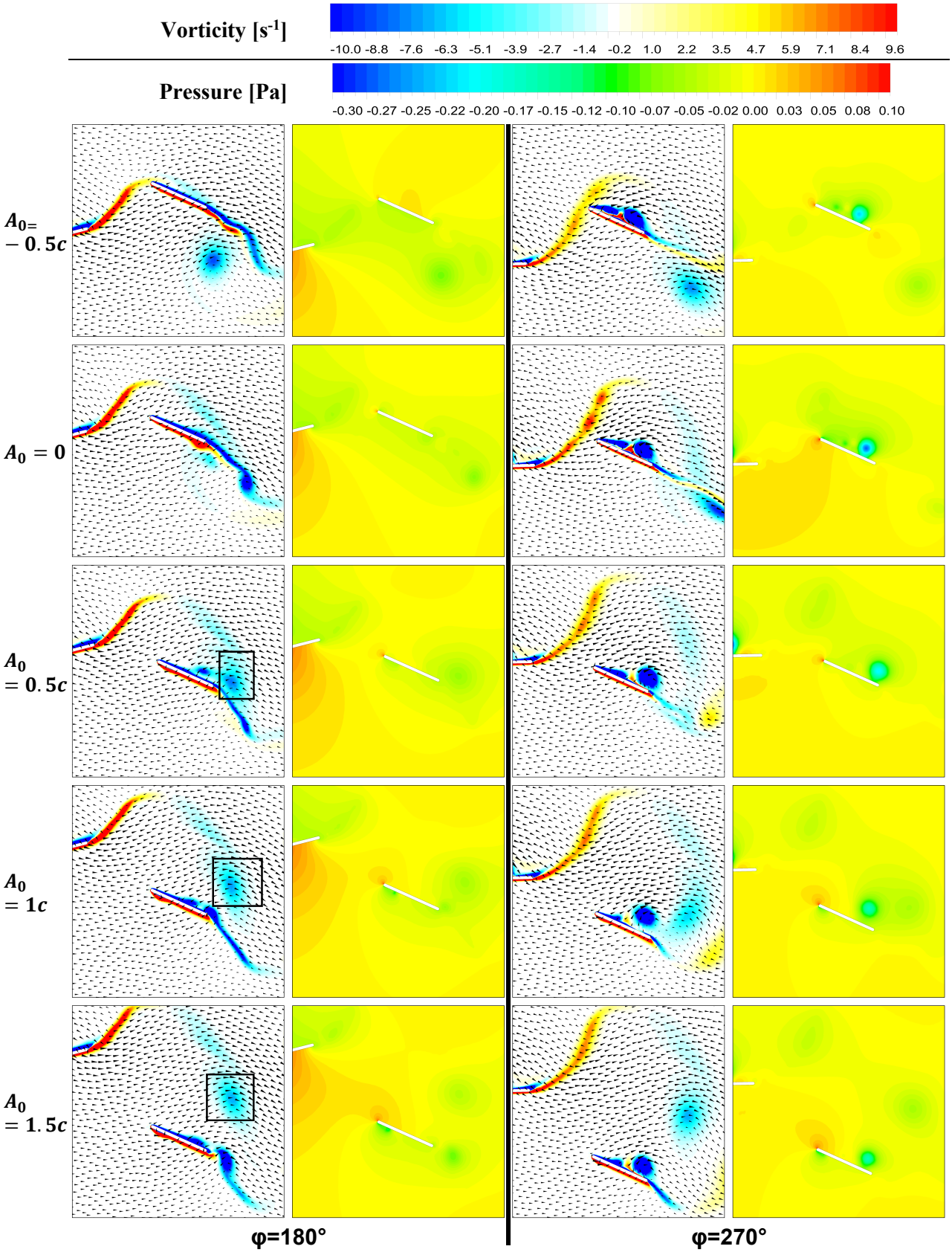

Figure 6.14 Vorticity and pressure contours around the hindwing for φ=180° and φ=270°at t/T=0.75.

From the average thrust coefficient plotted in Figure 6.15, it can be clearly seen that the cases with φ=0° and φ=90° outperform the single wing as well as the results of tandem wing at φ =180° and φ 270° where it was maximized at A_0=0.25c for both cases of φ =0° and φ =90°. Compared with A_0=0c, the tandem wing configuration at φ=180° with A_0=1.5c showed the highest increase with **69%** (See Table 6.2).

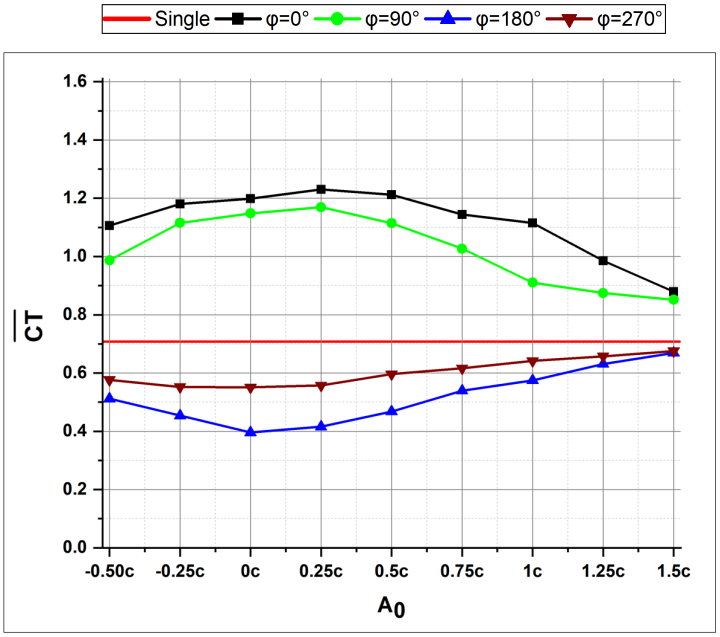

Figure 6.15 Time averaged $\overline{C_T}$ of combined Fore/hind wing

Table 6.2 average thrust coefficient of the best performing tandem wing configuration ($\overline{C_{Tb}}$) compared with the single ($\overline{C_{Ts}}$) case as well as tandem configuration at A_0=0c ($\overline{C_{T\,0c}}$)

Phase difference	**Increase compared with that of a single wing (%)** $\frac{\overline{C_{Lb}} - \overline{C_{Ls}}}{\overline{C_{Ls}}} \times 100$	**Increase compared with Tandem wing at A_0=0c (%)** $\frac{\overline{C_{Lb}} - \overline{C_{L\,0c}}}{\overline{C_{L\,0c}}} \times 100$	**Best performing configuration**
φ=0°	**73.3%**	**2.6%**	A_0=0.25c
φ=90°	**65.2%**	**2%**	A_0=0.25c
φ=180°	**-5.5%**	**69%**	A_0=1.5c
φ=270°	**-4.5%**	**22.5%**	A_0=1.5c

To further quantitatively demonstrate the effect of A_0 and φ on both the lift and thrust generation, the average resultant coefficient of the tandem as well as single wing configurations is plotted in Figure 6.16.

We notice a similar trend between the averages of the resultant and lift coefficients. That is because the thrust force is significantly lower than the lift force.

Compared with a single wing, the case of φ=90° with A_0=0c was **12%** higher.

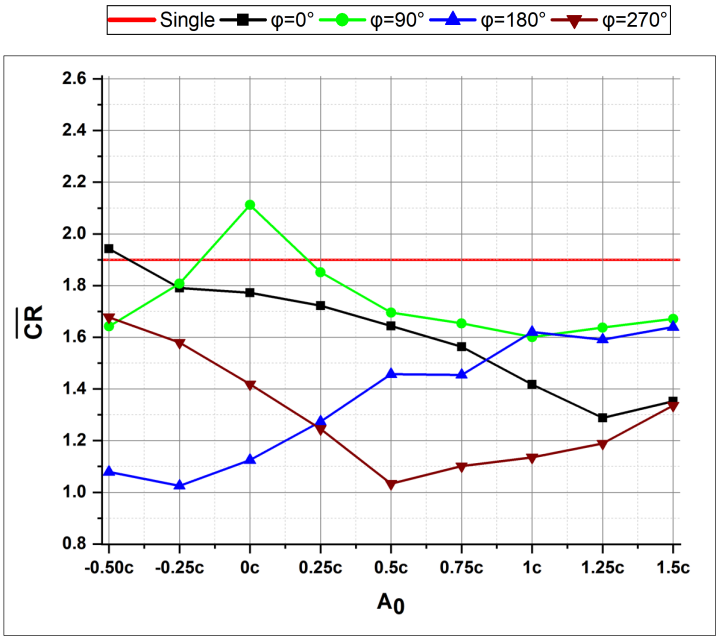

Figure 6.16 Time averaged $\overline{C_R}$ of combined Fore/hind wing.

The time histories of the energy coefficient for both the fore and hind wings are shown in Figure 6.17. The positive energy coefficient represents power output by the system. However, a negative energy coefficient represents power put back to the system and since it is impractical for the wing to regenerate energy, the negative values of the energy coefficient are set to zero.

As the initial position varies, it is noticed that the hindwing at φ=180° had lower power consumption than that of a single wing. While the initial position was decreasing, the energy consumption was decreasing as well.

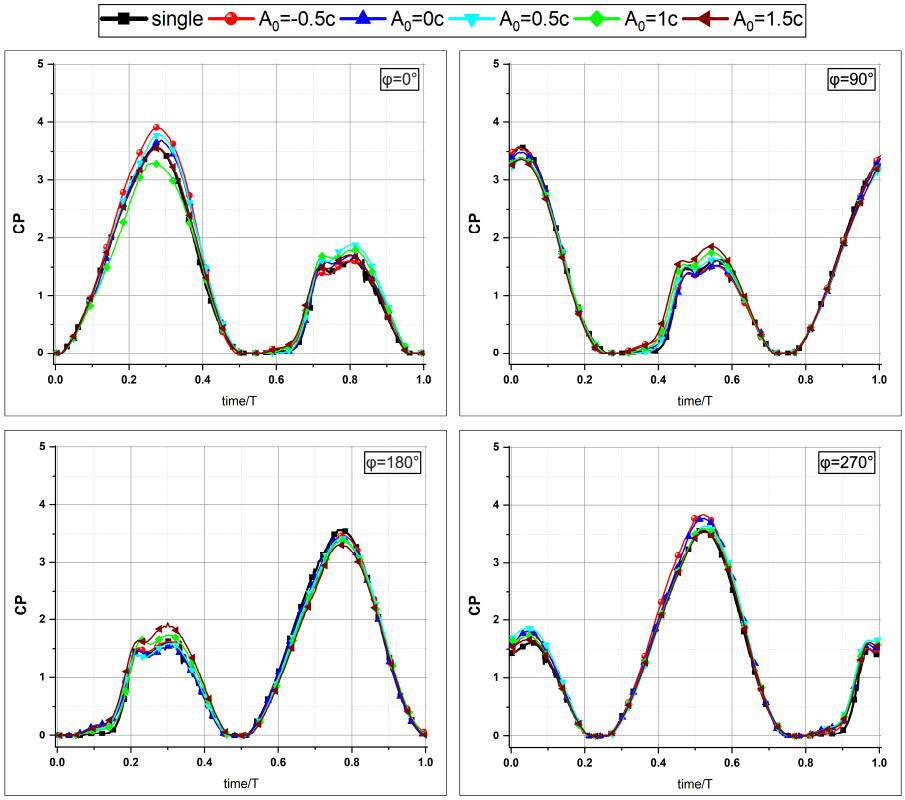

Figure 6.17 Time histories of the power coefficient of the Forewing.

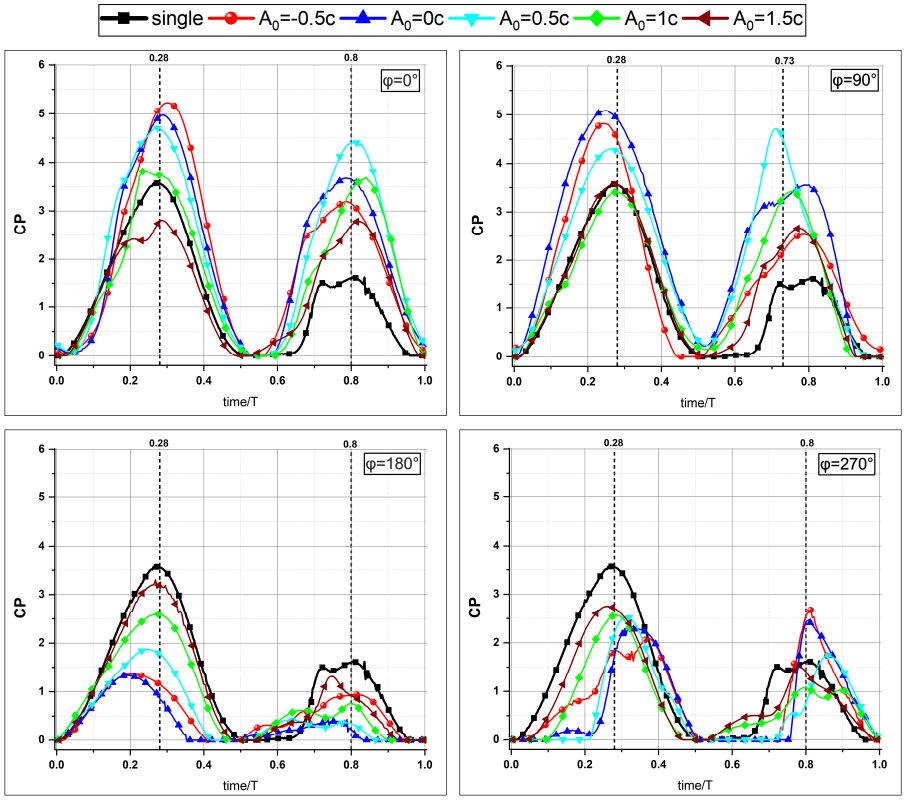

Figure 6.18 Time histories of the power coefficient of the hindwing.

Figure 6.19 shows the variation of the mean energy coefficient at different initial positions. The energy consumption of the tandem wing configuration at φ=0° and φ=90° remained above that of a single wing for all A_0 cases. On the contrary, the energy consumption at φ=180° and φ =270° is lower than that of the single wing for all A_0 cases. This increase of the energy consumption is due the high-pressure area on the upper and lower sides of the hindwing during the upstroke and the downstroke, respectively (see Figure 6.8 and Figure 6.13).

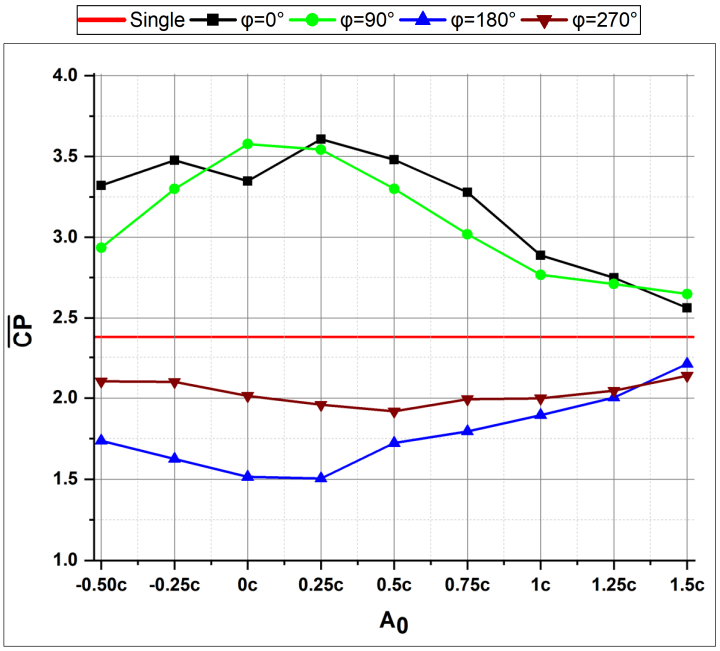

Figure 6.19 Averaged $\overline{C_P}$ of combined Fore/hind wing

The above results suggest that the cases with φ=0° and φ=90° have significantly higher thrust generation. However, these cases also had a higher energy consumption. To see which configuration possesses the highest aerodynamics efficiencies, the variation of the thrust, lift and resultant efficiencies are plotted in Figure 6.20.

It is seen that the propulsive efficiency of tandem configuration at φ =0 and φ = 90° was higher than the isolated wing for all A_0 cases. As for the rest, it was found that η_T was higher only between A_0=0.75c and A_0=1.5c and between A_0=0.5c and A_0=1.5c for the cases of φ= 180° and φ=270°, respectively. This can be seen in Table 6.3 where η_T at φ=0% with A_0=1c showed the maximum increase of **30%** when it is compared with the case of a single wing. Compared with the case of A_0=0c, the case with φ=180° at A_0=1.25c had the maximum increase of **20.4**%.

Although the lift production was low at φ =180° due to the destructive wing-vortex interaction, the lift efficiency was maximized at this phase. This is consistent with the experimental results of Dong and Liang [96] where they also concluded that the destructive interaction increases the efficiency while the instructive interaction increases the efficiency.

As it can be seen in Figure 6.20(b) and (c), the lift and resultant efficiencies follow the same trend. They were both maximized at φ =180° with A_0=0.5c. The lift efficiency with this configuration benefit was found to be as higher as **8.2%** when it is compared with a single wing and **15.2 %** when it is compared with the case of A_0=0c (see Table 6.4).

Table 6.3 Thrust efficiency of the best performing tandem wing configuration (η_{Tb}) compared with the single (η_{Ts}) case as well as tandem configuration at A_0=0c ($\eta_{T\,0c}$)

Phase difference	Increase compared with that of a single wing (%) $\frac{\overline{C_{Lb}} - \overline{C_{Ls}}}{\overline{C_{Ls}}} \times 100$	Increase compared with Tandem wing at A_0=0c (%) $\frac{\overline{C_{Lb}} - \overline{C_{L\,0c}}}{\overline{C_{L\,0c}}} \times 100$	Best performing configuration
φ=0°	**30%**	**7.9%**	A_0=1c
φ=90°	**14.5%**	**6%**	A_0=0.75c
φ=180°	**6%**	**20.4%**	A_0=1.25c
φ=270°	**8.2%**	**17.5%**	A_0=1.25c

Table 6.4 Lift efficiency of the best performing tandem wing configuration (η_{Lb}) compared with the single (η_{Ls}) case as well as tandem configuration at A_0=0c ($\eta_{L\,0c}$)

Phase difference	Increase compared with that of a single wing (%) $\frac{\overline{C_{Lb}} - \overline{C_{Ls}}}{\overline{C_{Ls}}} \times 100$	Increase compared with Tandem wing at A_0=0c (%) $\frac{\overline{C_{Lb}} - \overline{C_{L\,0c}}}{\overline{C_{L\,0c}}} \times 100$	Best performing configuration
φ=0°	**-35%**	**23.3%**	A_0= -0.5c
φ=90°	**-26.6%**	**9.5%**	A_0=1.5c
φ=180°	**8.2%**	**15.2%**	A_0=0.5c
φ=270°	**1.3%**	**15.4%**	A_0= -0.5c

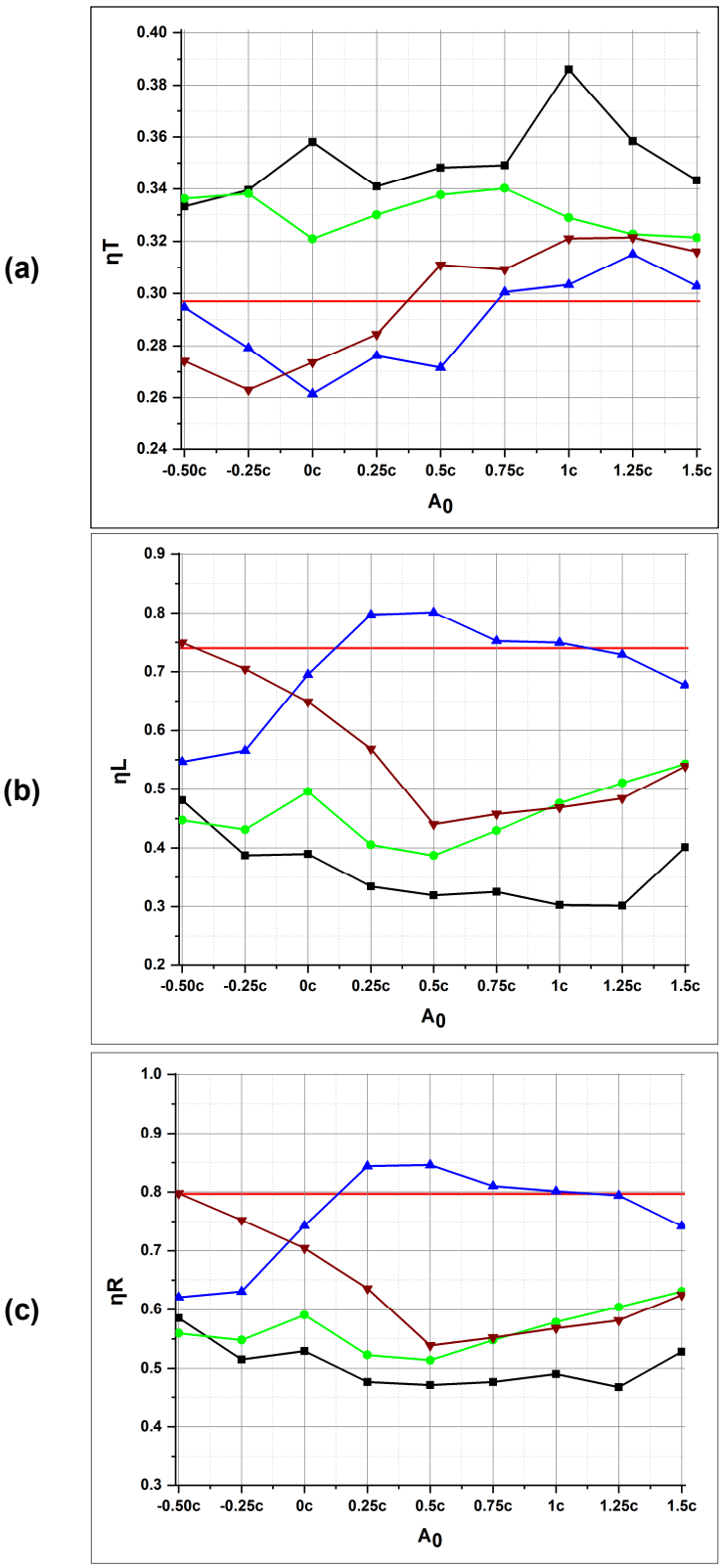

Figure 6.20 Variation of $\eta_T, \eta_L \; and \; \eta_R$, (a) thrust efficiency, (b): Lift efficiency, (c) resultant efficiency

6.4.2 Effect of frequency

In this section, we investigate the effects of the asymmetry of the flapping frequency on the flow around tandem wing configuration. Three cases were chosen is this study. The initial position was fixed at $A_0 = 0°$ and the phase difference at $\varphi = 0°$.

The variation of flapping frequency factor for ε the both wings are described in Table 6.5.

Table 6.5 variation of the flapping frequency factor ε.

	Configuration		**ε** of the Forewing	**ε** of the Hindwing
symmetrical			**1**	**1**
Case 1	Configuration 1	Slow Forewing Fast Hindwing	**2/3**	**4/3**
	Configuration 2	Fast Forewing Slow Hindwing	**4/3**	**2/3**
Case 2	Configuration 1	Slow Forewing Fast Hindwing	**4/5**	**6/5**
	Configuration 2	Fast Forewing Slow Hindwing	**6/5**	**4/5**
Case 3	Configuration 1	Slow Forewing Fast Hindwing	**6/7**	**8/7**
	Configuration 2	Fast Forewing Slow Hindwing	**8/7**	**6/7**

For the case 1(Configuration 1), within the same period of time, the forewing and the hindwing complete one and two strokes, respectively. For the case 2 (Configuration 1), within the same period of time, the forewing and the hindwing complete two and three strokes, respectively. For the case 3 (Configuration 1), during the same period of time, the forewing and the hindwing complete three and four strokes, respectively.

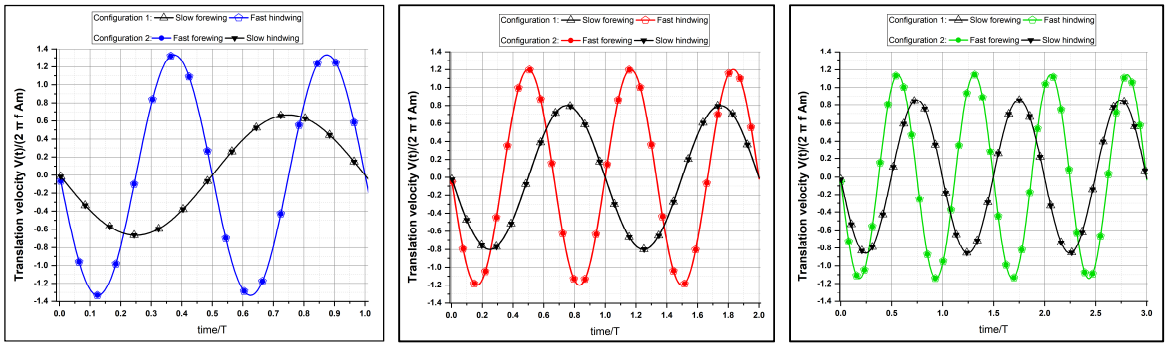

Case 1 **Case 2** **Case 3**

Figure 6.21 Time histories of the translation velocity for the three cases.

The thrust, lift and resultant coefficients for the combined wings were calculated using :

$$C_T = -\frac{\varepsilon F_{Df} + \varepsilon F_{Dh}}{0.5\,\rho {U_0}^2 (c_f + c_h)} \tag{6.5}$$

$$C_L = \frac{\varepsilon F_{Lf} + \varepsilon F_{Lh}}{0.5\,\rho {U_0}^2 (c_f + c_h)} \tag{6.6}$$

$$C_R = \frac{\sqrt{\left(\varepsilon F_{Df} + \varepsilon F_{Dh}\right)^2 + \left(\varepsilon F_{Lf} + \varepsilon F_{Lh}\right)^2}}{0.5\,\rho {U_0}^2 (c_f + c_h)} \tag{6.7}$$

Figure 6.22 and Figure 6.23 compare the thrust and lift coefficients for both the fore and hind wings for each case chosen in this study. The horizontal lines represent the average values of the thrust and lift at each case.

The continued curves represent the wings that flap with lower frequencies while the dashed curves represent the wings that flap with higher frequencies.

Nine time instants were chosen for this analysis:

For case 1: t(a)=0.13T, t(b)=0.25T, t(c)=0.88T

For case 2: t(d)=0.3T, t(e)=0.85T, t(f)=1.85T

For case 3: t(g)=0.75T, t(h)=1.7T, t(i)=2.85T

It is seen that in all three cases the slow hindwing benefits in term of thrust production from the higher frequency of the forewing. However, the slow forewing had negative effect on the thrust of the fast hindwing (configuration1).

As for the lift production, it is observed that in configuration 1 the forewing produces more lift than the hindwing despite that it has lower flapping frequency. This

concludes that the when the forewing flaps with lower frequency than the hindwing an undesirable effect on the lift production of the hindwing is resulted.

Moreover, it is noticed that although the forewing (configuration1) and hindwing (configuration 2) flap with the same frequency, the hindwing had an additional peak in both the thrust or lift coefficient in all three cases

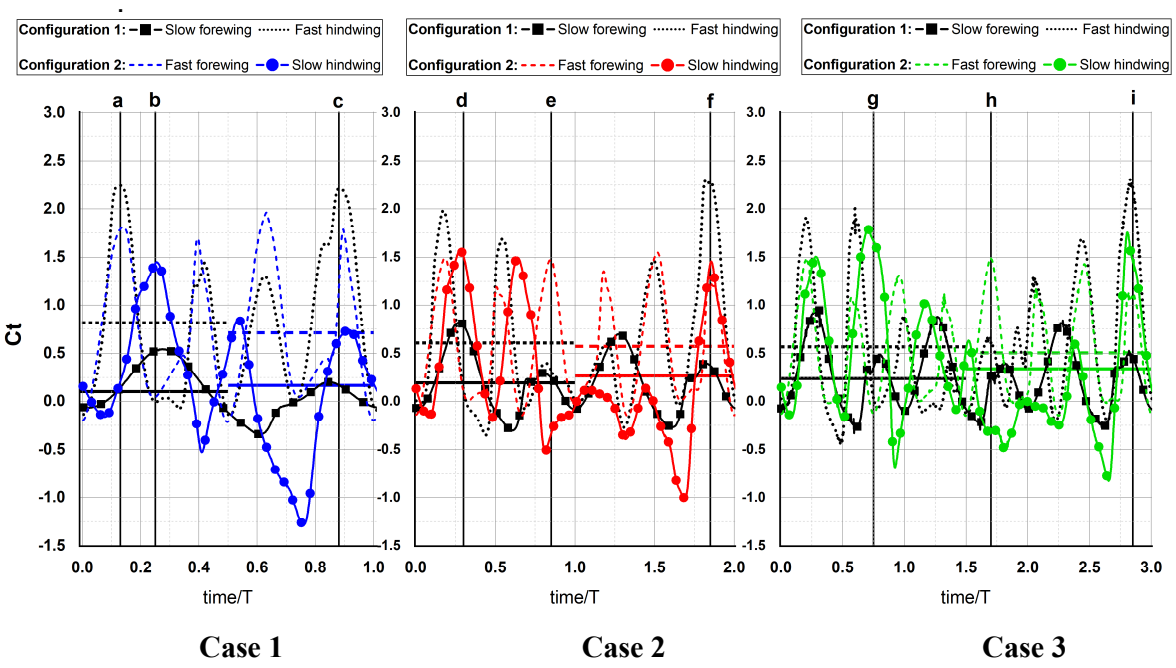

Figure 6.22 Time histories of the thrust coefficient C_T of the three cases.

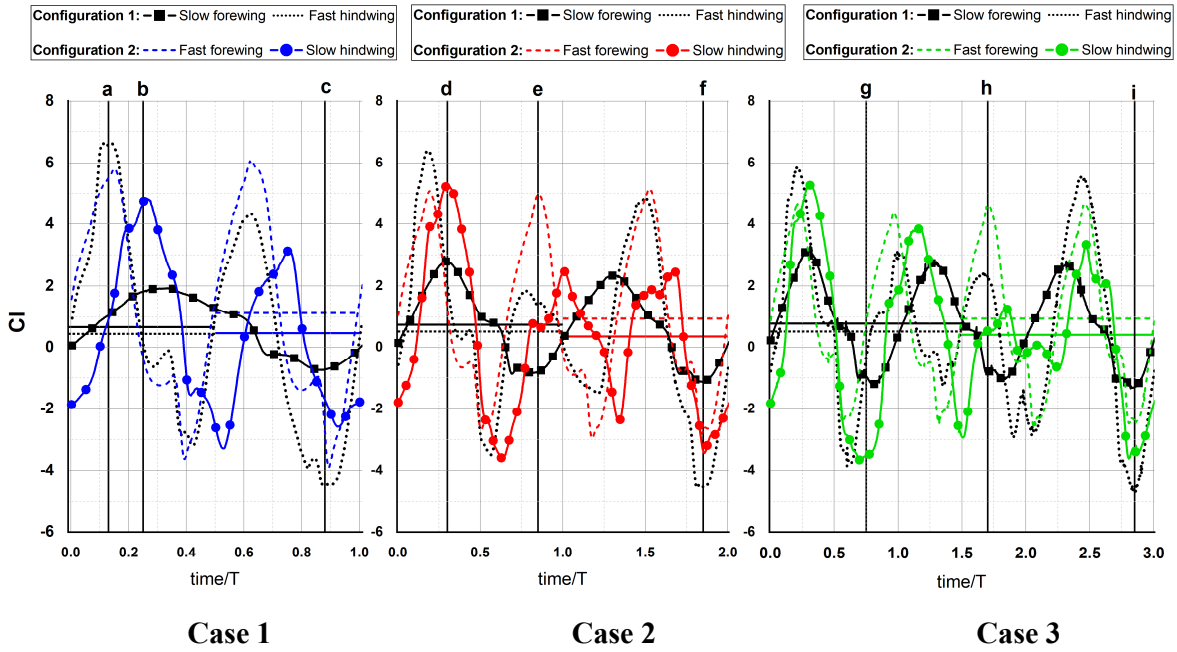

Figure 6.23 Time histories of the lift coefficient C_L of the three cases.

Figure 6.24-6.26 represent the vorticity contours for all cases chosen in this study at different instants.

Case 1:

At t(a), we notice a similar flow patter around the hindwing of the configuration 1 and the forewing of configuration 2 with slight flow acceleration in configuration 1 (as the two headed arrow indicates in Figure 6.24(a)). This explains the similarity of the lift and thrust trend around t(a), which is due to the absence of vortex interaction between the tandem wings around this instance.

At t(b), we notice in configuration 2 that the CW vortex shed from the forewing induces the flow on the lower side of the hindwing (as it is indicated by red rectangle on Figure 6.24) . This led to a higher thrust peak compared with the forewing of configuration 1. Moreover, we notice that the size of the LEV on the hindwing of configuration 2 is significantly larger than the forewing of configuration 1 (as the two-headed arrow indicates in Figure 6.24(b)). This is because the CCW shedding vortex from the forewing accelerates the growth of the LEV on the hindwing. This explains the larger lift peak observed in configuration 2 (see Figure 6.23 (b)).

At t(c), the shed LEV from the forewing of configuration 1 merges with the newly formed LEV on the hindwing to create larger LEV (as the two-headed arrow indicates in Figure 6.24(c)). This resulted in a significant enhancement in the thrust generation (see Figure 22(c)). The absence of wing wake interaction during the upstroke of the forewing in configuration 1 (as the green two-headed arrow indicates in Figure 6.24(c)) had a significant benefit on the thrust generation. However, it resulted in larger negative lift peak (see Figure 6.22 and Figure 6.23 at t (c)).

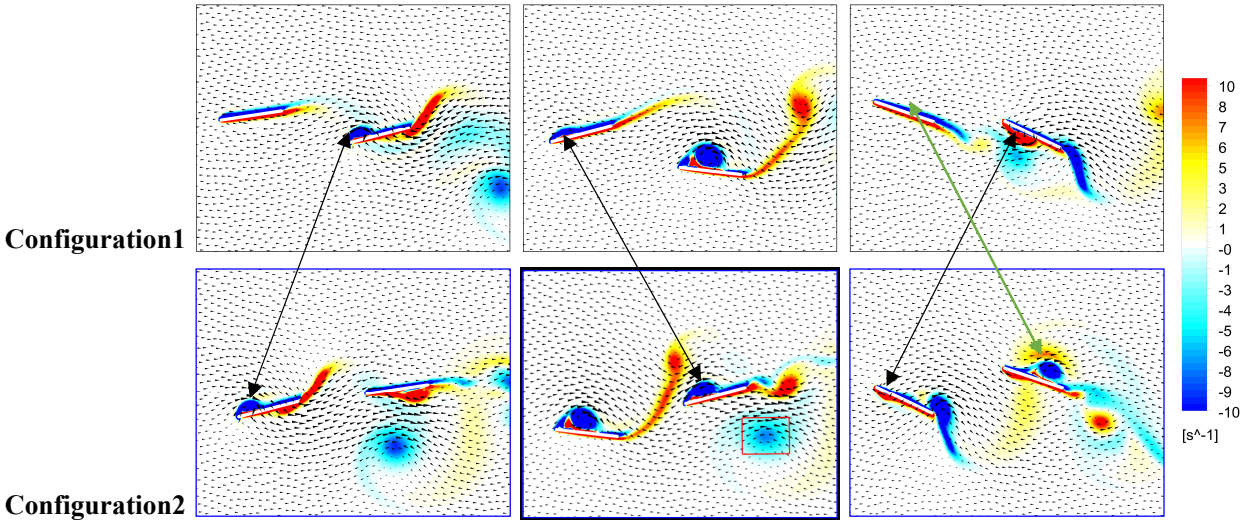

Figure 6.24 Vorticity contours of the Case 1 and Case 4 at t/T= 0.12, t/T=0.25 and t/T=0.88.

Case 2:

At t(d), we notice from the vorticity contours that the elongated shed TEV of the forewing in configuration 2 (labelled with black rectangle in Figure 6.25 (d)) accelerates and strengthens the LEV formed on the hindwing. This resulted in a significant high lift and thrust peaks compared with the forewing in configuration 1 (see Figure 6.22 and Figure 6.23 (d)).

At t(e), we notice that the formed LEV on the forewing in configuration 2 is much stronger than the formed LEV on the hindwing in configuration 1 (as the two headed arrow indicates in Figure 6.25(e)). Moreover, the CW shed vortex at the lower side of the hindwing in configuration 1(labelled with black rectangle in Figure 6.25 (e)) induces the downwash on the underside of the hindwing. This resulted in significant drop of the production of thrust and lift as Figure 6.22 (e) and Figure 6.23 (e) indicate.

At t(f), the shed LEV from the forewing in configuration1 (see green rectangle in Figure 6.25 (f)), had favorable influence on the thrust generation by increasing the size of the CCW LEV on the lower side of the hindwing (see Figure 6.22 (f)). However, that had negative influence on the lift generation by increasing the negative life coefficient (see Figure 6.23 (f)).

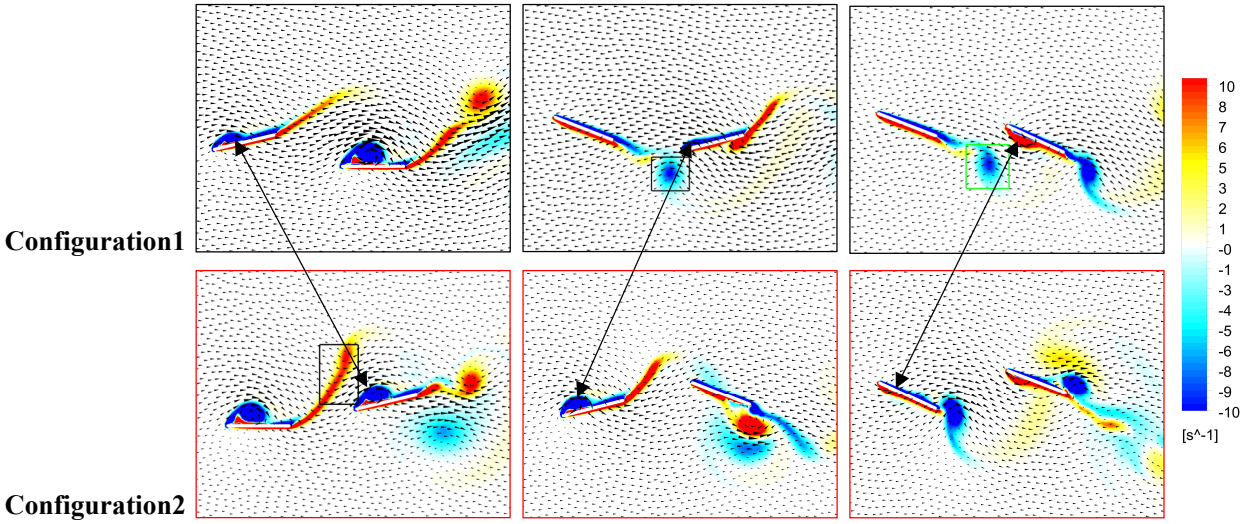

Figure 6.25 Vorticity contours of the Case 2 and Case 5 at t/T= 0.3, t/T=0.85 and t/T=1.85.

Case 3:

At t(g), we notice a large CCW LEV on the hindwing of the configuration2 which was a result of the induced forewash created by the shed LEV from the forewing. However, in configuration 1 the LEV was not present on the forewing (as the two-headed arrow indicates in Figure 6.26(g)). The presence of the LEV on the underside of the wing creates a suction zone, which was in favor of the thrust generation as Figure 6.22(g) shows. However, this had a negative effect on the lift generation, where we notice a significantly higher negative peak.

We notice that at t(h), the forewing in configuration 2 generates more thrust and lift than the hindwing in configuration1 (see Figure 6.22 and Figure 6.23 (h)). During the downstroke, the hindwing in configuration 1 passes through the destructive elongated TEV shed from the forewing which resulted in smaller LEV compared with the LEV on the forewing in configuration 2 (as the two headed arrow indicates in Figure 6.26(g)).

At t(i), the induced flow created by the forewing increased the size of the LEV of the hindwing in both configurations (see Figure 6.26 (i)) which resulted in significant higher thrust generation.

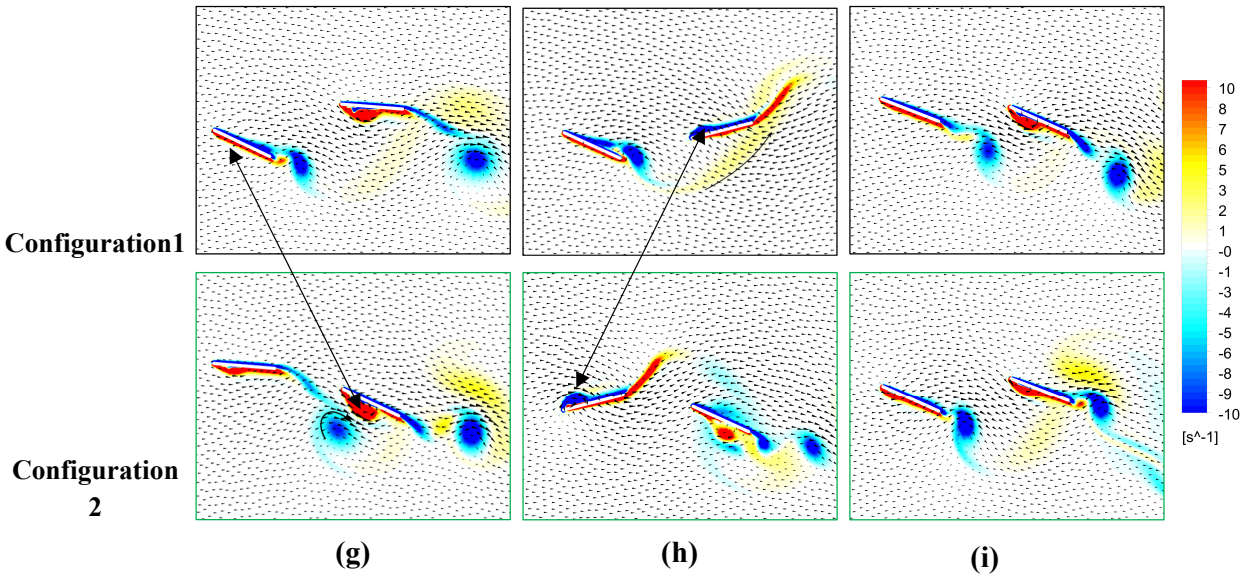

Figure 6.26 Vorticity contours of the Case 3 and Case 6 at t/T= 0.75, t/T=1.7 and t/T=2.85.

Figure 6.27 shows the transient energy coefficient for both the fore and hind wings with the negative values set to zero.

In all three cases, the power consumption of the hindwing is slightly higher than the forewing. Which indicates that hindwing does not benefit in terms of energy consumption from the flow structure left from the forewing.

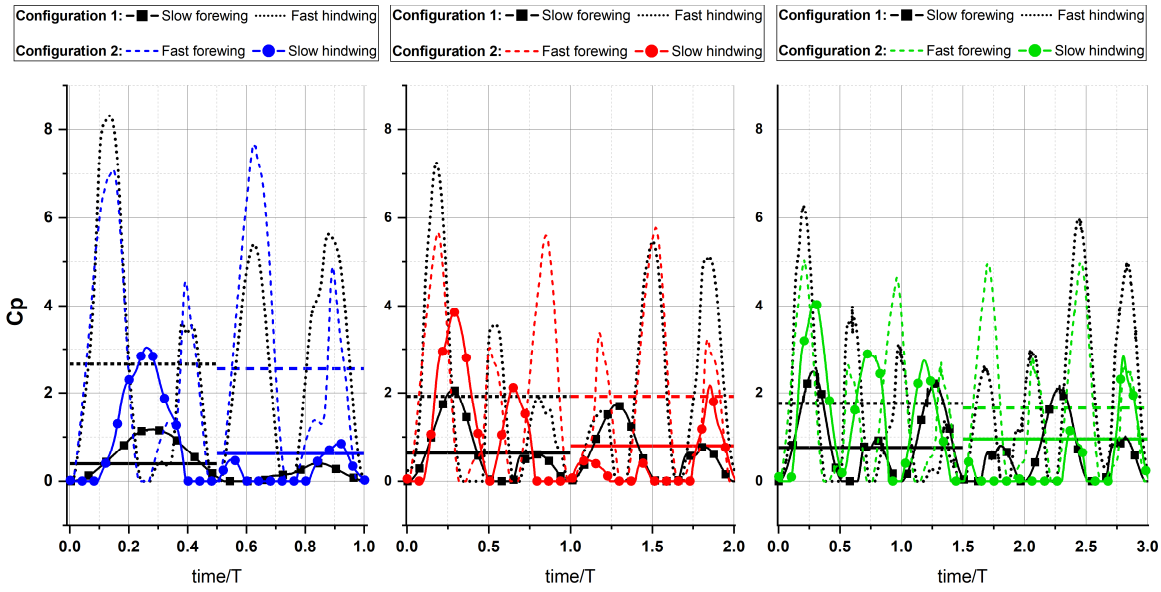

Figure 6.27 Time histories of the energy coefficient C_P of the three cases.

The propulsive force generated with a symmetrical stroke remained higher than all cases studied (see Figure 6.28).

The lift production generated with configuration 2 remained higher than the symmetrical stroke as well as configuration 1 in all cases, which concludes that the slow hindwing benefits greatly from the strong vortices that are shed from the forewing that flaps with higher frequency. However, when the forewing flaps with slower frequency, it creates a sort of an obstacle on the hindwing to rely on the drag to generate lift force.

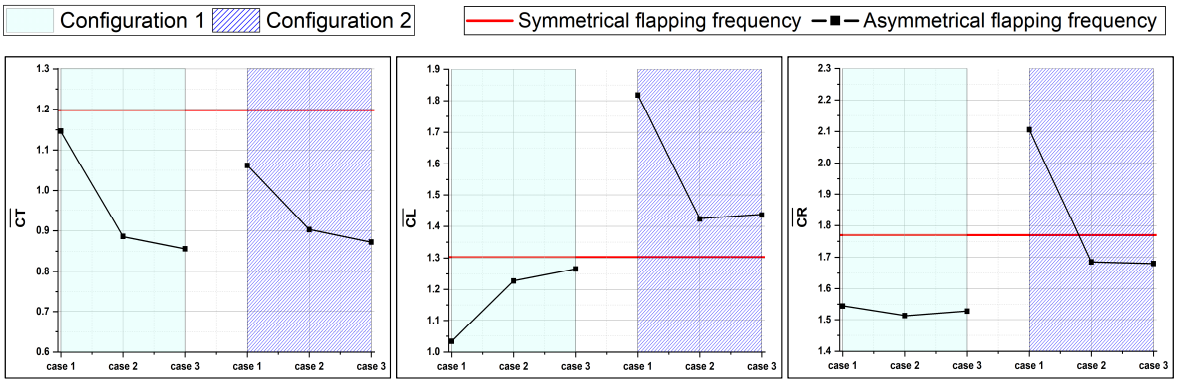

(a) **(b)** **(c)**

Figure 6.28 Time average of C_T, C_L and C_R for all cases studied compared with the symmetrical case, (a): average thrust coefficient, (b): average lift coefficient and (c): average resultant coefficient

From Figure 6.29, we notice that the case 3 with configuration 2 outperformed all the cases studied in term of lift and resultant efficiencies including the symmetrical stroke. However, the symmetrical stroke had the highest thrust efficiency. Compared with the symmetrical stroke, the case 3 (configuration 2) had an increase of **32%** and **15%** in lift and resultant efficiencies, respectively.

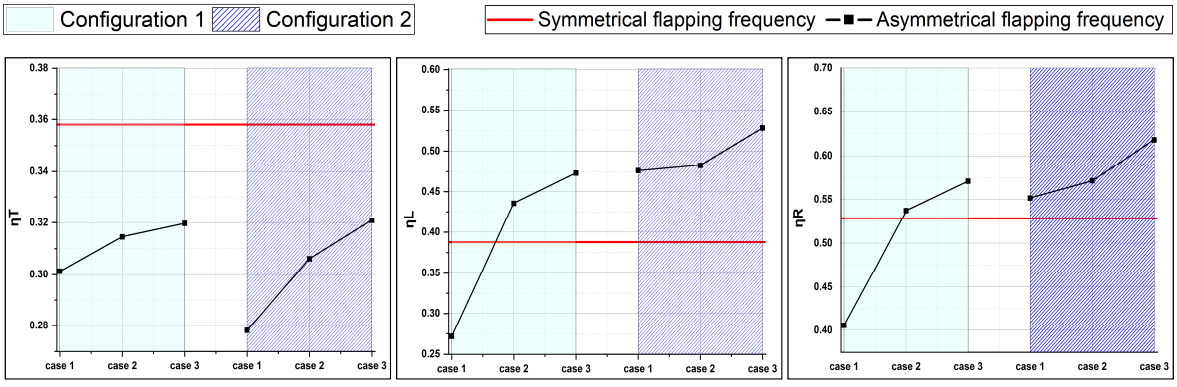

(a) **(b)** **(c)**

Figure 6.29 Variation of η_T, η_L and η_R, (a) thrust efficiency, (b): Lift efficiency, (c) resultant efficiency

6.5 Conclusion

In this chapter, the effects of the initial position and the asymmetry in flapping frequency on the aerodynamics of 2D flapping wings in tandem configuration has been investigated. The Reynolds number was fixed at Re=5000. Both wings flap in symmetrical harmonic pitching and plunging along the horizontal direction motions.

The results from this study suggest that the aerodynamic forces and efficiencies are heavily affected by the two parameters chosen in this study.

The results of the effects of the initial position show that although the single wing had the highest thrust, lift and resultant coefficients compared with the tandem wing configuration at φ=180°, the efficiency of these coefficient for a single wing was lower than most cases of tandem wing arrangement as the initial position varies. This was due to the significant decrease of the energy consumption in the tandem wing configuration where the case of the highest lift and resultant efficiencies (A_0 =0.75c) showed a 28% decrease in the power consumption compared to the single wing case. The cases with A_0 =0.75c and A_0 =1c had simultaneously higher thrust, lift and resultant efficiencies than the single wing case.

In the second part, the results suggest that the lift and resultant production of configuration 2 remained higher than symmetrical stroke as well as configuration 1 in almost all cases, which concludes that the slow hindwing benefits incredibly from the strong vortices that were shed from the forewing that flaps with higher frequency. As for the aerodynamic efficiency of the asymmetrical flapping frequency, it was found that the symmetrical stroke had the highest thrust efficiency. However, all cases of the configuration 2 where the forewing flaps with higher frequency than the hindwing had higher lift efficiency. The case 3 with configuration 2 outperformed all the other cases including the symmetrical stroke in both lift and resultant efficiencies.

Concluding remarks and future work

Concluding remarks

In this thesis, we have investigated the effects on multiple parameters on the aerodynamic performance of single and tandem wing configurations. The present numerical results were compared with several previous studies. The present results showed a good agreement with the results found in the literature.

The aerodynamic investigation was consisted of three parts. First, we studied the effects of the ground on the aerodynamics by using several distances from the ground to the center of the airfoil at Reynolds number of 100. The delayed-stall mechanism associated with the leading edge vortex and the rapid pitch-up mechanisms were identified in both hovering modes. However, only for the “normal” hovering mode, the wake-capturing mechanism was identified at the beginning of the stroke.

The influence of the ground affected the two hovering modes differently. The cushion effect combined with large-scale Leading edge vortex increases the lift production drastically when the airfoil is located near the ground. For the “water treading” mode, the closer the airfoil gets to the ground the higher the lift force, energy consumption and the flight efficiency are produced. However, for the “normal” mode, the maximum lift production was also found when the airfoil is situated closer to the ground. However, unlike the case of the “water treading” mode, a significant drop in the lift production in the “normal” mode, was located between L= 1.5c and L=3.5c (the force reduction regime).

Second, the effects of the asymmetry in flapping duration, wing spacing and phase difference on the thrust and lift generation as well as energy consumption and the flow structure at Reynolds number of 157 were investigated. Three flight mechanisms used by naturel flyers were identified in this analysis, the wake capturing, fast pitching rotation and rapid acceleration. It is found that depending on when and how the hindwing interacts with the vortices created by the forewing motion will either increase or decrease the aerodynamic forces. For instance, when the hindwing avoids the destructive vortices that are created from the forewing, we notice as significant increase in the thrust generation. Furthermore, the absence of destructive vortex-vortex interaction on the hindwing resulted in higher lift generation. As for the energy

consumption, it was found that the case of symmetrical stroke results in minimal energy consumption, where the lowest energy consumption was found in the case of counter phase flap.

The thrust production and efficiency with faster upstroke was higher than the symmetrical stoke in all cases studied. However, the lift production and efficiency was maximized with faster downstroke instead. This concludes that the asymmetry in flapping duration has more importance than the wing spacing and phase difference.

Finally, we investigated the effects of the initial position and the asymmetry in flapping frequency on the aerodynamics of 2D flat plate wings in tandem configuration. The Reynolds number was fixed at 5000. The results from this study suggest the aerodynamic forces and efficiencies are heavily affected by the two parameters chosen in this study.

The results of the effects of the initial position show that although the single wing has the highest thrust, lift and resultant coefficients compared with the tandem wing configuration at $\varphi=180°$, the efficiency of these coefficients for a single wing was lower than most cases of tandem wing as the initial position varies. As for the effects of the asymmetry in flapping frequency, the results show that when the forewing flaps with higher frequency, the lift and resultant forces remained higher than symmetrical stroke as well as configuration 1 in almost all cases. This conclude that the slow hindwing benefits greatly from the strong vortices that are shed from the forewing that flaps with higher frequency. However when the forewing flaps with slower frequency it creates a sort of an obstacle on the hindwing that relies on drag to generate lift force.

Future work:

1- Hovering modes

In the first case studied in this thesis, only two hovering modes were considered for comparison. However, there are several other hovering modes that can provide a better insight into the effects of the ground on the aerodynamics, such as:

- The advanced and delayed rotations
- Figure-of-O flapping trajectory
- Figure-of-eight flapping trajectory
- Figure-of-U flapping trajectory

2- Corrugated tandem wing configuration in forward flight

The effects of the wing spacing, phase difference and the downstroke ratio on a corrugated airfoil instead of an elliptic one is of high importance since corrugated wings resemble to the dragonfly wing shape. This probably will give a better understanding of the dragonflys' flight characteristics.

3- Wing aeroelasticity

All the results presented in this dissertation have been obtained assuming that the wing is rigid and the flow is laminar. Though these assumptions are sufficient for conceptual and preliminary design phases of MAVs, a more sophisticated physical model taking into account aeroelasticity effect should be used at the final phase of the MAV design process.

NOMENCLATURE

A(t)	:	Instantaneous position of tandem airfoils [m]
A_0	:	Initial position of tandem airfoils [m]
C	:	Chord length [m]
C_l	:	Lift coefficient [-]
$\overline{C_l}$	:	Averaged lift coefficient [-]
C_R	:	Resultant coefficient [-]
$\overline{C_R}$	:	Averaged Resultant coefficient [-]
C_T	:	Thrust coefficient [-]
$\overline{C_T}$	:	Averaged Thrust coefficient [-]
C_p	:	Energy coefficient [-]
$\overline{C_p}$	:	Averaged energy coefficient [-]
D	:	Ground clearance [m]
dt	:	Time step [s]
f	:	Flapping frequency [Hz]
F_{flap}	:	Flapping force [N]
F_D	:	Drag force [N]
F_L	:	Lift force [N]
F_R	:	Resultant force [N]
h_a	:	Flapping amplitude of the airfoil in hovering mode [m]
h(t)	:	Instantaneous position of a flapping airfoil in hovering mode [m]
J	:	Advance ratio [-]
k	:	Reduced frequency [-]
p	:	Static pressure [Pa]
P(t)	:	Instantaneous energy consumption [Watt]
M_a	:	Rotational moment [N m]
Re	:	Reynolds number [-]
R_{ao}	:	Vector from the origin to the centre of the airfoil which [m]
T	:	Period of one flapping cycle [s]
t	:	Time [s]
u,v,w	:	Cartesian velocity components [m/s]

x,y,z : Cartesian coordinates [m]

U_{ref}: Reference velocity [m/s]

$V(t)$: Instantaneous translation velocity of a flapping airfoil [m/s]

GREEK SYMBOLS

$\omega(t)$: Instantaneous rotational velocity of a flapping airfoil [rad/s]

Δt: The time step [s]

Δx : Smallest size in the mesh [m]

$\alpha(t)$: Instantaneous Angle of attack [deg]

α_0: Initial angle of attack [deg]

α_a: Pitching angle amplitude [deg]

φ: Phase difference between flapping and pitching motion [deg]

υ: Kinematic viscosity of the fluid [$m^2\ s^{-1}$]

μ: Dynamic viscosity of the fluid [Kg/m.s]

ρ: Density [Kg/m^3]

ξ : Ratio of downstroke duration to flapping period [-]

η_t: Lift efficiency [-]

SUBSCRIPTS

CFL: Courant-Friedrichs-Lewy number

HTOL: horizontal take off landing

LEV: Leading Edge Vortex

MAV: Micro Air Vehicle

NAV: Nano air vehicle

PAV: Pico air vehicle

SD: Smart dust

UAV: Unmanned air vehicle

μUAV: Micro unmanned air vehicle

VTOL: vertical take-off landing

References

[1] V. Tucker, “Energetic cost of locomotion in animals,” *Comparative biochemistry and physiology,* vol. 34, pp. 841-846, 1970.

[2] A. Cavoukian, Privacy and Drones: Unmanned Aerial Vehicles, Ontario: Information and Privacy Commissioner, 2012.

[3] S. Gupta, M. Ghonge and P. Jaw, “Review of unmanned aircraft system (UAS),” *International Journal of Advanced Research in Computer Engineering & Technology,* vol. 2, no. 4, 2013.

[4] h. Snow, “MarineTimes,” Your Marine Corps, 11 12 2016. [Online]. Available: https://www.marinecorpstimes.com/news/your-marine-corps/2019/03/20/here-are-some-of-the-tactical-drones-the-corps-wants-in-2020/. [Accessed 20 01 2020].

[5] L. Brooke-Holland, “Unmanned Aerial Vehicles (drones): An Introduction,” House of Commons Library, UK, 2012.

[6] A. Arjomandi, S. Agostino, M. Mammone, M. Nelson and T. Zhou, “Classification of Unmanned Aerial Vehicle,” University of, Adelaide, 2006.

[7] B. Zakora and A. Molodchick, “Classification of UAV (Unmanned Aerial Vehicle),,” [Online]. Available: ⟨http://read.meil.pw.pl/abstracts/StudentAbstract_Zakora_. [Accessed january 2014].

[8] “TAdviser,” TAdviser, 07 09 2018. [Online]. Available: http://tadviser.com/index.php/Article:Smart_dust. [Accessed 20 01 2020].

[9] M. Hassanalian and A. Abdelkefi, “Classifications, applications, and design challenges of drones: A review,” *Progress in Aerospace Sciences,* vol. 91, pp. 99-131, 2017.

[10] C. Galinski and R. Żbikowski, “Materials challenges in the design of an insect-like flapping wing mechanism based on a four-bar linkage,” *Materials & Design,* vol. 28, pp. 783-796, 2007.

[11] M. Hassanalian and A. Abdelkefi, “A novel methodology for wing sizing of bio-inspired flapping wing micro air vehicles: theory and prototype,” *Acta Mechanica,* vol. 228, 2016.

[12] “SCRIBD,” 2010. [Online]. Available: https://www.scribd.com/document/38262061/Mission-on-and-Rules-IMAV-2010. [Accessed 2019].

[13] T. Ward, C. Fearday, E. Salami and N. Soin, “A bibliometric review of progress in micro air vehicle research,” *International Journal of Micro Air Vehicles,* vol. 9.

[14] M. Hassanalian, H. Khaki and M. Khosrawi, “A new method for design of fixed wing micro air vehicle,” *Journal of Aerospace Engineering,* vol. 229, 2014.

[15] G. Cai, J. Dias and L. Seneviratne, “A Survey of Small-Scale Unmanned Aerial Vehicles: Recent Advances and Future Development Trends,” *Unmanned Systems,* vol. 02, pp. 175-199, 2014.

[16] F. Bohorquez, P. Samuel, J. Sirohi, D. Pines, L. Rudd and R. Perel, “Design, Analysis and Hover Performance of a Rotary Wing Micro Air Vehicle,” *Journal of the American Helicopter Society,* vol. 48, pp. 80-90, 2003.

[17] “SingularityHub,” [Online]. Available: https://singularityhub.com/2010/09/17/quadrotor-robot-with-open-source-computer-vision-flies-itself-video/. [Accessed 10 2019].

[18] W. Han, Y. Lei and X. Zhou, “Application of unmanned aerial vehicle survey in power grid engineering construction,” *Electr. Power Surv,* vol. 3, no. 019, 2010.

[19] F. Charavgis, “TUDelft,” 16 02 2016. [Online]. Available: http://resolver.tudelft.nl/uuid:0191e063-648a-4dae-818f-72637bcd456d. [Accessed 10 2019].

[20] G. Decroon, M. Percin, B. Remes, R. Ruijsink and C. De Wagter, The delfly: Design, aerodynamics, and artificial intelligence of a flapping wing robot, New York: Springer, 2015.

[21] M. Hassanalian and A. Abdelkefi, “Methodologies for weight estimation of fixed and flapping wing micro air vehicles,” *Meccanica,* 2016.

[22] K. Jones, C. Bradshaw, J. Papadopoulos and M. Platzer, “Bio-inspired design of flapping-wing micro air vehicles,” *The Aeronautical Journal,* vol. 109, pp. 385-393, 2005.

[23] L. Petricca, P. Ohlckers and C. Grinde, “Micro- and Nano-Air Vehicles: State of the Art,” *International Journal of Aerospace Engineering,* 2011.

[24] M. Keennon, K. Klingebiel and H. Won, “Development of the Nano Hummingbird: A Tailless Flapping Wing Micro Air Vehicle,” Nashville, Tennessee, 2012.

[25] “Autonomous Flying Microrobots (RoboBees),” [Online]. Available: https://wyss.harvard.edu/technology/autonomous-flying-microrobots-robobees/. [Accessed 10 2019].

[26] “FLIR,” [Online]. Available: https://www.flir.com/products/black-hornet-prs/. [Accessed 10 2019].

[27] E. Ulrich, D. Pines and J. Humbert, “From falling to flying: The path to powered flight of a robotic samara nano air vehicle,” *Bioinspiration & biomimetics,* vol. 5, p. 045009, 2010.

[28] W. Shyy, M. Berg and D. Ljungqvist, “Flapping and Flexible Wings for Biological and Micro Air Vehicles,” *Progress in Aerospace Sciences,* vol. 35, pp. 455-505, 1999.

[29] D. E. Alexander, Nature’s Flyers, Baltimore/London: University Press, 2002.

[30] T. Weis-Fogh, “Quick estimates of flight fitness in hovering animals, including novel mechanisms for lift production,” *Journal of Experimental Biology,* vol. 59, pp. 169-230 , 1973.

[31] U. M. Norberg, Vertebrate Flight, Berlin: Springer-Verlag, 1990.

[32] A. Azuma, The Biokinetics of Flying and Swimming, Tokyo: Springer-Verlag, 1992.

[33] W. Shyy, Y. Lian, J. Tang, D. Viieru and H. Liu, “Aerodynamics of Low Reynolds Number Flyers,” *Aerodynamics Of Low Reynolds Number Flyers,* 2008.

[34] H. Tennekens, The simple science of flight: From insects to jumbojets, London, England: The MIT Press, 1996.

[35] E. Gowree, C. Jagadeesh, E. Talboys, C. Lagemann and C. Brücker, “Vortices enable the complex aerobatics of peregrine falcons,” *Communications Biology,* vol. 1, 2018.

[36] S. Dhawan, Bird flight, Bangalore: Springer India, 1991.

[37] M. Ruckman. [Online]. Available: https://www.fotocommunity.com/photo/galapagos-hawk-take-off-max-ruckman/23541196.

[38] [Online]. Available: https://animals.desktopnexus.com/get/2468029/?t=ccsuom4anctjomegs7ap2kvk055d97bc26387cd.

[39] C. P. Ellington, Vortices and Hovering Flight, Wiesbaden: Franz Steiner, 1980, pp. 64-101.

[40] C. P. Ellington, “The Aerodynamics of Hovering Insect Flight. IV. Aeorodynamic Mechanisms,” *Philosophical Transactions of The Royal Society B: Biological Sciences,* vol. 305, pp. 79-113, 1984.

[41] J. Rayner, “A vortex theory of animal flight. Part 1. The vortex wake of a hovering animal,” *Journal of Fluid Mechanics,* vol. 91, pp. 697-730, 1979.

[42] C. P. Ellington, The aerodynamics of hovering insect flight. I. The quasi-steady analysis, London: Royal Society, 1984.

[43] C. P. Ellington, “The Aerodynamics of Hovering Insect Flight. II. Morphological Parameters,” *Royal Society of London Philosophical Transactions Series B,* vol. 305, 1984.

[44] C. Ellington, “The Aerodynamics of Hovering Insect Flight. III. Kinematics,” *Royal Society of London Philosophical Transactions Series B,* vol. 305, 1984.

[45] M. H. Dickinson, F.-O. Lehmann and S. P. Sane, “Wing Rotation and the Aerodynamic Basis of Insect Flight,” *Science,* vol. 284, no. 5422, pp. 1954-1960, 1999.

[46] Z. J. Wang, “Vortex shedding and frequency selection in flapping flight,” *Journal of Fluid Mechanics,* vol. 410, pp. 323-341, 2000.

[47] S. Sane and M. Dickinson, “The aerodynamic effects of wing rotation and a revised quasi-steady model of flapping flight,” *The Journal of experimental biology,* vol. 205, pp. 1087-1096, 2002.

[48] M. Dickinson and K. GÖTZ, “Unsteady Aerodynamic Performance of Model Wings at Low Reynolds Numbers,” *J. Exp. Biol,* vol. 174, 1993.

[49] S. P. Sane, “The aerodynamics of insect flight,” *The Journal of experimental biology,* vol. 206, pp. 4191-4208, 2004.

[50] M. Kramer, “Die Zunahme des Maximalauftriebes von Tragflugeln bei plotzlicher Anstellwinkelvergrosserung,” *Zeitschrift fur Flugtechnik and Motorluftschiffahrt,* vol. 23, pp. 185-189, 1932.

[51] M. Sun and J. Tang, “Unsteady aerodynamics force generation by a model fruit fly in flapping motion,” *The Journal of experimental biology,* vol. 205, pp. 55-70, 2002.

[52] M. Sun and J. Tang, “Lift and Power Requirements of Hovering Flight in Drosophila virilis,” *The Journal of experimental biology,* vol. 205, pp. 2413-2427, 2002.

[53] K. G. Götz, “Course-control, metabolism and wing interference during ultralong tethered flight in Drosophila melanogaster,” *J. Exp. Biol,* vol. 128, pp. 35-46, 1987.

[54] A. K. Brodsky, “Vortex Formation in the Tethered Flight of the Peacock Butterfly Inachis io L. (Lepidoptera, Nymphalidae) and some Aspects of Insect Flight Evolution,” *Journal of Experimental Biology,* vol. 161, 1991.

[55] Y. Moryossef and Y. Levy, “Effect of Oscillations on Airfoils in Close Proximity to the Ground,” *AIAA J,* vol. 42, pp. 1755-1764, 2004.

[56] T. Gao and X. Y. Lu, “Insect normal hovering flight in ground effect,” *PHYS FLUIDS,* vol. 20, 2008.

[57] J. Molina and X. Zhang, “Aerodynamics of a Heaving Airfoil in Ground Effect,” *AIAA J,* vol. 49, pp. 1168-1179, 2011.

[58] J. Y. Su, J. H. Tang and C. Wang, “A numerical investigation on the ground effect of a flapping-flying bird,” *Physics of Fluids,* vol. 25, p. 3101, 2013.

[59] J. Wu, C. Liu, S. C. Yang and N. Zhao, “Influence of a flexible tail on the performance of a foil hovering near the ground: Numerical investigation,” *B/Fluids,* vol. 52, pp. 85-96, 2015.

[60] H. Lu, K. B. Lua, Y. Lee, T. Lim and K. Yeo, “Ground effect on the aerodynamics of three-dimensional hovering wings,” *Bioinspiration & Biomimetics,* vol. 11, p. 066003, 2016.

[61] Z. J. Wang, “The role of drag in insect hovering,” *The Journal of experimental biology,* vol. 207, pp. 4147-4155, 2004.

[62] S. Vogel, “Flight in Drosophila I. Flight Performance of Tethered Flies,” *Journal of Experimental Biology,* vol. 44, pp. 567-578, 1966.

[63] D. E. ALEXANDER, “Unusual Phase Relationships Between The Forewings And Hindwings In Flying Dragonflies,” *Journal of Experimental Biology,* vol. 109, no. 1, pp. 379-383, 1984.

[64] L. Shilong and S. Mao, “Aerodynamic force and flow structures of two airfoils in flapping motions,” *Acta Mechanica Sinica,* vol. 17, pp. 310-331, 2001.

[65] H. Huang and M. Sun, “Dragonfly Forewing Hindwing Interaction at Various Flight Speeds and Wing Phasing,” *AIAA Journal,* vol. 45, pp. 508-511, 2007.

[66] T. Broering and Y.-S. Lian, “The effect of phase angle and wing spacing on tandem flapping wings,” *Acta Mechanica Sinica,* vol. 28, 2012.

[67] T. Broering and Y. Lian, “Numerical study of tandem flapping wing aerodynamics in both two and three dimensions,” *Computers & Fluids,* vol. 115, pp. 124-139, 2015.

[68] w. b. Tay, “Effect of Different Types of Wing-Wing Interactions in Flapping MAVs,” *Journal of Bionic Engineering,* vol. 14, pp. 60-74, 2017.

[69] A. R. Shanmugam and C. H. Sohn, “Numerical investigation of the aerodynamic benefits of wing-wing interactions in a dragonfly-like flapping wing,” *Journal of Mechanical Science and Technology,* vol. 33, no. 6, pp. 2725-2735, 2019.

[70] Y. Zheng, Y. Wu and H. Tang, “Force measurements of flexible tandem wings in hovering and forward flights,” *Bioinspiration & biomimetics,* vol. 10, p. 016021, 2015.

[71] K. B. Lua, H. Lu, X. Zhang, T. Lim and K. Yeo, “Aerodynamics of two-dimensional flapping wings in tandem configuration,” *Physics of Fluids,* vol. 28, 2016.

[72] Q. Li, M. Zheng, T. Pan and G. Su, “Experimental and Numerical Investigation on Dragonfly Wing and Body Motion during Voluntary Take-off,” *Scientific Reports,* vol. 8, 2018.

[73] C. Li and H. Dong, “Wing kinematics measurement and aerodynamics of a dragonfly in turning flight,” *Bioinspiration & biomimetics,* vol. 12, 2017.

[74] R. Dudley and C. Ellington, “Mechanics of forward flight in bumblebees: I. Kinematics and morphology,” *J. Exp. Biol,* vol. 148, p. 19–52, 1990.

[75] J. Zhu and C. Y. Zhou, “Aerodynamic performance of a two-dimensional flapping wing in asymmetric stroke,” *Proceedings of the Institution of Mechanical Engineers, Part G: Journal of Aerospace Engineering,* vol. 228, pp. 641-651, 2014.

[76] C. Wang, C. Zhou and P. Xie, “Numerical investigation on aerodynamic performance of a 2-D inclined hovering wing in asymmetric strokes,” *Journal of Mechanical Science and Technology,* vol. 30, pp. 199-210, 2016.

[77] S. D. R, B. S and K. R, “PHYSICS-BASED DESIGN OF MICRO AIR VEHICLES,” AIR FORCE RESEARCH LABORATORY , UNITED STATES, 2012.

[78] J. D. Anderson, Fundamentals of Aerodynamics, 4th Edition ed., New York: McGraw-HIll, 2007.

[79] K. Jones, C. Dohring and M. Platzer, “Wake structures behind plunging airfoils - A comparison of numerical and experimental results,” *34th Annual Aerospace Sciences Meeting and Exhibit. Reno, NV: AIAA,* vol. 78, 1996.

[80] M. Ol and M. Gharib, “The passage toward stall of nonslender delta wings at low Reynolds number,” in *31st AIAA Fluid Dynamics Conference and Exhibit*, 2001.

[81] F. Moukalled, L. Mangani and M. Darwish, The Finite Volume Method in Computational Fluid Dynamics: An Advanced Introduction with OpenFOAM® and Matlab®, vol. 113, Stuttgart: Springer, 2015.

[82] Š. Borna, “NUMERICAL CHARACTERISATION OF A SHIP,” UNIVERSITY OF ZAGREB Faculty of Mechanical Engineering and Naval Architecture, 2017.

[83] ANSYS Fluent Theory Guide, Canonsburg: ANSYS, Inc, 2013.

[84] T. Barth and D. Jespersen, “The Design and Application of Upwind Schemes on Unstructured Meshes,” *AIAA Paper 89-0366,* vol. 0366, 1989.

[85] B. Leonard and S. Mokhtari, “ULTRA-SHARP Nonoscillatory Convection Schemes for High-Speed Steady Multidimensional Flow,” 1990.

[86] S. Patankar, Numerical heat transfer and fluid flow, Washington DC: Hemisphere Publishing Corporation, 1980.

[87] W. Ranz and W. Marshall, “Evaporation from drops, part I,” *Chem. Eng. Prog,* vol. 48, pp. 141-146, 1952.

[88] G. Taylor, R. Nudds and Thomas, “A. Flying and swimming animals cruise at a Strouhal number tuned for high power efficiency,” *Nature,* vol. 425, p. 707–711 , 2003.

[89] P. Freymuth, “Thrust generation by an airfoil in hover modes,” *Experiments in Fluids,* vol. 9, pp. 17-24, 1990.

[90] J. Castillo, Mathematical Aspects of Numerical Grid Generation, Philadelphia: Society for Industrial and applied Mathematic, 1991.

[91] J. H. Park and K. J. Yoon, “Designing a Biomimetic Ornithopter Capable of Sustained and Controlled Flight,” vol. 5, pp. 39-47, 2008.

[92] S. Xu and Z. J. Wang, “An immersed interface method for simulating the interaction of a fluid with moving boundaries,” *Journal of Computational Physics,* vol. 216, pp. 454-493, 2006.

[93] Z. J. Wang, “Two Dimensional Mechanism for Insect Hovering,” *Physical review letters,* vol. 85, pp. 2216-2219, 2000.

[94] J. Wakeling and C. Ellington, “Dragonfly flight. I. Gliding flight and steady-state aerodynamic forces,” *The Journal of experimental biology,* vol. 200, pp. 543-556, 1997.

[95] J. Wang and M. Sun, “ A computational study of the aerodynamics and forewing-hindwing interaction of a model dragonfly in forward flight,” *The Journal of experimental biology,* vol. 208, pp. 3785-3804, 2005.

[96] H. Dong and Z. Liang, “Effects of Ipsilateral Wing-Wing Interactions on Aerodynamic Performance of Flapping Wings,” *48th AIAA Aerospace Sciences Meeting Including the New Horizons Forum and Aerospace Exposition,* 2010.

[97] T. Broering and Y. Lian, “The Effect of Wing Spacing on Tandem Wing Aerodynamics,” *28th AIAA Applied Aerodynamics Conference,* 2010.

[98] K. Lim and w. b. Tay, “Numerical analysis of the s1020 airfoils in tandem under different flapping configurations,” *Acta Mechanica Sinica,* vol. 26, 2010.

[99] C. Somps and L. MW, “Dragonfly Flight: Novel Uses of Unsteady Separated Flows,” *Science,* vol. 228, pp. 1326-1329, 1985.